Silicon photomultiplier based continuous-wave functional near-infrared spectroscopy module with multi-distance measurements

Mahlet Alemayehu Zewde

School of Science

Thesis submitted for examination for the degree of Master of Science in Technology.

Espoo 08.04.2019

Supervisor

Prof. Risto Ilmoniemi

Advisor

D.Sc. Ilkka Nissilä

Aalto University
School of Science

Aalto University, P.O. BOX 11000, 00076 AALTO
www.aalto.fi
Abstract of the master's thesis

Author Mahlet Alemayehu Zewde

Title Silicon photomultiplier based continuous-wave functional near-infrared spectroscopy module with multi-distance measurements

Degree programme Master's Programme in Life Science Technologies

Major Biomedical Engineering **Code of major** SCI3059

Supervisor Prof. Risto Ilmoniemi

Advisor D.Sc. Ilkka Nissilä

Date 08.04.2019 **Number of pages** 58+21 **Language** English

Abstract

In recent years, there has been growing interest in developing fiberless and wireless functional near-infrared spectroscopy (fNIRS) and diffuse optical tomography (DOT) instruments. However, developing such instruments poses multiple challenges, in terms of cost, safety, system complexity and achievable signal quality. One crucial factor in developing wireless and fiberless instruments is the appropriate choice of detectors.

Currently, the majority of existing wireless and/or fiberless systems use photodiodes due to their low cost and low power requirements. However, under low-light conditions, the SNR of photodiodes diminishes significantly, making them less effective for measurements with long source–detector separations. The silicon photomultiplier (SiPM) is a relatively new type of detector that contains high internal amplification; this makes SiPMs suitable for low-light applications. Although SiPMs can increase signal quality at long source–detector distances, they cost more and have higher power requirements than photodiodes.

This thesis presents the design of a multi-distance, multichannel DOT prototype that uses a hybrid detector arrangement. This arrangement uses photodiodes for short-distance measurements (i.e., 1 cm) and silicon photomultipliers for long-distance measurements (i.e., 3 cm and 4.5 cm). The developed system consists of two printed circuit boards (PCBs): a DOT sensor PCB, a data acquisition and control PCB as well as a graphical user interface. The performance of the developed DOT system prototype was validated using a dynamic optical phantom. The results show that the prototype works as intended.

Keywords Optical imaging, near-infrared spectroscopy, neuroimaging, continuous-wave instrumentation

Preface

At first, I would like to thank my advisor Dr. Ilkka Nissilä for giving me the opportunity to work on this project and introducing me to the exciting world of near-infrared spectroscopy. Your support and feedback has helped me to improve, Thank You! I would also like to thank my supervisor Prof. Risto Ilmoniemi for making the time in his busy schedule to read my work, listen to my presentation and giving me valuable feedback.

The members of the fNIRS group Pauliina Hirvi and Salla Autti, Thank you for being such a good workmates, and for all the shared lunches and memories. I would like to thank Mr. Helge Kainulainen for letting me use his laboratory space and for giving me a much needed technical support. I would also like to thank the NBE department for providing good working conditions.

Finally, I would love to thank my loved ones, without you non of this would be possible *Ewedachehualehu*. My dear mother Almaz Demeke and my beloved sister Mihret Alemayehu, for believing in me and for your kind encouraging words whenever I doubted myself. My dear brother Yoni for the listening ears and giving me your wise advice. Robiye, Thank You! for all the care and showing interest in my work.

Otaniemi, April 8, 2019

Mahlet Alemayehu Zewde

Contents

Abbreviations

ADC	Analog-to-digital converter
APD	Avalanche photodiode
ASL	Arterial spin labeling
BCI	Brain–computer interface
BLL	Beer–Lambert law
CCO	Cytochrome c oxidase
CNR	Contrast-to-noise ratio
CPU	Central processing unit
CSF	Cerebrospinal fluid
CT	Computed tomography
CW	Continuous-wave
DAQ	Data acquisition
DAQ-C	Data acquisition and control
DOT	Diffuse optical tomography
EEG	Electroencephalography
EMI	Electromagnetic interference
ENOB	Effective number of bits
FD	Frequency-domain
fMRI	Functional magnetic resonance imaging
fNIRS	Functional near-infrared spectroscopy
FOV	Field of view
GUI	Graphical user interface
IPC	Inter-processor communication
ISR	Interrupt-service routine
LED	Light-emitting diode
LD	Laser diode
MBLL	Modified Beer-Lambert law
MEG	Magnetoencephalography
MPPC	Multi-pixel photon counter
NIR	Near-infrared
Op-amp	Operational amplifier
PCB	Printed circuit board
PD	Photodiode
PDE	Photon detection efficiency
PGA	Programmable-gain amplifier
PET	Positron emission tomography
PMT	Photomultiplier tube
RAM	Random-access memory
SDS	Source–detector separation
SiPM	Silicon photomultiplier
SNR	Signal-to-noise ratio

SPAD	Single-photon avalanche diode
SPI	Serial peripheral interface
TD	Time-domain
THI	Traumatic head injury
TIA	Transimpedance amplifier
TMS	Transcranial magnetic stimulation
UART	Universal asynchronous receiver-transmitter

1 Introduction

Imaging of the structure and function of the brain using various modalities is known as neuroimaging. Currently, numerous neuroimaging modalities are available. These modalities can be classified into two types: functional and structural neuroimaging. As the names suggest, structural modalities image the anatomical structure of the brain, while functional modalities measure an aspect of brain function. Functional neuroimaging modalities can be further classified into two types: direct and indirect. Direct functional neuroimaging modalities, such as electroencephalography (EEG) and magnetoencephalography (MEG), collect functional information by measuring directly the electromagnetic activity generated as a result of neuronal activity in the brain. On the other hand, indirect neuroimaging modalities measure haemodynamic and metabolic activity coupled with neuronal activity and make inferences about the function of the brain. Haemodynamic and metabolic activity is commonly measured using three modalities: functional magnetic resonance imaging (fMRI), positron emission tomography (PET), and functional near infrared spectroscopy (fNIRS). fNIRS is an optical neuroimaging modality that literally shines near infrared (NIR) light into the brain to measure changes in blood volume and cerebral oxygenation.

Various factors affect the adoption of neuroimaging modalities in the clinical world and in research. These factors include instrument size, portability, cost, reliability, non-invasiveness, ease of use as well as spatial and temporal resolution. Compared to the other modalities, fNIRS has multiple advantages, including non-invasiveness, portability and cost efficiency. In addition, fNIRS is silent, safe and does not require a specially shielded room. These advantages make fNIRS potentially suitable for applications that require long-term, repeated imaging, such as brain computer interface systems (BCI) and bedside monitoring devices. Additionally, fNIRS is suitable for imaging preterm and newborn babies as well as for conducting studies outside the limitations of the laboratory environment [85, 66, 23].

To fully realize the potential advantages of fNIRS, it would be necessary to make considerable advances in technology in terms of both software and hardware. Recent years have witnessed increased interest in developing wireless and fiberless fNIRS systems [54, 96], since building such a system could make the technology widely available for out-of-the-lab uses. Conducting neuroimaging studies without the limitations of the laboratory environment would be an invaluable asset and would enable researchers to study the human brain in more naturalistic environments.

However, building a wireless and fiberless fNIRS instrument poses multiple challenges. One of these challenges is using sufficiently powerful optical sources and detectors without compromising the portability of the system. Currently, a majority of fNIRS systems use photomultiplier tubes (PMTs), avalanche photodiodes (APDs) or photodiodes (PDs) as detectors. Each of these detectors have their own limitations. For instance, PMTs are in general large in size and require very high bias voltage (several kilovolts). Thus, most PMT-based systems use optical fibers to transmit light from light sources to the detectors. Although PMTs possess good sensitivity and signal-to-noise ratio (SNR), the use of optical fibers along with PMTs increases instrument size, thus limiting their implementation as a wireless technology. On

the other hand, APDs have lower bias voltage needs (a few hundred volts) than PMTs; however, this is still too high and raises safety concerns for fiberless on-scalp implementation. On the contrary, PDs have lower bias voltage, thus can be used in fiberless systems. However, PDs have limited sensitivity compared to the other detectors. In recent years, some research groups have sugested that the use of silicon photo-multipliers (SIPMs) for fNIRS systems [82, 130] can improve sensitivity. SIPMs are a relatively new type of detectors that have a sensitivity comparable to that of PMTs, lower voltage requirements (less than hundred volts) and relatively easy integration into on-scalp fNIRS systems. This makes SiPMs a potentially suitable detector choice for fiberless fNIRS systems.

In fNIRS systems, the signal from the light detectors is influenced by multiple factors, one of which is the distance between the light sources and detectors. The general rule of thumb is that the signal contribution from the brain increases with increasing the source–detector separation (SDS). Thus, measuring at multiple SDS distances allows information to be collected from multiple depths for use in three-dimensional maps of cerebral haemodynamic and metabolic activity. For example, measuring at short SDS would make it possible to obtain information mainly from the superficial tissue, which can be regressed from long distance measurements that have an increased contribution of information collected from the brain. An extension of fNIRS that reconstructs three-dimensional maps of cerebral haemodynamic and metabolic activity is called diffuse optical tomography (DOT).

Although the contribution of the signal from the brain increases with increasing SDS, the measured light intensity decreases by approximately 10 dB/cm. Consequently, highly sensitive detectors are needed for longer SDS measurements. However, these detectors, i.e., SiPMs and PMTs are expensive and require complex instrumentation. Therefore, using low-sensitivity detectors (e.g., PDs) for shorter SDS ($\leq$ 1 cm) where the light intensity is sufficient, and highly sensitive detectors for intermediate and large SDS (eg., 3–4.5 cm) where the light intensity is significantly lower can be a good strategy for developing cost-efficient fiberless continuous-wave DOT instruments.

The goal of this thesis is to design and implement a fiberless DOT sensor unit as well as data acquisition and control (DAQ-C) unit prototypes. The DOT sensor unit consists of (1) three SIPMs for long and intermediate SDS (3–4.5 cm) measurements, (2) three PDs for short SDS (1 cm) measurements, (3) a preamplifier circuit to amplify the signal from the SIPMs and PDs, as well as (4) three dual-wavelength LEDs. The DAQC module prototype consists of (1) an 8-channel simultaneously sampling ADC for converting the signal from the detectors into a digital form, (2) a LED current modulator for modulating the LED currents, and (3) a microcontroller for controlling the ADC and LED current driver as well as for transmitting the received data to a computer.

The rest of this thesis is organized into four chapters. Chapter 2 reviews the current state of the technology and the working principles of fNIRS and DOT. Chapter 3 discusses the detailed design process of the prototype. Chapter 4 presents tests and phantom experiments conducted to validate the developed system. Finally, Chapter 5 summarizes the achievements and limitations of the developed system.

2 fNIRS and DOT

DOT is an extension of fNIRS that reconstructs three-dimensional maps of brain function. fNIRS is a neuroimaging modality which uses near-infrared light for imaging cerebral haemodynamic and metabolic changes. In order to design and implement a new DOT prototype, it is therefore crucial to understand the working principles, instrumentation techniques and state of the art of the fNIRS technology. Section 2.1 describes the working principles of fNIRS. Section 2.2 provides a general overview of fNIRS instruments and instrumentation techniques. Section 2.3 discusses DOT systems. Section 2.4 discusses the key application areas of fNIRS in clinical settings and in neuroimaging research. Finally, section 2.5 reviews the state of the art of current fiberless and wireless fNIRS and DOT systems.

2.1 Working Principles

This section discusses core principles that have been crucial for the realization of fNIRS as a neuroimaging modality. These principles include the nature of tissue–light interaction, the physiology of the brain as well as the relationship between light and tissue optical properties. Each of these will be discussed in detail in the coming subsections.

2.1.1 Tissue–Light Interaction

The interaction of light with tissue takes two forms: absorption and scattering. Absorption is a process in which light passing through a medium becomes attenuated by molecules in the medium. Light passing through the human head gets attenuated by various types of absorbers, including water, hemoglobin, enzymes, skull, scalp, lipid and cerebrospinal fluid (CSF). In addition to absorption, light passing through multiple layers of tissue encounters multiple scattering events. Both the scattering and absorption of light are dependent on the path that light takes through tissue. Fig. 1.A shows the propagation of light inside absorbing and scattering media as it travels from light source to detector.

Light in the NIR region has the ability to penetrate through intact human skull. This behaviour was first demonstrated experimentally by Jöbsis [49]. NIR light at wavelengths in the range of 690 to 900 nm is known as the optical window of tissue. Within the optical window, the skull, scalp and hemoglobin have relatively low absorption coefficients, enabling the monitoring of cerebral oxygenation and blood volume changes in a non-invasive manner. In addition, within this wavelength range, hemoglobin and the enzyme cytochrome-c-oxidase (CCO) have distinct absorption spectra in their oxygenated and de-oxygenated forms. Fig. 1.B shows the absorption of oxygenated hemoglobin (HHb), deoxygenated hemoglobin (HbO_2) and water with respect to the wavelength of light.

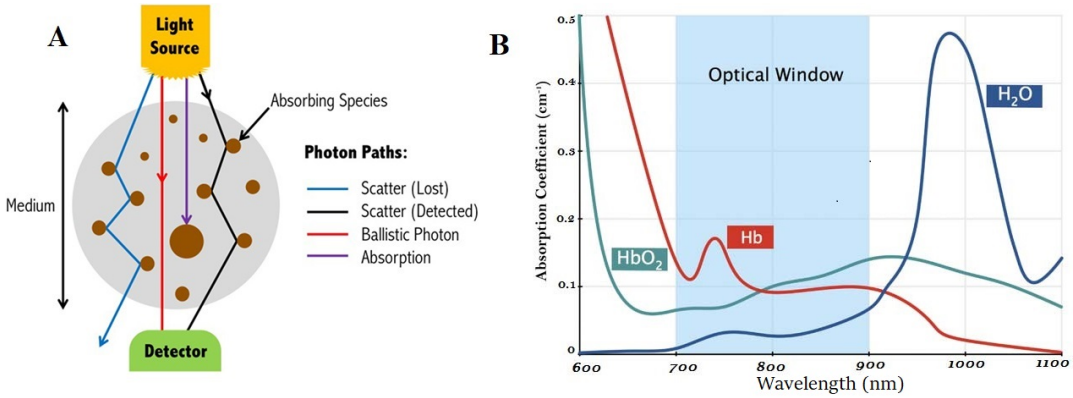

Figure 1: A. As photons propagate through an absorbing and scattering medium, they can be absorbed or scattered by the medium. Rarely, the photon passes directly to the detector without any absorption or scattering (ballistic photons). Only a portion of the photons are detected; while a majority photons are either absorbed by the tissue or exit the tissue without being detected. Adapted from [90]. B. Absorption coefficient of HbO_2, HHb and water in the NIR spectrum. The optical window shows the range of wavelengths where tissue has the lowest absorption factor. Adapted from [88]

2.1.2 Mathematical Formulas and Technical Advancements

As discussed in the previous section, the interaction between light and tissue is of two types: absorption and scattering. In order to form an image it is crucial to formulate a clear relationship between the changes in the intensity of input light and the concentration of absorbing chromophores (HbO_2 and HHb). The Beer–Lambert law (BLL) is a mathematical equation that formulates a linear relationship between the concentration of a light-absorbing molecule and the attenuation of light passing through it. This reationship is expressed in Equation 1.

$$A = \log(\frac{I_o}{I}) = \epsilon * C * d \tag{1}$$

Where A represents the attenuation, I is the detected light intensity, I_o is the input light intensity, ϵ is the wavelength-dependent extinction coefficient, C is the concentration of the attenuating molecule and d denotes the distance between the light source and detector.

The original BLL takes into consideration the attenuation of light as a result of absorption only. However, as mentioned earlier, the transport of photons in tissue encounters multiple scattering events in addition to absorption. These scattering events lead to rapid diffusion of the propagating photons. Scattering also increases the distance travelled by photons within tissue, thereby leading to an increase in the probability of photon absorption. This limits our ability to know the exact length of the optical path taken by light. Thus, the original form of BLL is insufficient for estimating the concentration of chromomophores in scattering media. As a result, a modified form of the Beer–Lambert law (MBLL) has been developed account for the

effects of scattering [26]. A simplified version of the MBLL is given in Equation 2.

$$A = \log(\frac{I_o}{I}) = \epsilon * C * L + G \tag{2}$$

Where L is the total mean path length of detected photons events which, takes to account the scattering dependent optical path length increase. The term G here represents the measurement geometry dependent factor which accounts for the intensity loss caused by scattering.

The human head contains multiple light-absorbing chromophores. Measuring the concentration of multiple chromophores in a mixture, such as the human head, requires a multi-wavelength spectrometer. Multi-wavelength spectrometers should use at least the same number of distinct wavelengths as the number of chromophores under investigation. For instance, fNIRS instruments generally measure the chromophores HbO_2 and HHb. Thus, it is necessary to use at least two distinct wavelengths of light [23, 59]. In addition to monitoring HbO_2 and HHb, a minority of instruments [121, 21] additionally measure the enzyme CCO using four or more wavelengths of NIR light.

The first multiple-wavelength tissue spectrometer was invented in the 1936 by the physicist Glen Millikan. This spectrometer had two wavelengths and was used as an hemoglobinometer. This and similar developments in spectrometric techniques have laid the technical foundations for the development of modern day fNIRS instruments. [19, 73, 72]

Because the human head consists of multiple chromophores, it is impossible to determine the absolute concentration of any of the chromophores using the MBLL equation. For this reason, the differential form of the MBLL (i.e., dMBLL) is used to determine the relative change in the concentration of the chromophores under investigation at distinct wavelengths. Equation 3 shows the generalized form of the dMBLL given for n chromophores and n number of wavelength combinations.

$$\begin{bmatrix} \Delta[HbO_2] \\ \Delta[HHb] \\ \vdots \\ \Delta[oxCCO] \end{bmatrix} = \mathbf{L^{-1}} \begin{bmatrix} \epsilon_{HbO_2}(\lambda_1) & \epsilon_{HHb}(\lambda_1) & \epsilon_{oxCCO}(\lambda_1) \\ \epsilon_{HbO_2}(\lambda_2) & \epsilon_{HHb}(\lambda_2) & \epsilon_{oxCCO}(\lambda_2) \\ \vdots & \vdots & \vdots \\ \epsilon_{HbO_2}(\lambda_n) & \epsilon_{HHb}(\lambda_n) & \epsilon_{oxCCO}(\lambda_n) \end{bmatrix}^{-1} \begin{bmatrix} \Delta A(\lambda_1) \\ \Delta A(\lambda_2) \\ \vdots \\ \Delta A(\lambda_n) \end{bmatrix} \tag{3}$$

The dMBLL equation is based on two assumptions: the absorption of tissue changes homogeneously, and the photon loss caused as a result of scattering is constant. These assumptions result in some inaccuracies in estimating concentration changes. Consequently, changes in concentration calculated using the dMBLL are influenced by cross talk resulting from concentration changes of other, unmonitored chromomophores. Moreover, the dMBLL underestimates the concentration changes as a result of the partial volume effect. Therefor, the dMBLL yields only qualitative results. Various researchers have proposed ways to improve these limitations in the accuracy of the dMBLL equation. [58, 110, 103]

Some groups have also proposed new approaches that are based on modelling photon propagation inside tissue, known as the forward problem. The forward

model is then used to reconstruct an image of the underlying tissue (i.e., the inverse solution). The diffusion equation and radiative transfer equation are the most common analytical expressions of forward models that can be solved by numerical methods. On the other hand, the Monte Carlo method is a stochastic method widely used to simulate photon trajectories through tissue as well as measurement sensitivity. The forward model obtained from formulas or numerical methods is then used for image reconstruction. This requires an inverse solver that uses either linear or nonlinear methods. [9, 47]

2.1.3 Physiological and Biochemical Processes of the Brain

Furthermore, the nature of physiological and biochemical processes in the brain has allowed for the realization of fNIRS as a neuroimaging modality. Both fNIRS and DOT indirectly measure the neuronal activity by measuring metabolic and haemodynamic processes. These processes strongly correlate with the neuronal activity in the brain; this correlation is called the neurovascular coupling. This behaviour has been investigated by various groups.[114, 46, 32]

Typically, upon stimulus onset the metabolic demand in the brain increases, leading to an initial brief dip in HbO_2 and an increase in HHb. This is followed by an overflow of oxygenated blood, which results in an increase in HbO_2 and a decrease in HHb. Finally, a steady increase in HBO_2 and a decrease in HHb occurs, followed by a slow, steady decrease in the HbO_2 and increase in the HHb. fNIRS can measure these oscillations in HBO_2 and HHb. In contrast, fMRI measures the blood oxygen level-dependent (BOLD) signal resulting from only oscillations in HHb. A special kind of fMRI, known as arterial spin labeling (ASL) fMRI can measure cerebral blood flow in addition to the BOLD signal. Fig. 2.B shows a typical haemodynamic process coupled with stimuli.

Many biochemical processes in the brain rely on the enzyme CCO for oxygen metabolism. CCO has been shown to have more brain specificity than hemoglobin due to its involvement in as much as 95% of oxygen metabolism in neurons [113, 50, 60, 13]. Additionally, unlike hemoglobin, CCO is mainly found in the brain, with its concentration being low in the skull and scalp. Despite the higher brain specifity of CCO, HbO_2 and HHb still remain to be the most common chromophores investigated using fNIRS instruments due to their higher abundance compared to CCO. Fig. 2.A illustrates the physiological sources of the haemodynamic and metabolic signals measured by fNIRS.

2.2 fNIRS Instrumentation

A typical fNIRS instrument consists of light sources at two or more wavelengths and light detectors located several centimetres apart from each other. The light from the sources travels through the scalp, skull and some brain tissue and back. The detectors measure this back-scattered light. The detected signal is then further amplified and converted into a digital format using an analog-to-digital-converter (ADC). The choice of light sources, detectors and control circuit are crucial in determining the

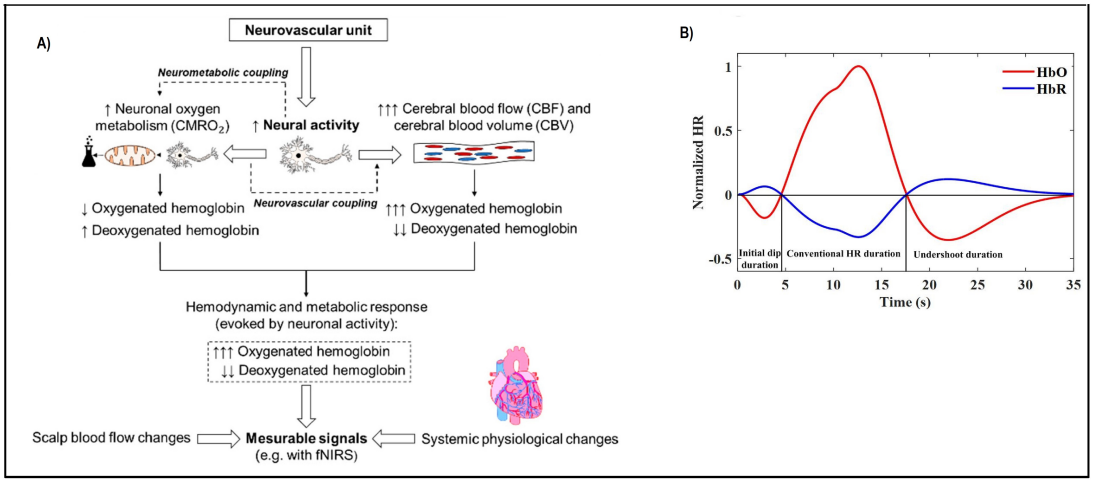

Figure 2: A. Physiological model of the fNIRS signals. Adapted from [44] B. A model of a typical haemodynamic response including the initial dip. Adapted from [45]

capability of an fNIRS system. Hence, it is important to understand each constituent when designing an fNIRS system. Fig. 3 shows a block diagram of a typical fNIRS system and its constituents.

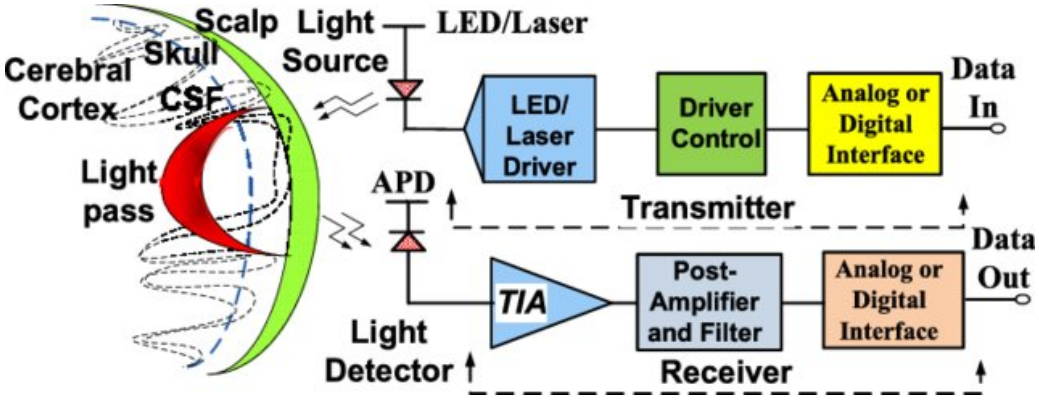

Figure 3: A block diagram of a typical fNIRS instrument. Copied from [53]

The following sections present the constituents of an fNIRS instrument, sources of noise and techniques used to reduce noise, as well as instrumentation techniques.

2.2.1 Probe Geometry

fNIRS systems can be classified into reflectance and transmittance mode systems based on the relative position of light sources and detectors to each other. Reflectance mode systems consist of detector optodes placed contralateral to source optodes, as shown in Fig. 4.A. Such an optode arrangement used mainly for investigating newborn and preterm babies; since their thin skull allows for enough photons to be collected by the detector in the opposite side [23]. However, this arrangement is not

applicable for adults, where the skull is significantly thicker; thus, reflective mode systems are used instead. In reflectance mode fNIRS systems, detectors are placed ipsilateral to sources. In this arrangement, the detectors detect the back-scattered light as a result of multiple scattering events that occur in various cell membranes. The transport of light from the source optodes to the detectors in a reflective mode arrangement somewhat resembles a random walk leading to the famous banana shape, shown in Fig. 4.B. The general rule of thumb in reflectance mode systems is that increased source–detector separation (SDS) leads to a decrease in the amount of detected signal and an increase in sensitivity to depth. Therefore, the optimal SDS should have adequate sensitivity to brain tissue, and sufficient light should reach the surface of the detectors [105, 95]. Most fNIRS systems use an SDS of 2–4 cm.

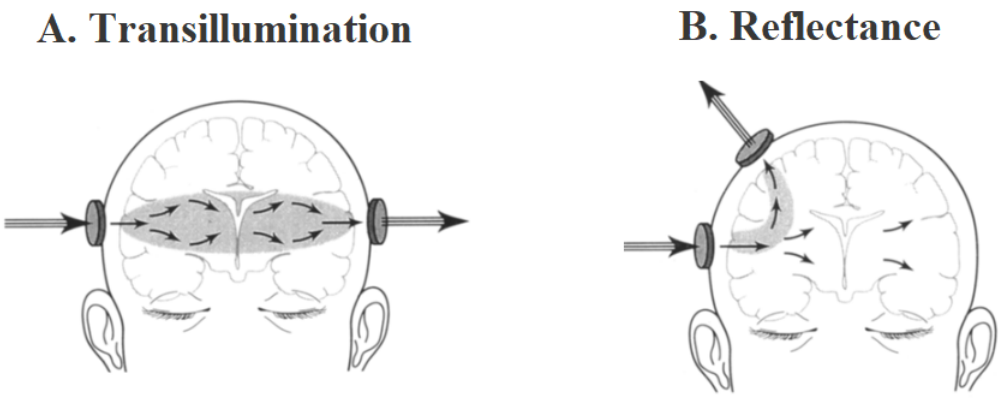

Figure 4: Arrangement of optodes in ransmittive mode (A) and reflectance mode (B). Adapted from [118]

In addition to SDS, the optode arrangement has a significant effect on the field of view (FOV) of multichannel fNIRS instruments. Thus, fNIRS optode grids should be designed taking into consideration the region of interest to be investigated and the attempted FOV. In general, high-density optode arrangements, with multiple partially overlapping source–detector pairs, provide a better contrast-to-noise ratio. Additionally, multi-distance measurements improve depth resolution in reconstructed images. [43, 120, 38]

2.2.2 fNIRS Instrumentation Techniques

Depending on the instrumentation technique used, fNIRS systems can be classified into three categories: time-domain (TD), frequency-domain (FD) and continuous-wave (CW) systems. TD systems use pico-second-long light pulses in order to measure the amplitude and arrival time of detected photons. These photon arrival times are used to form temporal time spread function. Using this information, TD systems can provide quantitative information regarding the concentration of the chromophores under study. However, TD systems require a complex and expensive design relying

on light sources, detectors and detection electronics with extremely fast rise times.

On the other hand, FD systems use radio frequency intensity modulated light sources. FD systems measure the amplitude and phase shift of the photon density wave at the detector. The phase shift information can be used to estimate the time of flight of the light in tissue, which is then used to calculate the path length that the light has travelled before it reaches the detectors. FD systems also provide quantitative information regarding the concentration of chromophores.

Unlike FD and TD systems, CW systems measure only the intensity of light. Thus, this intensity is used to to measure only semiquantitative changes in concentrations. The CW technique is less complex to implement and has the advantage of a straightforward design. A major drawback in CW systems is the lack of information regarding the background optical properties. Even with this drawback, CW systems are the most widely used of the three because they are relatively cheap and easy to implement.

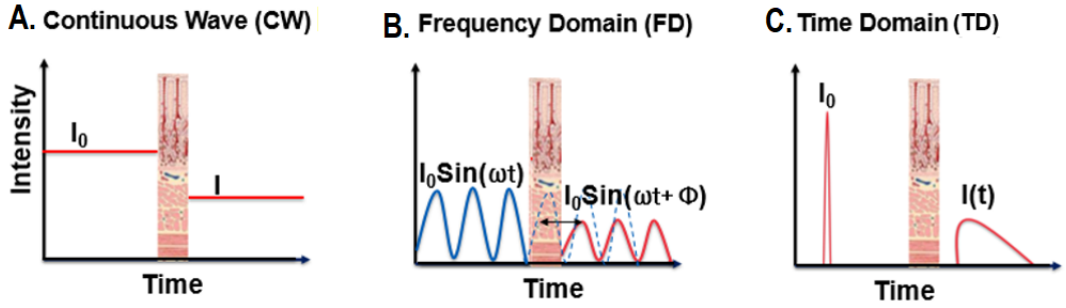

Figure 5: Illustration of the three different functional near-infrared spectroscopy techniques. The CW technique (A) measures only the intensity of light, the FD technique (B) measures the phase shift between the input and detected signal in addition to intensity. The TD technique (C) measures the distribution of time of flight of photons inside the tissue as well as the change in intensity. [99]

2.2.3 Light Emitters and Associated Circuitry

For fNIRS instrumentation, choosing the suitable type of light emitter is dependent on various factors, including the instrumentation type, required response speed, size and cost. The majority of fNIRS instruments available today make use of light-emitting diodes (LEDs) and Laser Diodes (LDs) [102, 78, 29, 92, 1, 117]. However, TD systems require special types of lasers (i.e., titanium-sapphire lasers, pulsed semiconductor lasers and supercontinuum lasers) which can generate ultra-short pulses of light [97, 79, 71, 42]. LDs have a faster response time than LEDs, thus making them suitable for FD systems in which the NIR light is modulated by a radio frequency reference signal. In addition, LDs generate narrow bandwidth light (<1 nm), which is beneficial to accurately calculate concentration changes using the dMBLL equation. However, LDs tend to be more expensive and have tighter safety regulations than LEDs. Thus, LEDs are a cost efficient option for CW instruments measuring only

qualitative concentration changes and where a broad spectral bandwidth (∼30 nm) is not a an issue.

As mentioned in 2.1.2, the wavelength selected for light sources depends on the type and number of chromophores measured by the fNIRS instrument. Most fNIRS systems employ only two wavelengths to detect concentration changes in HbO_2 and HHb [102, 78, 29, 92, 1, 117]. If absolute measurements are desired in CW systems, it is necessary to use multiple wavelengths (>4). Additionally, studies suggest, optimizing wavelength combinations can improve measurement reliability by increasing separability between chromophores and decreasing cross talk. [110, 8]

In fNIRS systems, it is common practice to implement either time division multiplexing or frequency division multiplexing to deliver the light emitted from the different sources in a system. Time division multiplexing is a method for switching on each light source one at a time. On the other hand, in frequency division multiplexing all light sources are frequency encoded and can be switched on simultaneously. Frequency encoding is used in instruments with large number of sources to limit the acquisition time to acceptable range [33, 29]. However, in systems that use detectors for multi-distance measurements, the intensity from distant emitters is dominated by the shot noise from nearby emitters leading to a limited dynamic range.

The supporting control circuitry for light emitters depends on the type of NIRS instrument that one wants to build. Typically, the source driver circuitry in fNIRS systems consists of multiplexers, modulators and switches. For CW systems, a current-switching circuitry (multiplexer) can be sufficient. For FD systems, intensity modulation is also required. TD systems require extremely fast switches to toggle sources at high speed.

2.2.4 Light Detectors and Associated circuitry

There are a wide range of optical detectors available that can be used in fNIRS devices, including photodiodes (PDs), photomultiplier tubes (PMTs) and avalanche photodiodes (APDs). PMTs and APDs have internal amplification, which improves their performance for low-light applications, such as fNIRS measurements. PDs have no internal amplification, thus limited sensitivity. However, when taking into consideration cost and operating voltage, PDs can be a good option because their typical operating voltage ranges only a few volts with price range less than 1 euro per piece. While PMTs provide a faster response time and high sensitivity, they are bulky in size, require higher operating voltage in the range of kilovolts and they are very expensive, typically ranging between 1000 and 2000 euros. On the other hand, APDs provide the advantage of having a moderate operating voltage requirement in the range of 50 to 100 volts. They are also less expensive than PMTs costing only a few hundred euros.

Another type of detector is the silicon photon multiplier (SiPMs). SiPMs contain an array of small single photon avalanche diodes (SPADs) connected in parallel on a common substrate. SiPMs have the advantage of being small and having high sensitivity. Their typical operating voltage is in the range of 50 to 100 volts and a

price range of a few hundred euros. Studies show that using SiPMs as detectors can lead to improved SNR at longer SDSs [130, 82].

In a similar manner to the light emitters, the selection of the detector type is dependent on various factors, including the type of NIRS instrument, cost, size, response speed and power consumption. CW instruments can function using any of the available detector types, while TD and FD systems mainly use detectors with a fast response rate, such as PMTs and APDs. The precision, depth sensitivity and accuracy of the systems is highly dependent on the chosen detector. Moreover, the choice of detectors greatly affects the cost and portability of an fNIRS system.

The detector circuitry consists of amplification and demodulation stage, if applicable. Usually there is a preamplification stage using transimpedance amplifier (TIA) that converts the detected current into voltage. There can also be multiple amplification stages following the preamplifier to increase the signal to the range of the data acquisition (DAQ) unit. The DAQ unit converts the signal into a digital format and transfers it to a computer via a communication bus, such as USB, UART, bluetooth, wifi and Ethernet for further processing. DAQ units can be either generic DAQ cards or custom built using an ADC and a controller.

2.2.5 Sources of Noise

There are various sources of noise in fNIRS systems, including physiological oscillations (heart beat, blood pressure, respiration), motion-related artefacts, instrument noise (shot noise, dark current, Johnson–Nyquist) and enviromental noise (ambient light). These sources of noise should either be reduced to a minimum during instrument design and measurements or be removed in preprocessing steps to improve the reliability and accuracy of fNIRS instruments. [44, 48, 27]

For instance, motion-related artefacts and physiological oscillations can be regressed out from fNIRS data during preprocessing by simultaneously monitoring these parameters (eg., heart beat, motion). This can be done by using separate sensors to measure each of the sources of oscillations separately. Another method to reduce the impact of physiological oscillations is to simultaneously measure the backscattered light using detectors placed close to the source of light. Studies have shown that short distance measurements ($\sim$8 mm for adults and $\sim$2 mm in infants) are sensitive mainly to superficial tissue and this data can be used to regress the effect of physiological oscillations from other channels [91, 34, 18].

Instrument noise has various sources, including the quantum nature of photon (shot noise), current flowing in the detector in completely dark conditions (dark current), thermal noise resulting from moving charge carriers in electronic components, e.g., amplifiers and resistors (Johnson–Nyquist) and slow changes in the intensity of light. For detectors with internal amplification (PMT, SiPM and APD) there is an additional multiplicative noise factor which is known as excess noise factor resulting from the internal gain of the detectors [99]

Photon shot noise is equal to the square root of the number of detected photons. The shot noise follows a Poisson distribution similarly to the random arrival of photons to the detector surface. This noise is not completely avoidable. Nevertheless,

it can be kept to minimum by carefully shielding the detector from external stray light. Additionally, the effect of the shot noise can be reduced by taking more samples during measurements. [52]

Meanwhile, the effect of ambient light can be kept to a minimum taking some technical measures, including conducting experiments in dim rooms, using NIR bandpass optical filters, using an opaque light shield, and using lock-in detection techniques. In addition to reducing ambient light from reaching the detector surface, shielding with opaque material can help to prevent lateral radiation from sources. On the other hand, the lock-in amplification (detection) technique can be beneficial to recover very small signals overwhelmed by noise. The lock-in principle lies in modulating an input light signal with a reference signal of known frequency, locking-in (multiplying) the detected signal using the same reference signal used for modulation, and low-pass filtering this locked-in signal to extract only the low-frequency component [80]. In the past, various research groups have implemented this principle in their fNIRS systems to reduce the effect of background light and improve SNR [102, 24, 116].

2.3 Imaging using fNIRS: Diffuse Optical Tomography

A typical signal obtained from a multichannel fNIRS instrument is time series data of relative absorption changes due to the chromophore under investigation. Functional images can be reconstructed from these data by using sophisticated image reconstruction algorithms. Based on the type of image that can be reconstructed, instruments can be classified into two categories: optical topography and diffuse optical tomography (DOT) systems. In optical topography, measurements from multichannel fNIRS devices are used to reconstruct two dimensional surface maps of cerebral oxygenation and blood volume. In DOT, three-dimensional maps of oxygenation are reconstructed if information regarding depth is available. Fig. 6 shows a compact guideline on how to distinguish between the various fNIRS instruments.

As discussed in 2.2.1, in a reflective type fNIRS instrument light emitters and detector are placed next to each other with a separation of a few cm. In this geometry, the emitted light spends a considerable amount of the time travelling in non-brain (superficial) tissue before it is detected. This leads to the measured time series signal at the detectors being highly sensitive to haemodynamic changes in the superficial tissue. Multiple studies have demonstrated that the contribution of the signal arising from the brain increases with increase in SDS [70, 104, 68]. Measurements from multiple SDS combinations provide information from multiple layers of tissue. Fig. 7 illustrates this behaviour.

DOT instruments can make use of two strategies to obtain 3D maps of the cortex. These strategies are: using time resolved measurements and overlapping multi-distance measurements. Time-resolved systems [71, 97] function by time-gating the detected photons to profile different layers of tissue. Time resolved techniques require complex and expensive instrumentation. While the overlapping SDS measurement strategy [17, 98, 126, 123] uses measurements from multiple overlapping SDSs either

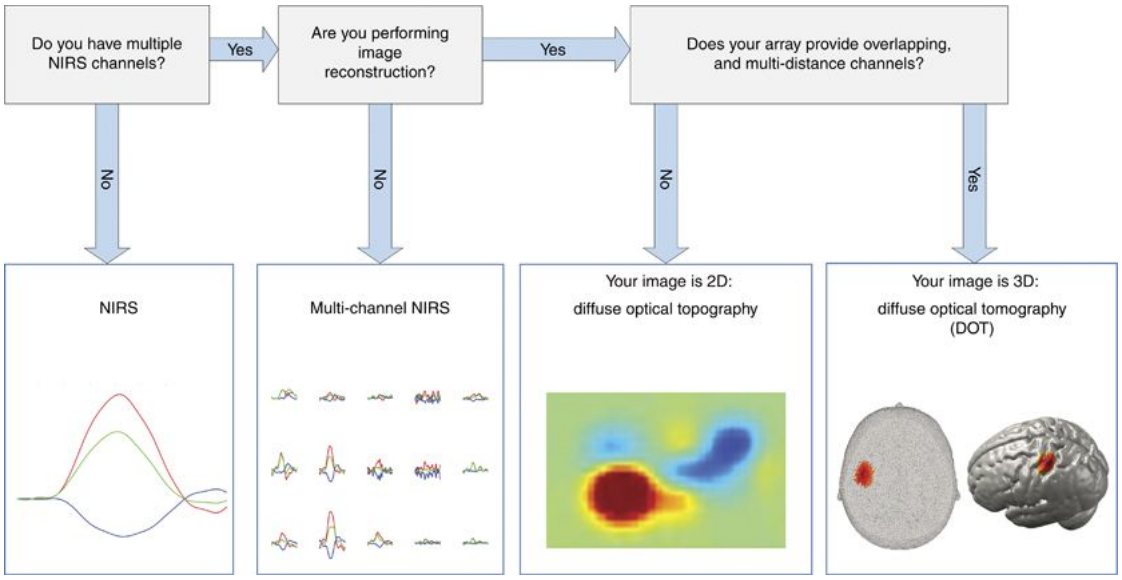

Figure 6: A decision chart used to classify fNIRS-based instruments based on the type of image aquired. Taken from [64]

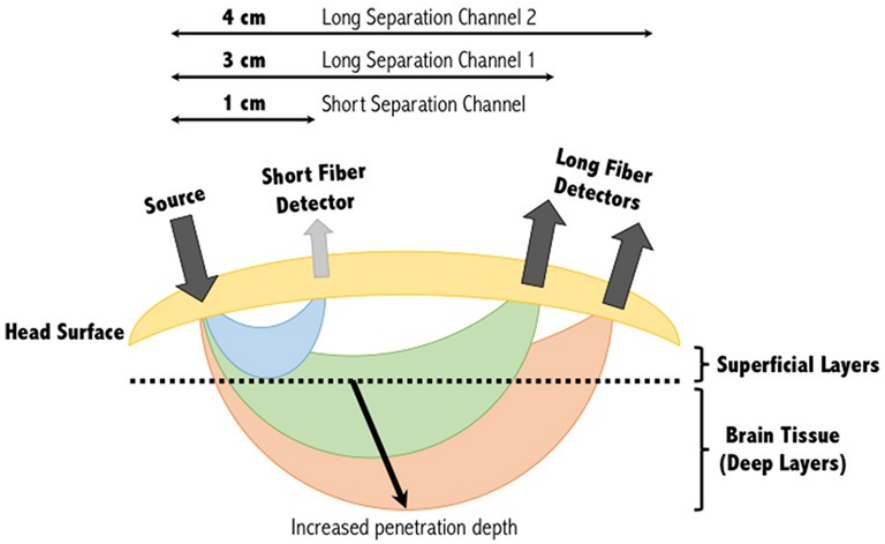

Figure 7: Illustration of the dependence of depth sensitivity on SDS. Adapted from [99]

with FD or CW techniques, TD and FD systems additionally give quantitative data which helps to determine baseline optical properties of tissue. Thus, the timing and phase information from FD and TD DOT is known to improve the quality of the reconstructed images. However, including the full time-resolved timing information in the reconstruction algorithm is known to increase computational time considerably [36]. In addition, the time-resolved data tend to be more noisy than the intensity

data. Moreover the instrumentation of TD and FD systems is bulky, sophisticated and expensive. These factors put practical limitations on optode density, channel count and cost on DOT systems to be implemented using FD and TD techniques. A study by Heiskala et al. [43] investigated various parameters, such as optode grid geometry and time-resolved vs intensity measurements on DOT image resolution. They found that the best resolution was obtained using high-density grid probes. In addition, overlapping SDS measurements are known to improve the lateral resolution and localization of DOT measurements. Hence, in the current technological state, CW instruments are the best option for building high density DOT instruments with reasonable cost for applications where the background optical properties are not necessary.

2.4 Key Application Areas

Currently, most cerebral haemodynamic measurements are conducted using fMRI device. However, compared to an fMRI device, fNIRS systems have multiple advantages, such as portability, cost efficiency and low movement sensitivity. These advantages make fNIRS potentially suitable for investigating the brain of neonates, children and schizophrenics who can not stay still in the confined space of an fMRI device. Unlike fMRI, fNIRS is also suitable for long-term monitoring of cerebral oxygenation and blood volume. fNIRS is also much cheaper than fMRI, which makes it potentially a suitable replacement when an fMRI system is not available, e.g., in clinics and remote areas [66]. In addition, fNIRS has a smaller size and can be nonmagnetic which makes it suitable for integration with other imaging modalities (MEG, EEG) and for studying the brain in a more naturalistic environment. This section reviews the applications of fNIRS systems in clinical environments, in research and in brain–computer interface systems.

2.4.1 Clinical Applications

Although fNIRS systems have not been fully adopted as a gold standard neuroimaging modality in clinical settings, it has been increasingly used for diagnosis and monitoring purposes. For instance, fNIRS has been used in intensive care units to monitor neonates. A significant number of death and brain injuries caused in this population are as a result of hypoxia–ischaemia. Studies have shown that monitoring the babies' cerebral oxygenation (cerebral blood flow, cerebral blood volume and cerebral oxygen saturation) using fNIRS can lead to early diagnosis and potential treatment [63, 30, 89, 14]. Additionally, cerebral metabolic rate of oxygen which is a good indicator of tissue viability, can be measured using diffuse correlated spectroscopy [112].

Besides its use in neonatal care, fNIRS has also been used in the monitoring of cerebral oxygen saturation in patients undergoing cardiac surgery. In these surgical procedures, cerebral hemoglobin oxygen saturation is monitored throughout the surgery to avoid cerebral ischemia. Various studies have shown that monitoring cerebral oxygen saturation using fNIRS during cardiac surgeries and carrying out

informed intervention have a positive clinical impact [4, 115].

The use of fNIRS has also been investigated for haematoma detection of after traumatic head injury (THI). The Infrascanner© [65] has been FDA approved for detection of cerebral haematoma. Clinical trials have investigated the applicability of the Infrascanner© for early detection of haematoma [76], intracranial lesions [101] and hemorrhages [25] after THI. These studies implied that fNIRS has a potential to be a routine diagnostic tool in emergency-care units for patients with THI as an adjunct to CT [84].

Some studies also indicate that fNIRS might be a useful tool in practical psychiatric settings involving both diagnostics and treatment efficacy evaluation. However, to adopt fNIRS as a diagnostic tool for brain disorders, there needs to be extensive investigation to identify fNIRS-detectable biomarkers for each specific condition. fNIRS instruments should also be developed by taking into consideration specific application areas.

2.4.2 Neuroimaging Research

fNIRS has been used extensively in neuroimaging studies. The majority of these studies have focused in functional activation studies (e.g., investigation of language and investigation of mental load). In these studies, the experiments are designed to target specific cognitive skills and to identify task-evoked brain responses. [122, 10, 85, 51, 67, 111]

The majority of neuroimaging studies are conducted in adults, which has created a knowledge gap regarding the developing brain. This is because studies with infants require a less confining experimental set-up than in adults, have higher ethical requirements and it is difficult to recruit subjects. The small instrument size, safety, quietness and the non-invasive nature of fNIRS make it suitable for use with infant neuroimaging experiments. A baby can stay in their parents' lap during an experiment, which is impossible during fMRI studies. Thus, fNIRS provides much needed neuroimaging data regarding the developing brain. There have been multiple fNIRS studies to investigate emotional, language and cognitive development of brain [51, 122, 67, 111, 61].

Most of the knowledge available regarding the human brain from neuroimaging studies is from experiments conducted in research environments, with carefully designed experiments. However, this knowledge is not sufficient when trying to understand the brain's response to mental tasks encountered in everyday environments. fNIRS is suitable for studying the brain in unrestricted naturalistic settings. For instance, fNIRS has been used to investigate the brain while subjects are performing real-world prospective memory tasks, playing table tennis, pedaling, playing a musical instrument and performing daily activities for many hours [85, 10, 86].

Multi-modal neuroimaging is the act of using two or more modalities simultaneously to acquire complementary information from the brain. The most common multimodal neuroimaging experiments are conducted by combining a direct (EEG, MEG) modality with an indirect (fNIRS, fMRI) modality to acquire information on both electrical activity of neurons and the related haemodynamic changes. fNIRS

provides multiple advantages for multi-modal imaging. Unlike fMRI, fNIRS probes can be designed to be nonmagnetic; thus, they are much easier to integrate in studies with MEG and EEG.

fNIRS-EEG multimodal imaging has been used for cognitive, behavioural and connectivity studies[11, 7, 12, 16, 3, 5]. In additon, fNIRS-EEG imaging has been extensively used for the epileptic brain research, as it provides additional information for presurgical planning, epileptic focus localization etc. [77, 83, 87, 119, 69, 35]. Additionally, concurrent fNIRS-MEG studies have been conducted for investigating the temporal relation between neuronal activation and haemodynamic changes (neurovascular coupling) [94, 100, 55].

fNIRS is also increasingly being used in brain–computer interface (BCI) systems. BCI systems are devices that measure brain activity and translate it into control signals used for a variety of applications, including aiding people with motor disabilities to control prosthetic limbs, providing a means of communication for people in vegetative state, for environmental control and in neuro-feedback studies. EEG is the most common imaging modality used in BCI applications. However, studies show that EEG-fNIRS BCIs perform better than EEG BCIs alone [24, 57, 31]. Moreover, a number of wearable hybrid fNIRS-EEG instruments have been developed for potential BCI use [54, 92, 96, 117].

Transcranial magnetic stimulation (TMS) is a non-invasive procedure in which a changing magnetic field is used to cause neuronal activation in the brain. TMS is a useful tool in neuroscience research. TMS has been found a useful tool in mapping of the human brain, for rehabilitation of the brain, for treating depression. Imaging using a non-magnetic fNIRS probe during TMS stimulation is helpful for measuring regional cortical brain activation and connectivity. [62, 28, 6, 39, 109, 74]

2.5 Existing Continuous-Wave Fiberless fNIRS and DOT Systems

Typical fNIRS systems are composed of two units: a probe consisting of an array of source and detector optical fibers and a control-data-acquisition unit consisting of a data acquisition circuitry as well as the necessary control electronics. This kind of arrangement has allowed for the design of fNIRS systems with sophisticated electronics to be easily implemented on table-tops with the use of optical fibers. The optical fibers deliver light to the scalp and from the scalp to the detectors. However, optical fibers are fragile, expensive and bulky. Resulting in a number of limitations, including inability to be used in naturalistic environments and increased discomfort for continuous monitoring applications (e.g., preterm baby monitoring, sleep apnea, BCI). To overcome these limitations, there has been a lot of progress in developing fiberless fNIRS and DOT instruments. Unlike TD and FD systems, the relatively simple instrumentation of CW systems allows for easier implementation of a fiberless arrangement. Thus, the recent progress has been mainly focused in developing CW systems. This section reviews some of the fiberless CW fNIRS and DOT instrumentation that has been developed in the past decade.

In a recent review Zhao et al. [129], have classified the architecture of fiberless

CW systems into three including: control-cabled, flexible-rigid and modular. Control-cabled architecture systems [56, 86, 96, 92, 15, 22, 20, 121, 33, 54, 123, 128] typically consist of two subsystems. One subsystem consists of the emitter–detector array, while another subsystem consists of control and communication units. The two subsystems are connected using a cable. On the other hand, flexible-rigid architecture systems [124, 125, 57, 75, 40, 2] typically consist of systems in a hybrid flexible-rigid printed-circuit-board (PCB). In the flexible part of the PCB light sources and detectors are placed. This allows the fitting of the probe to the curvature of the head. The rigid part of the PCB contains the control and data acquisition circuitry. Modular architecture systems [117, 21, 130, 1] are systems that consist of small and scalable modular units that can be combined to create a larger system. Modular systems include both the source–detector array and control circuitry in the same module. Table 3 shows a summary of the reviewed CW fiberless fNIRS instruments.

Table 3: Existing fiberless fNIRS and DOT systems. Modified from [129]

Author year [citation]	Architecture	Number of source/detector locations	Emitter, Detector Wavelengths (nm)	SDS (mm)	Demonstrated number of optical channels
Yurtsever et al. 2003 [124, 125]	Flex-rigid potentially modular	4/10	LED, PD 730, 850	25	-
Muehlemann et al. 2008 [75]	Flex-rigid potentially modular	4/4	LED, PD 760, 870	12.5 to 37.5	16
Kim et al. 2011 [57]	Flex-rigid potentially modular	3/8	LED,PD 780, 850	35	fNIRS
Kiguchi et al. 2012 [56]	Control-cabled	8/8	LD, APD 754, 850	30	22
Piper et al. 2013 [86]	Control-cabled	8/8	LED, PD 760, 850	25	20
Sawan et al. 2013 [96]	Control-cabled	8/8	LED, APD 735, 850	31	32
Safaie et al. 2013 [92]	Control-cabled	8/4	LED, PD 760, 850	20 to 63	32
Zimmermann et al. 2013 [130]	Modular	1/1 per module	LED, SiPM 680, 850	20 to 50	2
Bhutta et al. 2014 [15]	Control-cabled	3/8	LED, PD 640/700/910	30	12
Hallacoglu et al. 2016 [40]	Flex-rigid potentially modular	10/18	LED, PD 690 to 850 (5 wavelengths)	13 to 55	180

Choi et al. 2016 [22]	Control-cabled	4/6 per module	LD, PD 780, 850	-	14
Chitnis et al. 2016 [21]	Modular	1/4 per module	LED, PD 750 to 900 (8 wavelengths)	36, 42	4
Abtahi et al. 2016 [1]	Modular	4/4 per module	LED, PD 770, 830	30	10
Agrò et al. 2016 [2]	Flex-rigid potentially modular	4/16 per module	LED, SiPM 735, 850	15 to 30	-
Von Lühmann et al. 2017 [117]	Modular	2/2 per module	LED, PD 750, 850	35/30	4
Chiarelli et al. 2017 [20]	Control-cabled modular	1/1 per module	LED, SiPM 735, 850	15 to 60	6
Wyser et al. 2017 [121]	Control-cabled modular	4/1 per module	LED, SiPM 770, 810, 850, 885	7.5, 40	4
Funane et al. 2017 [33]	Control-cabled modular	12/23	LED, APD 730, 855	30	-
Kassab et al. 2018 [54]	Control-cabeled potentially modular	32/32	LED, APD 735, 850	30	128
Zhang et al. 2018 [128]	control-cabled modular	-	LED, PD 760, 850	-	-
Saikia et al. 2018 [93]	control-cabled	8/16	LED, PD 750, 810, 850	40	128)
Yaqub et al. 2018 [123]	control-cabled	128/4	LED, PD 735, 850	0.5 to 3.5	128

As can be seen from Table 3, majority of the reviewed systems make use of LED-PD combinations as sources and detectors [124, 125, 1, 123, 93, 128, 75, 117, 86, 40, 92]. Although the low power need of PDs' makes them attractive for fiberless applications, they have relatively low sensitivity and require a high level of amplification which increases system noise. Some of the systems [117, 128, 124, 1, 125] use a monolithic PD with built-in amplification to reduce the noise introduced by the additional amplification.

Although it is known that APDs are more sensitive than PDs, they require a high bias voltage in the range of few hundred volts, which raises safety concerns when used in fiberless fNIRS probe designs. As a result, only a few of the reviewed fiberless systems use APDs as detectors [33, 54, 56, 96].

SiPMs on the other hand are relatively newer range of detectors in the market and not much is known about their applicability in fNIRS instruments. Thus, only a

few of the fNIRS systems make use of SIPMs[130, 121, 20, 2]. However the lower bias voltage (few tens of volts) and high sensitivity of SIPMs make them an attractive detector choice for fiberless fNIRS instrumentation design.

The majority of the reviewed instruments use a microcontroller and ADC based DAQ units [1, 57, 117, 75, 121, 15, 130, 2, 123]. Meanwhile some systems use field programmable gate array and ADC for their DAQ systems [96, 92]. In addition, most of the systems except a few are wireless and battery powered, which gives them even more flexibility. However, only a portion of the reviewed systems are DOT systems with multi-distance measurement capabilities [123, 20, 2, 121, 21, 40, 130, 92].

3 Solution Development

This section discusses the design procedure used to build a prototype of a fiberless DOT instrument based on silicon photomultipliers. Section 3.1 gives an overview of the designed prototype. Section 3.2 discusses the detailed hardware design of the instrument. Finally, section 3.3 discusses the detailed software design of the designed instrument.

3.1 System Overview

The designed DOT system prototype consists of two printed-circuit boards (PCBs), a JTAG programmer, a high-voltage power supply and a LabView-based graphical user interface (GUI). The first PCB is a DOT sensor unit which consists of source–detector arrays and a preamplifier for the detectors. The DOT sensor PCB consists of three dual-wavelength LEDs, three PDs and three SIPMs. This PCB is connected to the second PCB using a data and power cable.

The second PCB is a data acquisition and control (DAQ-C) unit consisting of an ADC, a dual-core microcontroller, a constant-current LED sink driver as well as on-board voltage regulators. The DAQ-C unit is connected to a PC by a debugger (TMDSEMU110). This debugger is used to transmit data to and from a computer and supply power to the DOT system. Additionally, a high voltage power supply is used to meet the high power demand of the SiPM detectors. Fig. 8 shows a detailed block diagram of the developed system.

3.1.1 Lock-in Detection

In the current design, the lock-in detection technique is implemented to reduce the effect of ambient light on the measured signal. It is a technique used to extract signal overwhelmed by noise by modulating the input of a system by a known reference signal and locking-in (multiplying) the output of the system by the same reference signal and finally low-pass filtering this signal.

The lock-in technique can be implemented by using either analog components or digitally. In the current design, a digital lock-in scheme was implemented. In this scheme, the LEDs' output light intensity was modulated using a reference square wave signal of a few kHz. This modulated signal was then detected by detectors and was transferred to a computer. Afterwards, during post-processing, the demodulation of the detected signal is performed. During demodulation, the detected was multiplied by the reference signal and was low-pass filtered to extract information from a narrow bandwidth around the frequency of interest only.

3.1.2 Optode Geometry

The DOT sensor unit optode arrangement was designed to conduct multi-distance measurements. The sensor unit has ten channels, of which three are short-distance channels with SDS of 1 cm, two are intermediate-distance channels with SDS of 3 cm

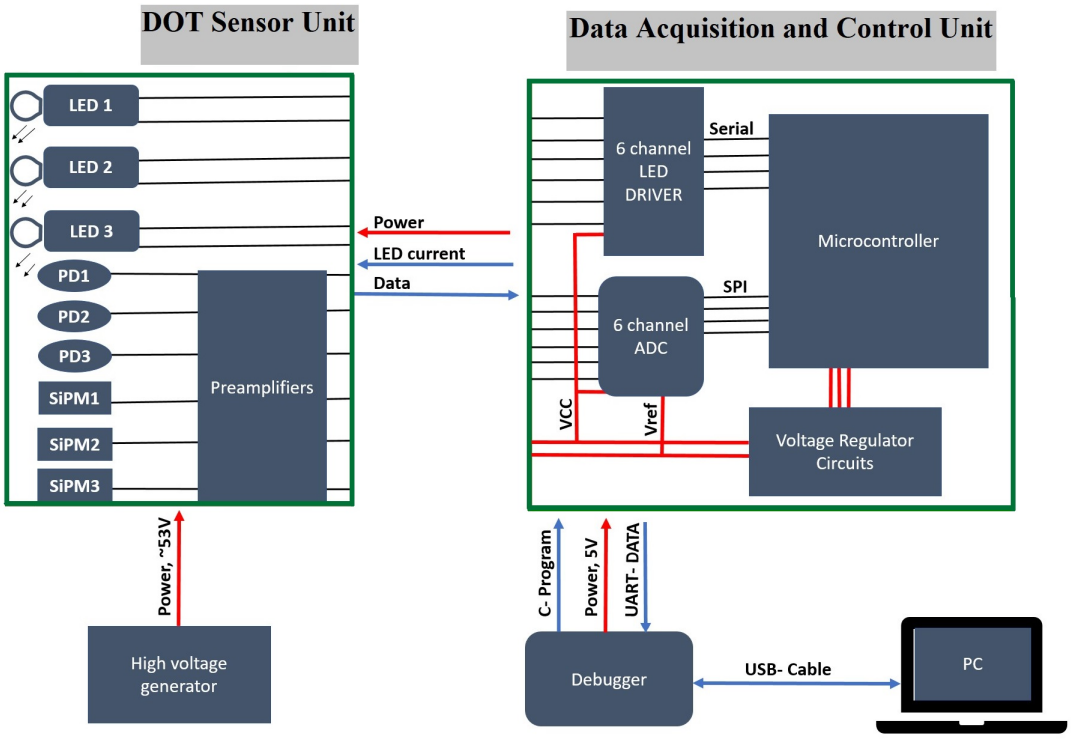

Figure 8: Block diagram of the designed DOT instrument

and three are long-distance channels with SDS of 4.5 cm. The geometry of the DOT probe is shown in Fig. 9.

3.2 Hardware Design

3.2.1 Light Emitters

In the DOT sensor PCB, three L760/850-04A common-anode bi-color LEDs from Epitex Electronics were used as light source. These LEDs consist of two wavelengths in one package with peak emissions at 760 nm and 850 nm with spectral band-width of $\pm$ 30 to 35 nm. The output radiated power is in the range of $8 - 15$ mW for 760 nm and in the range of $12 - 18$ mW for 850 nm at 50 mA forward current. The radiated power varies almost linearly with forward current, thus by doubling the forward current to 100 mA one could get an output power between $16 - 30$ mW at 760 nm and $24 - 36$ mW at 850 nm. The LEDs were were time-multiplexed and modulated with a square-wave signal using a constant-current driver TLC5916 from Texas Instruments. This driver is discussed in more detail in the next section.

3.2.2 Constant Current Driver

The TLC5916 is an eight-channel current-sink driver chip used for time multiplexing and modulating the three dual-wavelength LEDs. This driver is suitable for time multiplexing and modulation because each output channel can be switched on or off

independently. The driver's constant sink current for all channels is adjusted using an external resistor and an eight-bit configuration code. The relationship between the output current and the value of the external resistor is shown in Fig. (10). In the current design R_{ext} is set to be 188 Ω, resulting in a maximum output current of 100 mA.

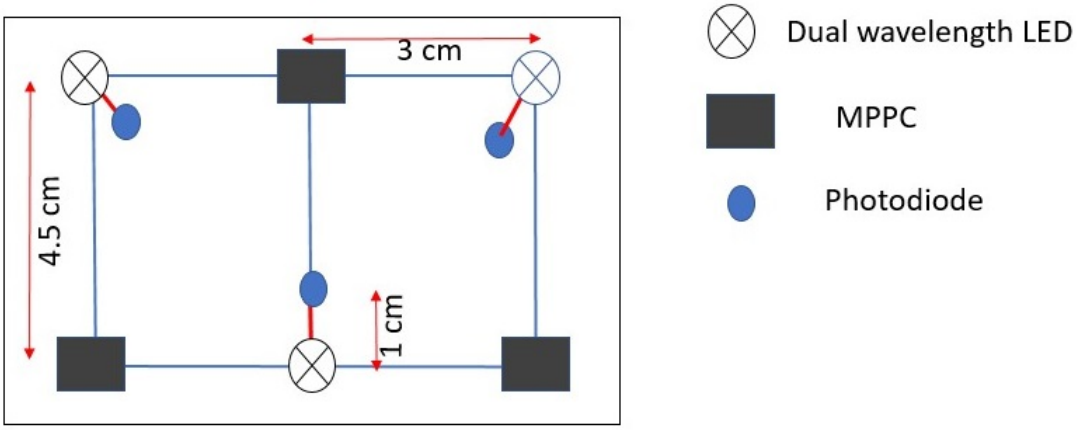

Figure 9: The optode arrangement in the DOT sensor PCB

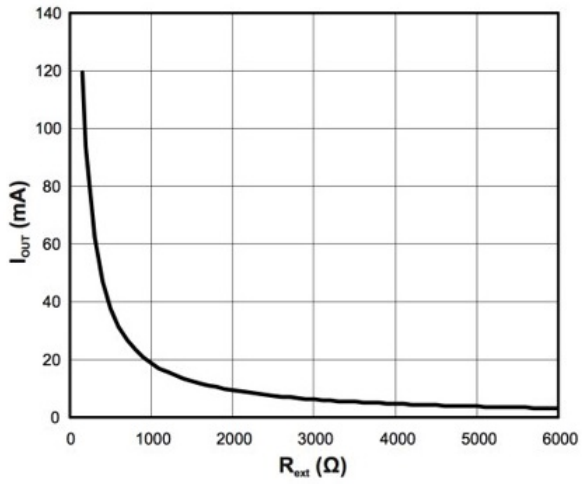

Figure 10: LED driver external resistance vs output current [108]

This driver has two functional modes: normal mode and special mode. In normal mode, the driver output channels can be selected using an 8-bit configuration code. In special mode, the value of the output current can be adjusted using an 8-bit configuration code allowing the output current to be finely set (Fig. A2). This gives flexibility to calibrate LED intensity according to different use cases. Thus, it is possible to avoid the saturation of detector circuitry. The detailed functional block diagram of the TLC5916 is given in Appendix A1.

This driver was controlled using a microcontroller. The two were interfaced using a three-wire serial communication protocol as well as additional digital pins,

latch-enable (LE) and output-enable (OE). The LE pin is used to latch out an input command into a shift register. The OE pin is used to enable output on selected LED output channels. By toggling OE, the LEDs can be modulated. Fig. 11 A. shows the circuit diagram of the connection between the LEDs and the led driver. Fig. 11 B. shows the modulation and time multiplexing timing diagram.

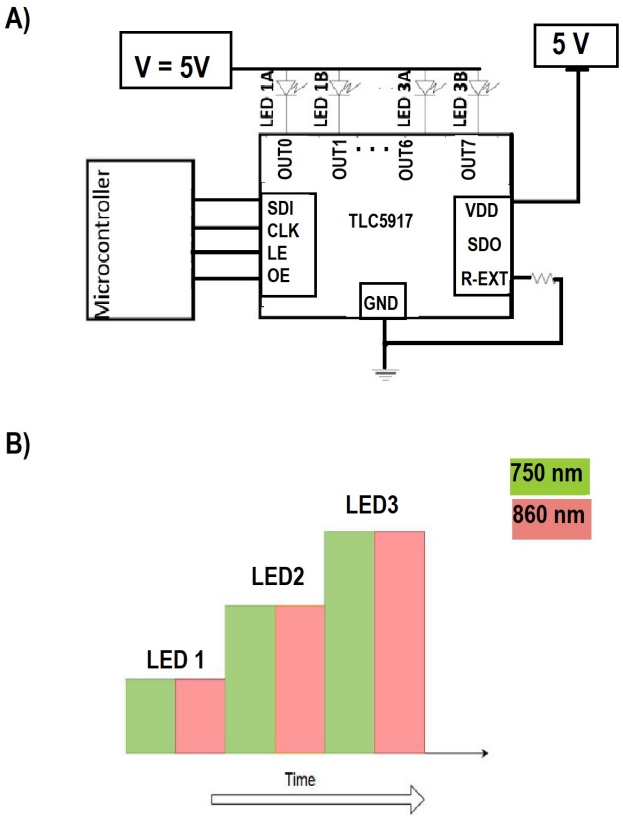

Figure 11: A) LED Driver Circuit B) Time multiplexing and modulation of the LED current

3.2.3 Light Detectors

Two types of detectors were used in this design: PDs and SiPMs. Three SFH 229 PDs, from Osram Opto Semiconductors, were placed approximately 1 cm from each LED for short-distance measurements. This PD have a small photosensitive area of 0.31 mm^2 with peak spectral sensitivity 0.62 A/W at 860 nm (Fig. 12.A). This PD has a maximum dark current of 5 nA at 10 V reverse bias. The dark current is directly proportional to the PD bias voltage and temperature. This behaviour can be seen in Fig. A3.

A multi-pixel photon counter (MPPC) SiPM S13360-6050CS, from Hamamatsu Photonics, was used for distances of 3 cm and 4.5 cm. This MPPC has a large photosensitive area of 36 mm^2 consisting of 3600 pixels each with pitch of 50 μm. This large area is useful to detect as many photons as possible in low-light conditions.

The peak sensitivity of the MPPC is at 450 nm with 40% photon detection efficiency (PDE). At wavelengths 760 nm and 850 nm this number drops to 6% and 10% respectively (Fig. 12.B).

The MPPC has an internal gain of 1.7 x 10^6 with a maximum dark count rate of 6000 kcps and 3% cross talk probability. The MPPC gain, PDE and cross talk probability are dependent on the operating voltage (V_{op}) (Fig. A4). The MPPC is operated at a few volts higher (V_{ov}) than the breakdown voltage (V_{Br}) of the P-N junction of individual pixels. V_{Br} increases with increase in ambient temperature. This leads to MPPC output non-linearity in applications where the ambient temperature cannot be controlled and V_{op} is constant. The temperature dependence of dark current with temperature is shown in Fig. A5. The MPPC has a temperature compensation coefficient (ΔV_{op}) of 53 mV/^{0}C. This can be used to dynamically adjust V_{op} based on input from temperature sensor.

In the current design, a temperature sensor was placed in the DOT sensor PCB to monitor the temperature of the MPPCs. The output of the the temperature sensor was intended to to adjust the SiPM high voltage supply output. The supply used in this design was specifically designed for SiPMs. This supply is discussed in Section 3.2.9.

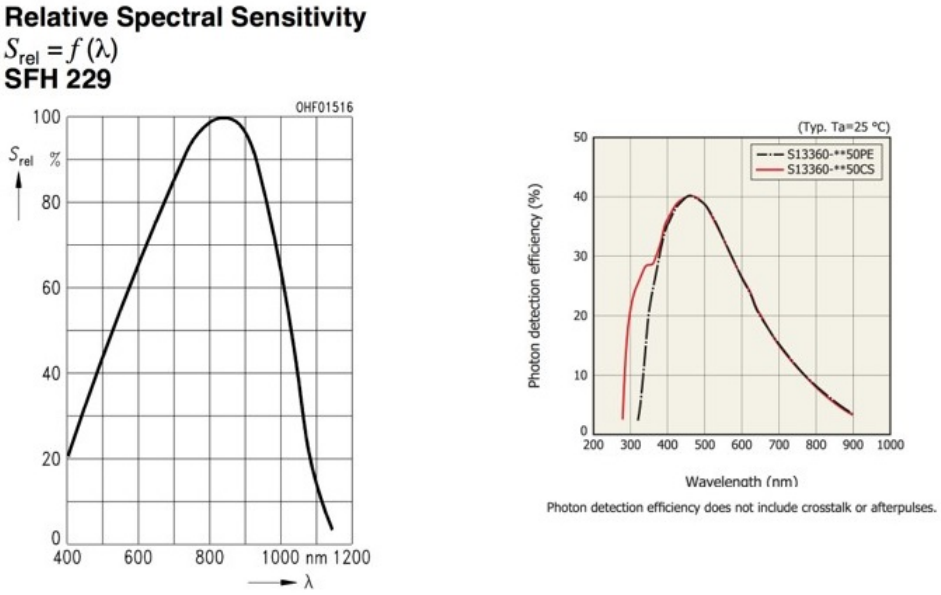

.

Figure 12: A. Spectral response of SFH 229[81] B. Photon detection efficiency vs wavelength of $S13360-6050CS$ [41]

3.2.4 Preamplifier

This design uses a single level amplification using a transimpedence amplifier (TIA). A TIA is an amplifier which converts current into voltage using a feedback resistor

(R_F). The output of a TIA is given by $V_{out} = I_{in}$ x R_F. Fig. 13 shows the circuit diagram of a typical TIA amplifier.

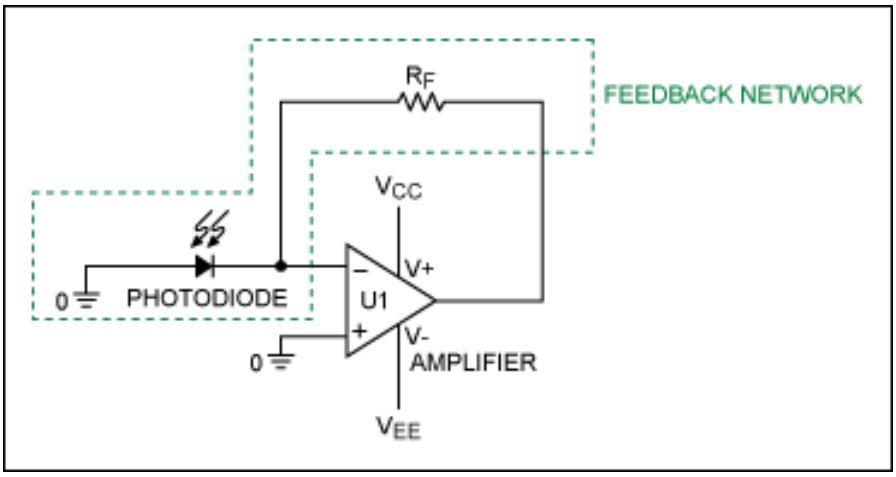

Figure 13: A typical transimpedence amplifier.

A suitable operational amplifier (op-amp) for the TIA was chosen based on multiple factors, including high bandwidth, minimum input noise and gain. The op-amp needs to operate with single supply, and low power. The bandwidth of the signal at the detectors considering maximum square wave modulating frequency 4 kHz and the first 5 harmonics contributing for $> 95\%$ total power is approximately 20 kHz, the final bandwidth of the TIA circuit needs to be above this value.

The gain of the TIA was chosen based on the ADC's dynamic range. The ADC's properties are discussed in detail in section 3.2.5. The necessary gain for the TIA was calculated by estimating the maximum possible current at the detectors. For the MPPCs this was extracted from phantom and in vivo measurements conducted in a previous study [127]. The maximum current of 300 μA was obtained from phantom studies. For the PD, it is expected to obtain maximum current of 500 nA assuming 50 μW to 100 μW optical power at the surface. These values need to be amplified to a range of 2.4 V which is the maximum amplitude that the ADC can convert. Thus, from this the gains were set to be 133 dB and 74 dB, using forward resistors of 4.5 MΩ for 5 kΩ the PDs and for the MPPCs respectively.

The TIA was designed using the TLV2374, a 4 channel op-amp from Texas Instruments. The op-amp has a unity-bandwidth of 3 MHz, a very low input noise of $39\frac{\text{nV}}{\sqrt{\text{Hz}}}$ and a low input bias current (1 pA). The final bandwidth of a TIA circuit is inversely proportional to the gain. Thus, a TIA design is a compromise between bandwidth and gain.

TIA circuits have stability problems such as ringing, gain picking and excessive high frequency noise. These problems can be reduced by placing a feedback capacitor (C_F) in parallel with R_F. The optimum C_F in the current design was chosen using simulations done on Tina TI SPICE-based analog simulation program. In the simulations, the detectors behaviour was modelled as a current source in parallel with a junction capacitor. The electrical models used for the feedback capacitor

selection are shown in Fig. 14.

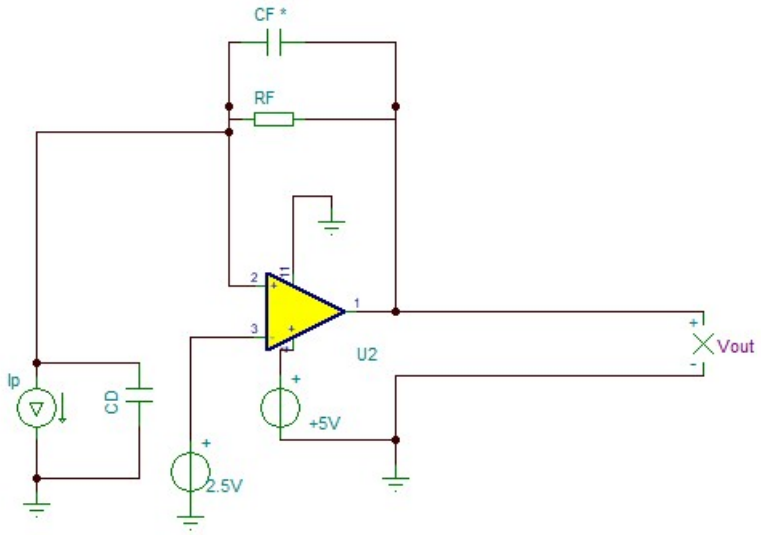

Figure 14: A TIA model used for identifying the appropriate feedback capacitance

The results from the simulation are shown in Fig. 15 and 16. From this the C_{F} was chosen with enough bandwidth to allow the modulated light be detected without distortion and minimum output noise.

From these simulations, C_{F} was chosen to be 0.8 pF for the PD TIA and 220 pF for the MPPC TIA. The final achieved bandwidth was calculated using Equation 4. The final gain bandwidth was $\sim$ 72 kHz for the PD TIA circuits and $\sim$ 260 kHz for the MPPC TIA circuits.

$$f_{-3\mathrm{dB}} = \sqrt{\frac{GBWP}{2piR_{\mathrm{F}}C_{\mathrm{IN}}}} \tag{4}$$

where:

- $GBWP$ is the amplifier's gain bandwidth product
- $f_{-3\mathrm{dB}}$ is the -3 dB bandwidth of the amplifier
- R_{F} is the feedback resistance
- C_{IN} is the total input capacitance given by $C_{\mathrm{IN}} = C_{\mathrm{CM}} + C_{\mathrm{diff}} + C_{\mathrm{D}}$, C_{CM} is the amplifiers common mode capacitance, C_{diff} is is the amplifiers diffrential capacitance and C_{D} is the detectors junction capacitance $C_{\mathrm{IN}} \approx 30$ pF and $C_{\mathrm{IN}} \approx 1.3$ nF for SFH 229 and S13360 – 6050CS respectively.

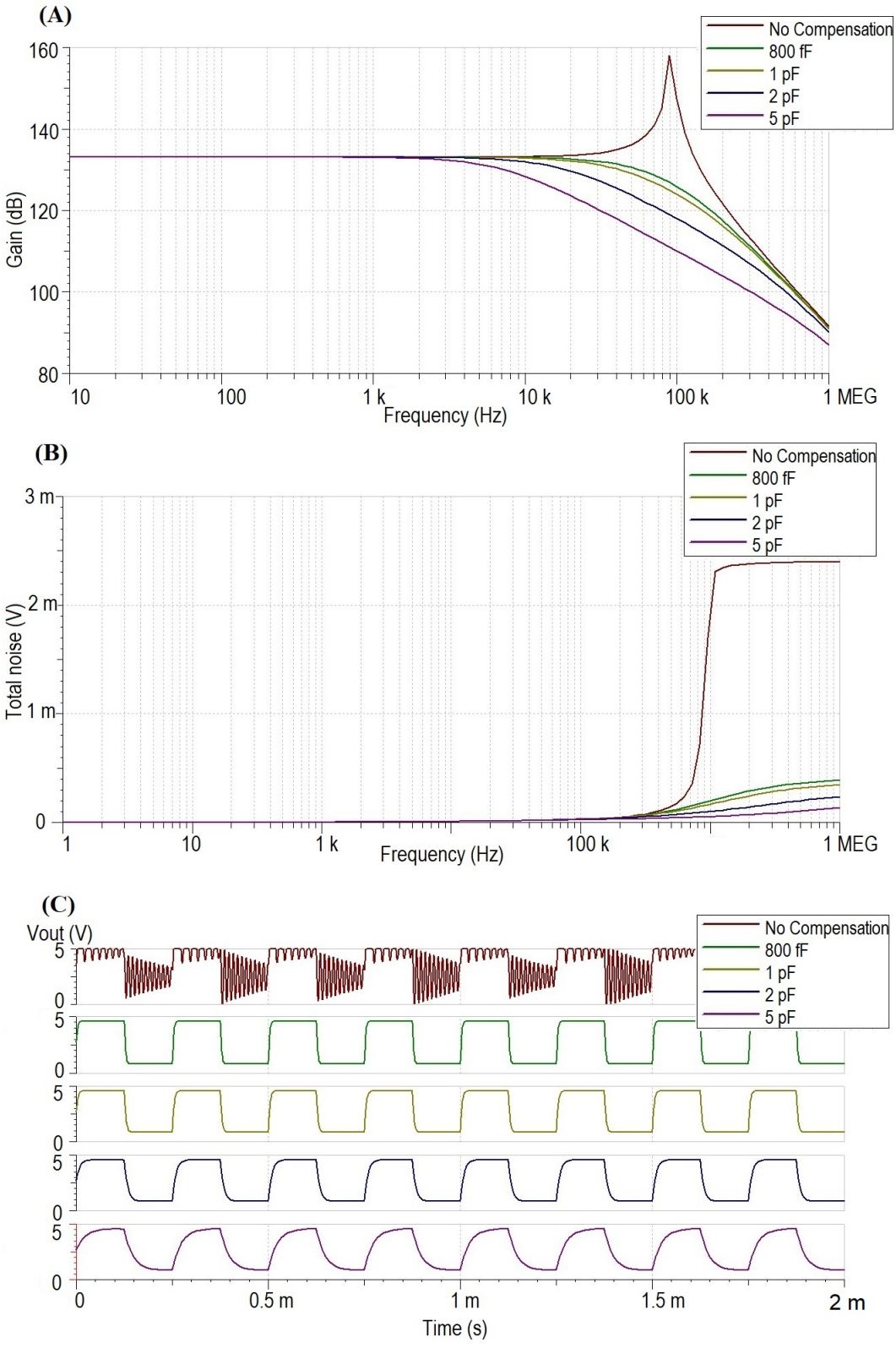

Figure 15: Simulation results for the photodiode with $R_{\mathrm{F}} = 4.5$ MΩ, 4 kHZ input square wave current and junction capacitance $C_{\mathrm{D}} = 11$ pF. The AC transient response (A), the total noise (B) and the transient response (C) are shown.

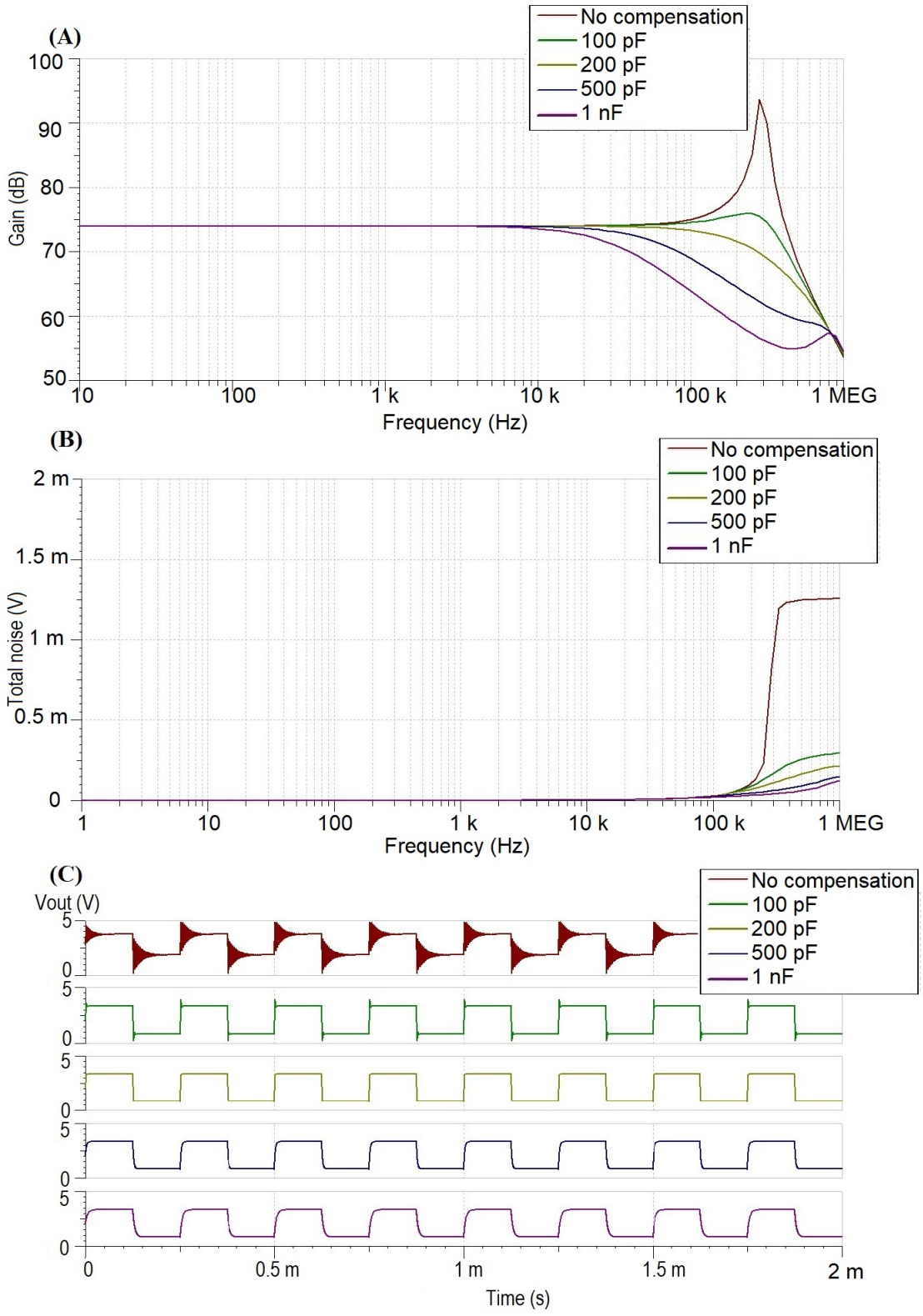

Figure 16: Simulation results for the MPPC with $R_{\mathrm{F=4\ k\Omega}}$, 4 kHz input square wave current and junction capacitance $C_{\mathrm{D=1.28\ nF}}$. The AC transient response (A), the total noise (B) and the transient response (C) are shown.

As discussed in section 2.2.5 there are various source of instrumentation noise. In TIA circuits this noise can result from four sources such as (1) a noise current term which results from the inverting input current noise of the op-amp (2) a noise voltage term resulting from input non inverting voltage noise of the op-amp (3) a thermal noise term resulting from R_F (4) an input capacitance term which results from the equivalent input capacitance of the TIA circuit. Equation 5 denotes the equivalent noise of a typical TIA circuit.

$$i_{ni} = \sqrt{i_n^2 + \left(\frac{e_n}{R_F}\right)^2 + \frac{4kT}{R_F} + \frac{(e_n 2\pi f_{-3dB} C_{IN})^2}{3}} \tag{5}$$

where:

- i_n is the inverting input current noise and is the same as the current noise term
- e_n is non-inverting input voltage noise
- R_F is the feedback resistor
- k is the Boltzmann constant = 1.38 x 10^{-23}J/^{0}K
- T is temperature
- C_{IN} is the total inverting input capacitance
- f_{-3dB} is the total inverting input capacitance
- $\left(\frac{e_n}{R_F}\right)$ is the voltage noise term
- $\sqrt{\frac{4kT}{R_F}}$ is the thermal noise term
- $\frac{(e_n 2\pi f_{-3dB} C_{IN})}{3}$ is the input capacitance noise term

The equivalent noise values for the designed TIA circuit were calculated using Equation 5. The specifications of the designed TIA circuits is given Table 3.2.4. This table shows the final total noise and the achieved SNR of the designed TIA circuit.

Table 4: The designed TIAs' characterstics

	GBWP	3 MHz
	Inverting input current noise (i_n)	0.0006 $\frac{pA}{\sqrt{Hz}}$
	Non-inverting input voltage noise (e_n)	39 $\frac{nV}{\sqrt{Hz}}$
	Op-amp input capacitance	$\sim$ 10 pF
SFH 229	R_F	4.5 MΩ
	Junction capacitance	11 pF
	Noise current term	0.0006 $\frac{pA}{\sqrt{Hz}}$
	Noise voltage term	0.0086 $\frac{pA}{\sqrt{Hz}}$
	Thermal noise term	0.06 $\frac{pA}{\sqrt{Hz}}$
	Input capacitance noise Term	8.48 $\frac{pA}{\sqrt{Hz}}$
	SNR calculated for a minimum expected current $\sim$ 10 nA and total spot noise calculated using Eqn. 5	61 dB
MPPC	R_F	5 kΩ
	Junction capacitance	1.3 nF
	Noise current term	0.0006 $\frac{fA}{\sqrt{Hz}}$
	Noise voltage term	7.8 $\frac{pA}{\sqrt{Hz}}$
	Thermal noise term	1.8 $\frac{pA}{\sqrt{Hz}}$
	Input capacitance noise term	551 $\frac{pA}{\sqrt{Hz}}$
	SNR calculated for minimum expected current of 0.5 μA and total spot noise calculated using Eqn. 5	59 dB

3.2.5 Analog to Digital Converter

The TIA data was converted into digital form using ADS131E08 ADC from Texas Instruments. This ADC is a delta-sigma converter with a resolution up to 24 bits. This ADC consists 8 simultaneously sampling channels, programmable gain amplifier (PGA) with 12 gain settings, an electromagnetic interference (EMI) filter, two selectable internal reference levels (2.4 V and 4 V) as well as seven selectable data rate (f_{Dr}) levels up to 64 kS per second per channel. The functional block diagram of this ADC is shown in Fig. A6.

The ADC has a low input referred noise (Fig. A8 A and B). The dynamic range, effective number of bits (ENOB) and the -3 dB bandwidth of the ADC are dependent on the output data rate (f_{Dr}) as well as the PGA gain as can be seen in Fig. A9. The -3 dB bandwidth of the ADC's conversion is approximately $\sim 0.25 f_{Dr}$ (Fig. A7 A and B).

In this design an RC filter with cut off frequency of 60 kHz was used to avoid any aliasing. The ADC was used in pseudo-differential mode. In this mode the negative input channel (INnN) was connected at mid supply, i.e., 2.5 V bias voltage. The ADC's internal reference voltage of 2.4 V was used for conversion. In this arrangement, the ADC can convert input voltages ranging from -2.4 V to 2.4 V.

The signal flow diagram is shown in Fig. 17.

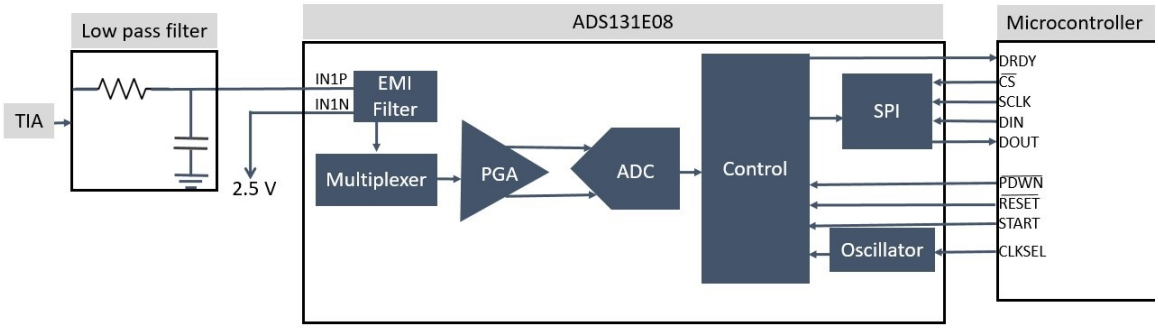

Figure 17: Summary of over all signal pathway

3.2.6 Microcontroller

A dual-core microcontroller TMS320f28379D from Texas Instruments is used for controlling the ADC and LED current driver as well as to communicate with a computer. This controller was chosen for this application because of its high speed and because it has two CPU subsystems (CPU1 and CPU2) which are suitable for running parallel programs. The CPUs in this controller are based on C28x, a 32-bit fixed-point processor. This controller has multiple subsystems, including the analog subsystem, three serial peripheral interface (SPI) ports, two serial communication interface (UART) ports, an enhanced capture unit and an inter processor communication module (IPC). These subsystems have access to interrupts. An interrupt is a signal that causes the CPU to pause its current execution and start executing a different program known as an interrupt service routine (ISR).

The IPC module is used by the two CPUs to communicate with each other. The IPC consists of two 2 kB shared memories (RAMs). These shared RAMs can be used to transfer data between the two CPUs. Only one CPU can have both write and read access to the shared message RAM while the other CPUs access would be limited only to reading the RAM only. In addition to the shared message RAM, the IPC contains multiple flag and interrupt sources which can be used to generate IPC interrupts on the remote CPU to notify the remote CPU that an event has occurred. The IPC also has a 64-bit free-running counter which can be used to time stamp IPC events between processors.

The controller is programmed using a JTAG debug probe TMDSEMU110-U XDS110 also from Texas Instruments. This probe is used to program and debug the micro-controller as well as to transmit UART data to computer. Additionaly, the probe can supply power for the designed system. The probe is connected to the controller using a 20-pin compact JTAG cable, which used for programming. There was an additional 14-pin IDC connection between the probe and the DAQ-C PCB used for UART communication and supplying probe. The probe was connected to a computer using a USB cable.

Table 5: Power requirements of system components

Component	Supply type	Voltage (V)	Current (mA)		
			min	Typical	maximum
Microcontroller (TMS320F28379D)	Analog supply(V_{DDA})	3.3	-	13	20
	Digital logic (V_{DD})	3.3	-	325	495
	GPIO supply (V_{DDIO})	2.3	-	30	-
	Flash supply (V_{DD3VFL})	3.3	-	33	40
ADC (ADS131E08)	Analog Supply (A_{VDD})	5	-	5.8	-
	Digital core supply (D_{VDD})	3.3	-	1	-
	Negative input offset (V_{INn})	2.5	-0.01	-	0.01
LED curent driver (TLC5916)	Supply voltage (V_{DD})	5	19	-	24
Op-amp (TLV2374)	Supply VCC	5	-	0.55	0.66
	Positive input offset	5	-	0.001	-
LED (L760-850)	Forward voltage(V_{DD})	5V	-	-	100
MPPC (S13360-6050CS)	Bias voltage	53V_{bias} (typical)	-	-	1

In the current design, two of the existing SPI ports of the controller are used to configure the ADC and LED driver. A UART port is used for communicating with a computer. In the current design an external oscillator was used to generate a stable clock source. The schematics for these circuits can be seen in Figs. A14-A16.

3.2.7 On-board Power Regulators

In the designed system, different circuits have different power needs. Most of the circuits except MPPC detectors are capable of operating at low power $\leqslant 5$ V. Table 3.2.7 shows the power requirements of the different components. For the low power circuits, a 3.3 V supplied from the debug probe was regulated to the various required voltage levels. However, the MPPC detectors have a high voltage requirement. Thus, a separate high voltage SiPM supply from Nuclear Instruments was used as a supply.

As can be seen from Table 3.2.7, four voltage levels (5 V, 2.5 V, 3.3 V and 1.3 V) are needed for different parts of the system. In order to fulfil these requirements, on-board power regulators were implemented. These regulators were designed based on a reference design provided by Texas Instruments [107]. A 3.3 V was regulated using a step-up and a step-down regulators. The step-up regulator circuit was designed to convert the 3.3 V to 5 V using a boost switching regulator LMR62421XMF. The step-down regulator circuit was designed to convert the 3.3 V to 1.2 V using the TPS62080ADSGT buck switching regulator. At last, a voltage divider circuit was designed to supply the 2.5 V for the op-amp and ADC using the MPMT2001AT1 resistor network. The circuit diagram for the power regulators is shown in Fig. A13.

3.2.8 PCB Layout Design

As mentioned in Section 3.1, the developed system consists of two PCBs: DOT sensor and DAQ-C. Both PCBs are designed for low noise and environmental interference. Both PCBs consist of four layers. The DAQ-C PCB was designed by using separate return paths for digital and analog currents. Thus, one layer was dedicated for analog ground and another for digital ground. This helps to prevent high frequency digital signals from interfering with analog signals. Additionally high frequency components and low frequency components were placed in different sections of the PCB for further reducing interference. The other two layers were dedicated for power and signal.

The DOT sensor PCB doesn't contain digital components, nevertheless, this PCB contains both high voltage and low voltage levels. Thus separate polygons dedicated for high ($\sim$ 50 V) and the low voltage (5 V) were used. In the DOT sensor PCB, the first layer was dedicated for power, the second and fourth layer were dedicated for ground plane, and the third layer was dedicated for signal. The layouts for for both PCBs, the bill of material and schematics are shown in A.5.

3.2.9 SIPM Power

The NIPM12, a high voltage regulator specifically designed for SiPMs was used for biasing the three MPPCs. This supply has a built in temperature compensation controller with a programmable coefficient. The module was digitally controlled by a UART and Zeus windows compatible software. The NIPM12 can provide up to 10 mA current and the output voltage could be regulated between 20 V and 85 V with a resolution of 1 mV. The Zeus interface can be used to continuously monitor the voltage and current consumption.

3.3 Software Design

The software design of this system consists of two main units. One unit is a C-code running in a microcontroller to control the ADC and LED driver as well as to communicate with a computer. The other unit is a graphical user interface that stores and visualizes data on the computer. A detailed overview of the software flow is shown in Fig. 18.

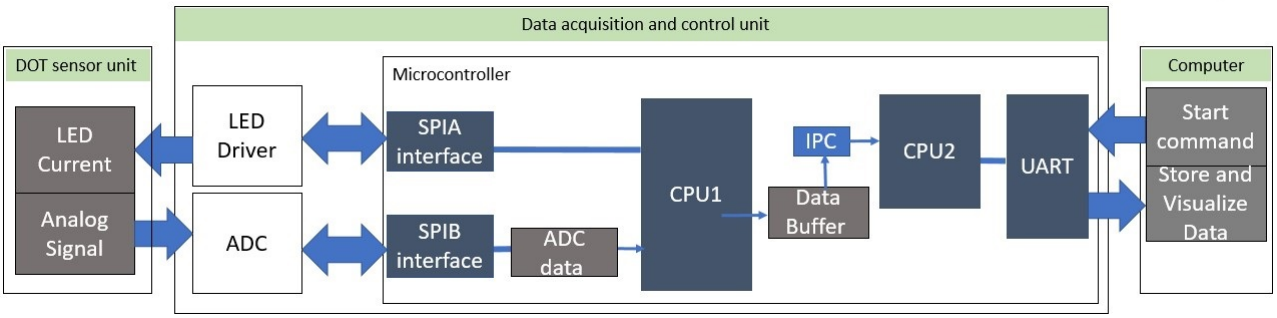

Figure 18: Block diagram of the detailed software overview.

3.3.1 Data Acquisition and Control Software

The data acquisition and control software for this application runs from the microcontroller. This software uses both CPUs of the TMS320F28379D controller described in Section 3.2.6. The first CPU (CPU1) is used for controlling the LED drivers and collecting ADC data using the two SPI ports of the controller. The second CPU (CPU2) controls one of the two UART ports. This port is used for sending the collected data to the computer. The two CPUs communicate with each other using the built-in IPC module of the controller.

There are two main processes in the C program. The first process initializes, configures and synchronizes the different parts of the system. In this process, CPU1 initializes and configures the SPI ports at first. Then, the ADC is initialized and configured by selecting the data rate, PGA amplification, and reference voltage. The LED driver output current value is also selected. After this, CPU1 waits until it receives an interrupt from CPU2 before continuing to the next step of the process. Meanwhile, in a parallel process, CPU2 initializes and configures the UART and waits until it receives a start command from the GUI. Upon receiving the start command it sets an interrupt flag to CPU1 and both CPUs can continue to the next step of the process. The first process is shown in a detailed flow chart (Fig. 19).

The second process is used to modulate the LED current, to collect ADC data and transfer this data to the PC. In the beginning of the process, CPU1 switches the LED current and enables the ADC to capture the data. After this, CPU1 waits in standby until the ADC has finished converting the data and sets a data ready (drdy) flag. Upon receiving the ADC drdy flag, CPU1 enters an interrupt service routine (ISR). In the ISR the converted data is read and is written to a message packet (Fig. 21). The message packet consists of conversion data from six ADC channels, a time stamp and LED status. The message is written to a shared memory buffer and an IPC flag is set to notify CPU2 a message is ready. Upon receiving this flag, CPU2 starts an ISR used for transferring preamble bits followed by the received message packet via UART to the GUI. The flow diagram of this process is shown in Fig. 20.

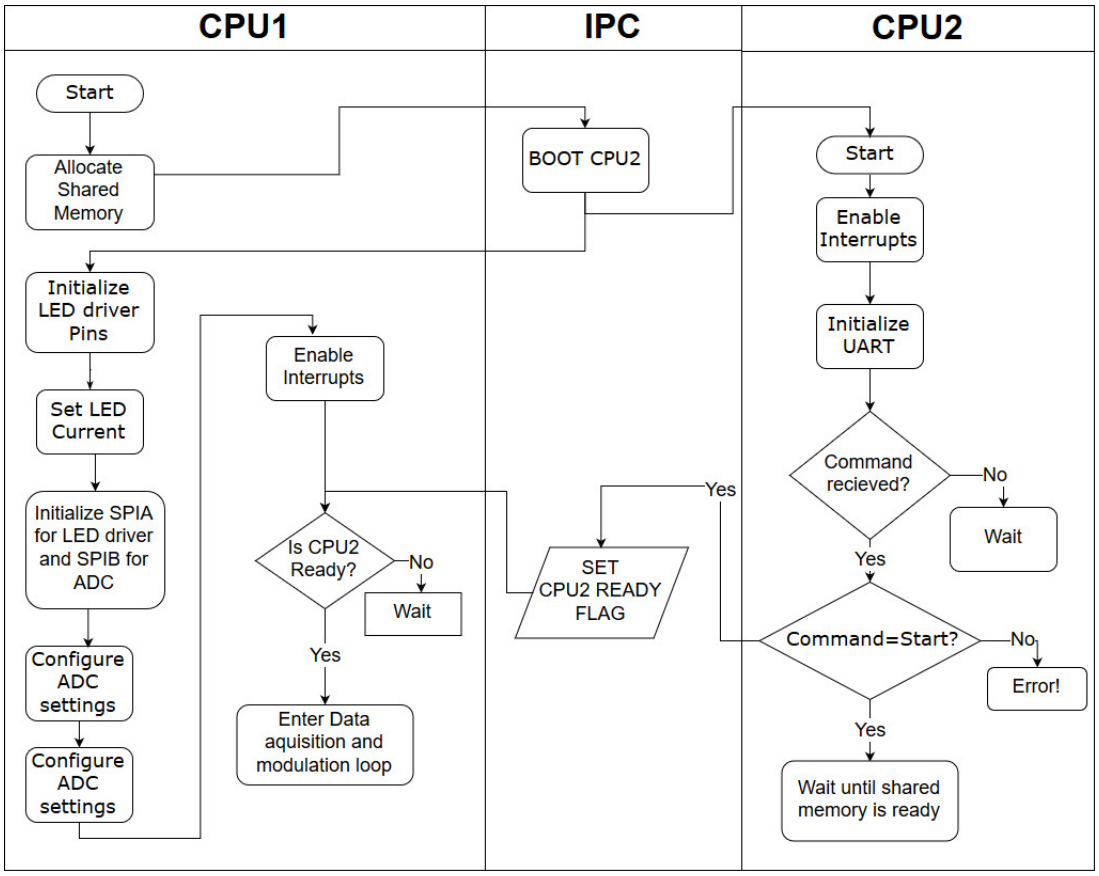

Figure 19: Initial software and synchronization sequence between CPU1, CPU2 and the user interface

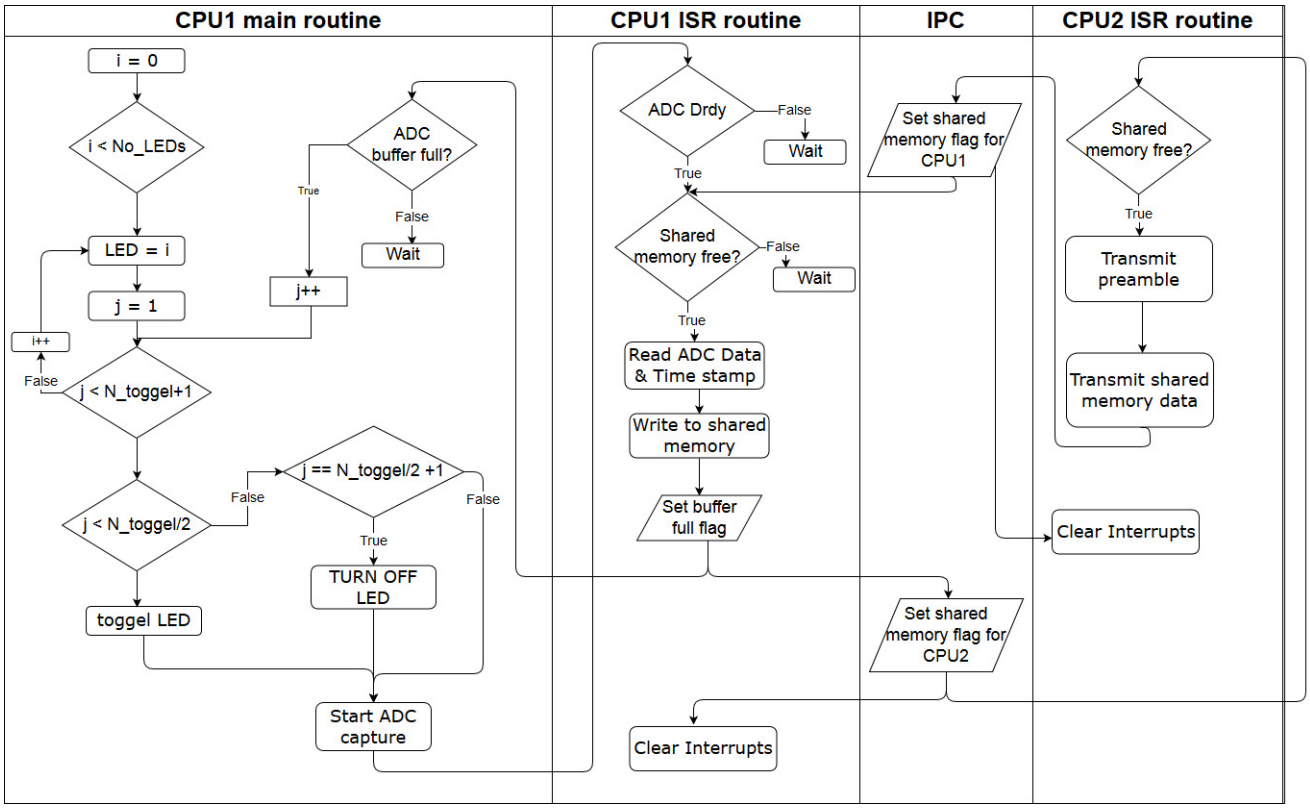

Figure 20: Second software sequence which modulates LED current, collects ADC conversion and transfers data to PC

The data packet sent via the UART to the computer consists of synchronizing bits, time stamp, LED status and ADC conversion results. Fig. 21 shows the structure of this packet.

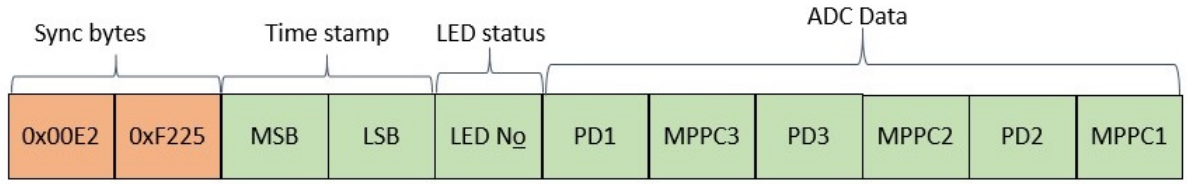

Figure 21: Structure of a data packet sent from the microcontroller to the computer via UART.

3.3.2 Graphical User Interface

A stand-alone graphical user interface (GUI) was implemented using LabView 2016 graphical programming tool. The GUI is used to log and visualize the raw data received from the DAQ-C unit via the UART bus. Additionally, the GUI receives an event status through a push button. This button is useful for distinguishing

between different experimental conditions during data analysis. Fig. 22 shows the front window of the GUI.

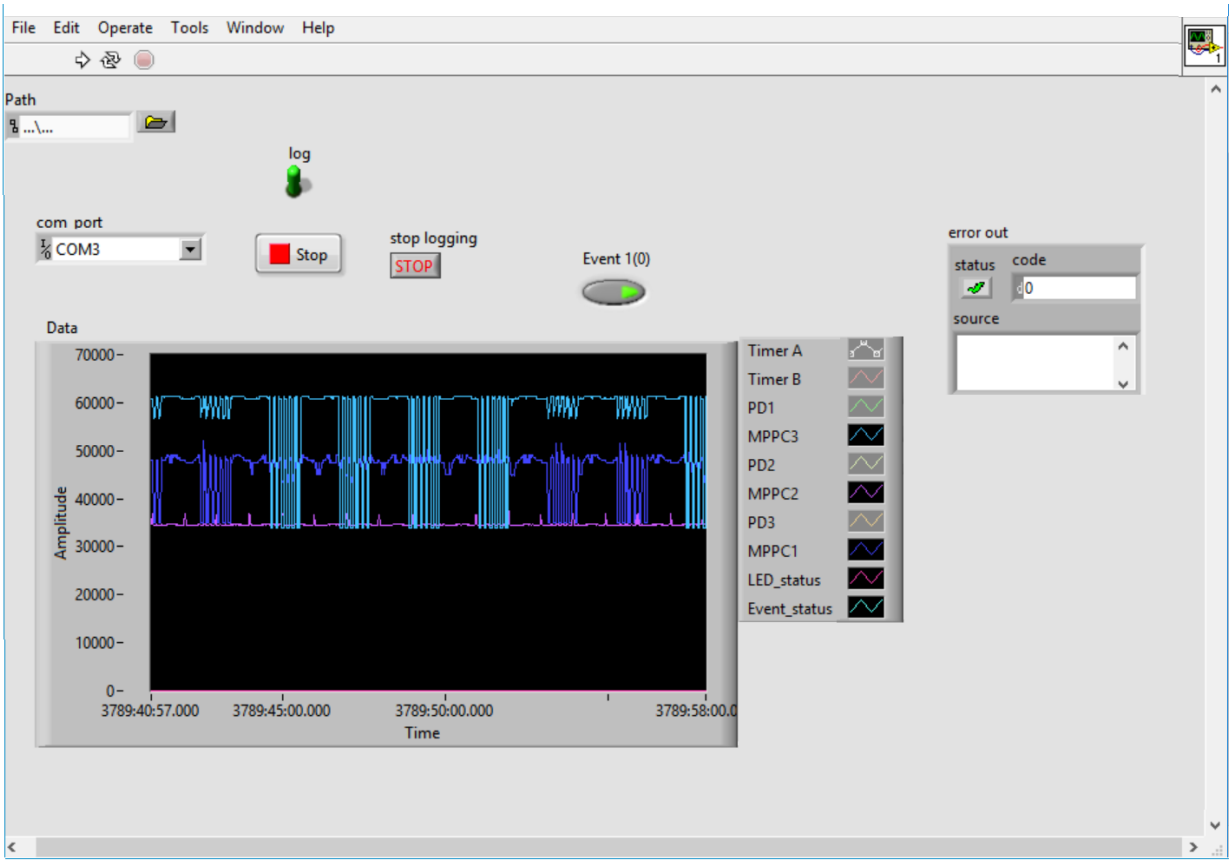

Figure 22: Graphical user interface.

The GUI was implemented using producer-consumer architecture. In this architecture, there are two parallel loops, the producer and the consumer, as the name suggests. This architecture is beneficial for processes that produce and consume data at different rates. The received data is queued between the two loops using an event handler.

In the current design, the incoming data is transferred at a high speed $> 10^6$ bits per second. However, the incoming data is saved at a much slower rate. Hence, the producer loop plots the data, appends the current event status and queues it for the consumer loop. The consumer loop then saves the conditioned data into a file at a slower rate. Fig. A18 shows the block diagram of the producer-consumer loop.

4 Test and Validation

This section discusses the test procedures and experiments conducted to validate the functionality of the developed DOT system. Sections 4.1 to 4.4 present various tests conducted to see functionality of the circuits. Section 4.5 discusses experiments conducted on a dynamic optical phantom for the validation of the prototype.

4.1 Power Supply

The impact of modulation on the output signal and on the on-board voltage regulators was evaluated using three one ohm resistors instead of the LEDs. The input current of the resistors from the LED current driver was modulated with a frequency of 1.2 kHz. During this experiment, the light detectors were not mounted, but the rest of the signal chain remained intact. Thus, enabling us to evaluate the impact of the current modulation on the overall output signal. This was achieved by quantifying the ADC output for all of the six input channels (Fig. 24 and 25). Additionally, the effect of modulation on analog supply voltage (V_{DD}) and the negative input reference voltage (V_{inN}) was measured using an oscilloscope Fig. 23.

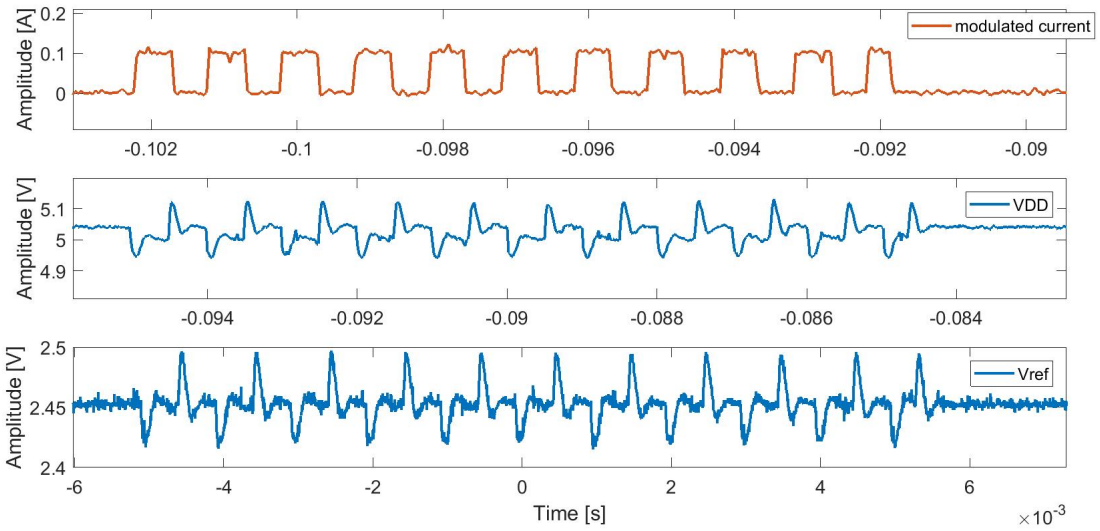

Figure 23: Modulated current, supply voltage and negative reference voltage of the TIA and the ADC.

Fig. 23 shows V_{DD} and V_{inN} measured using and osciloscope. The modulation affected $V_{DD} \sim 150$ mV and the VinN ~ 100 mV.

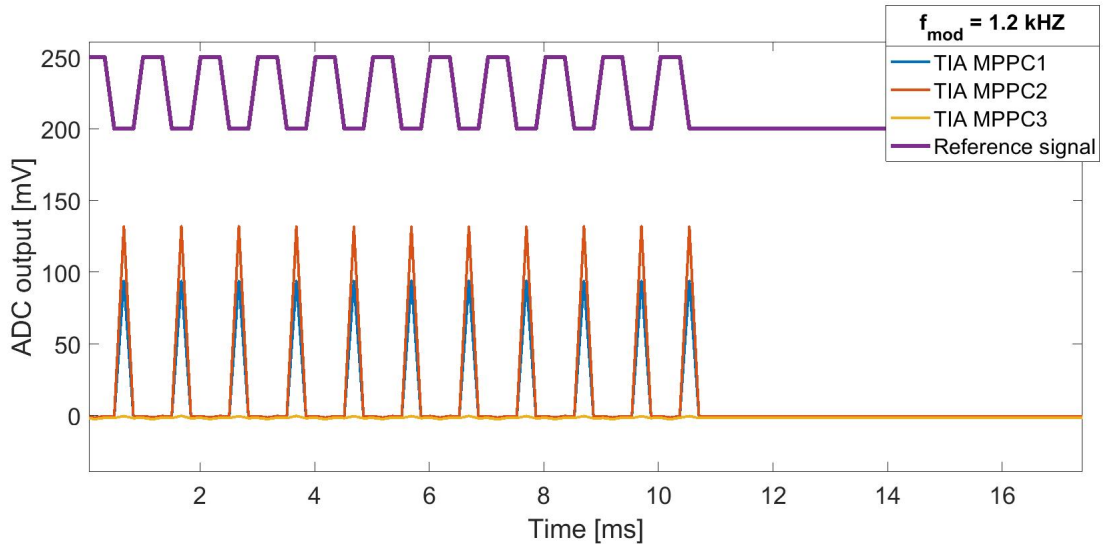

Figure 24: ADC outputs for MPPC TIA channels with respect to the reference modulating signal.

Fig. 24 shows the ADC output signal obtained during current modulation for the MPPC TIA channels where the gain was set to be 5 $k\Omega$. The overall noise that has resulted from current modulation in this channels is $\sim$ 120 mV.

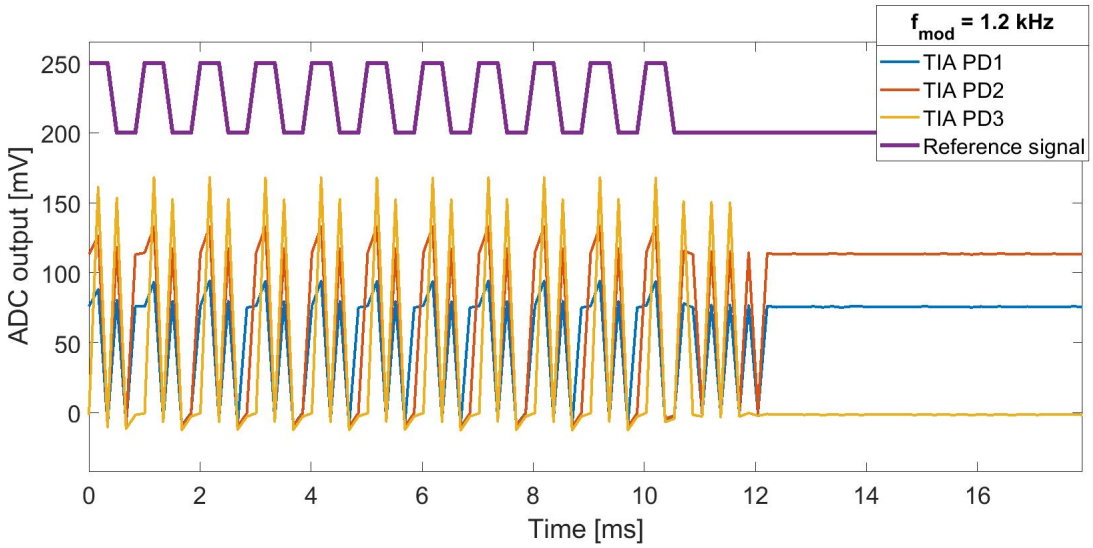

Figure 25: ADC outputs for PD TIA channels with respect to the reference modulating signal.

Fig. 25 shows the ADC output signal obtained during current modulation for the MPPC TIA channels where the gain was set to be 4.5 MΩ. The overall noise that has resulted from current modulation in these channels is $\sim$ 150mV.

In order to get sufficient signal quality the signal power from the detectors should be significantly higher than the noise limit posed by the current modulation ,i.e.

$\sim$ 150 mV. In future designs this noise limit can be improved by using separate supplies for the LED current modulating circuit and for the detection circuit.

4.2 LED Driver Output Current

The rise and fall time of the LED current at the driver output was examined by measuring the voltage across a 1 ohm resistor using an oscilloscope. The resistor was placed at the LED driver output and the output current was set at 100 mA. Fig. 26 shows the rise and fail time of the LED driver output current.

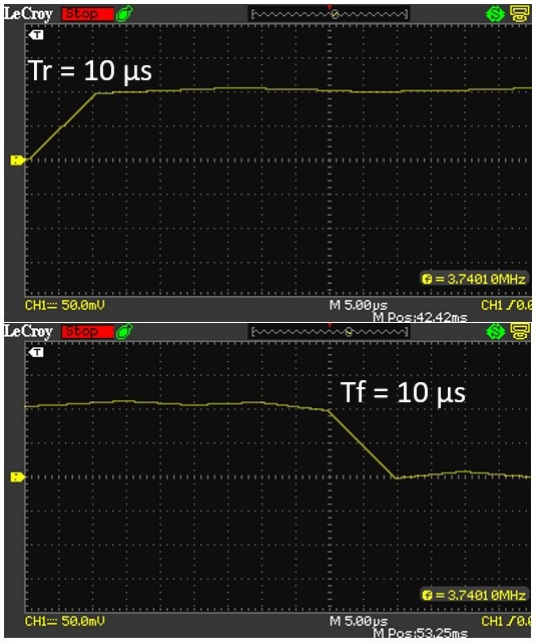

Figure 26: Rise and fail time of LED current driver output.

For lock-in detection, the LED current needs to be modulated at a few kHz. Thus, fast enough rise and fall times are necessary and this puts an upper limit to how large the modulation frequency can be. From the measurements, the rise and fall time (i.e, T_r and T_f) of the output LED current in this system was 10 μs. This is sufficiently fast for a few kHz modulation.

4.3 System Drift

To evaluate the overall drift of detectors, the probe was cast with a black silicon material (AccuTrans Black) and was covered with dark cloth. This helps to reduce interference from background light and maintain constant level of interference through out the experiment. The signal from the six detectors was acquired for $\sim$ 80 minutes with LED current of 50 mA, and modulation frequency of $\sim$ 1.2 kHz. The observed signal drift for the PDs was negligible. However, noticeable drift was observed in the MPPCs signal. The drift for the MPPC's is shown in Fig. 27.

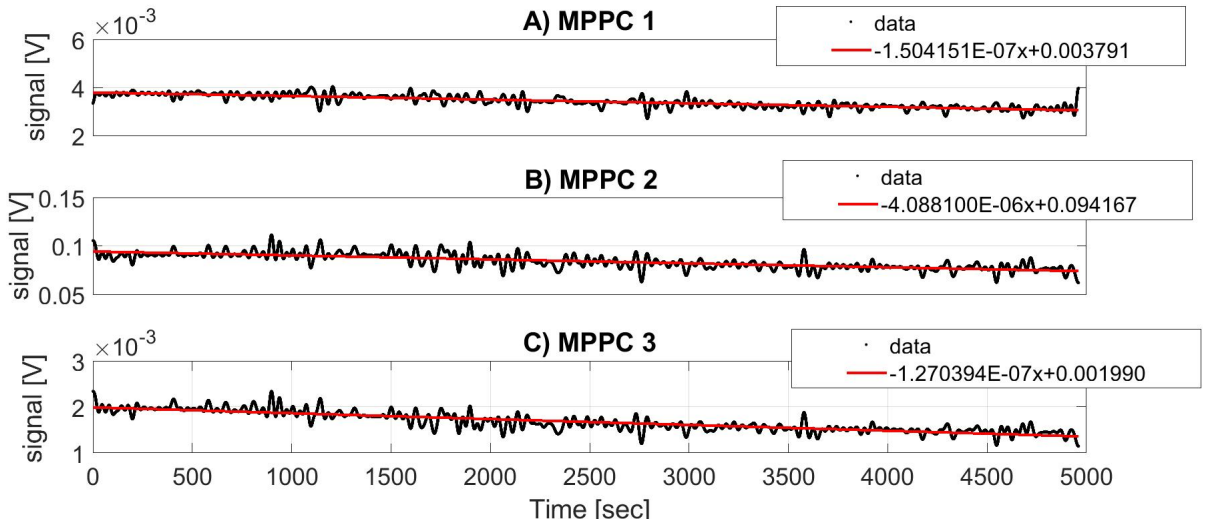

Figure 27: Observed signal drift on the three MPPC detectors

After fitting the demodulated MPPCs data using first degree polynomials, the system drift was estimated to be -0.15 uV/sec, -4 $\frac{\mu V}{sec}$ and -0.2 $\frac{\mu V}{sec}$ for the three MPPC channels. This significant signal drift is observed due to the high temperature dependence of the MPPC break down voltage. In this system, there has been an embedded temperature sensor that was intended to be used for the bias voltage compensation of the MPPCs. However, the sensor was found faulty during testing. Thus, all measurements had to be conducted without temperature compensation. In the future, having a working temperature compensation could reduce the drift significantly.

4.4 Impact of Lock-in Technique in Background Light Discrimination

The impact of the lock-in technique on signal quality and background light discrimination was demonstrated using four different sets of measurements. These measurements are: 1) using the lock-in method with $f_{mod} = 600$ Hz while background interference from a tungsten bulb is introduced 2) using the lock-in technique with $f_{mod} = 600$ Hz while no background light is introduced from a tungsten bulb 3) without using the lock-in method while background interference from a tungsten bulb is introduced 4) without using the lock-in method while no background light is introduced from a tungsten bulb. The results from these measurements are shown in Fig. 28 and 29.

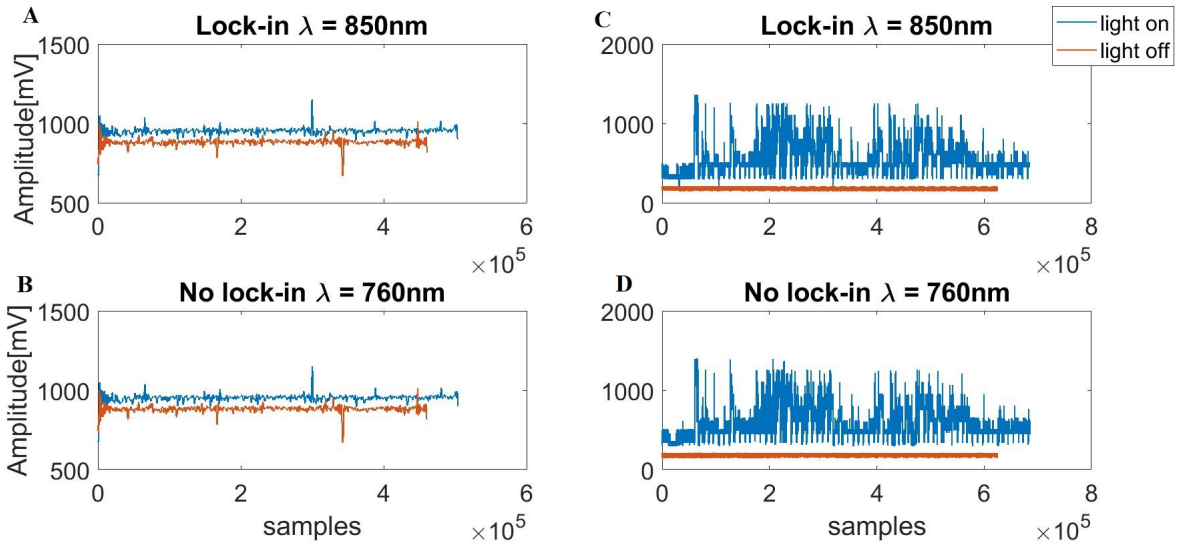

Figure 28: Raw signal for the case where lock-in was implemented at (A) $\lambda = 760$ and (B) λ =850 nm, raw signal for the case where no lock-in was implemented at (C) $\lambda = 760$ and (D) λ =850 nm.

Fig. 28 shows the raw signal for a single channel under the four conditions. As can be seen from the figure, when the tungsten bulb is on, the signal level increased both for the modulated and unmodulated light. Moreover for the signal where no lock-in technique was implemented there is a high level of noise arising from the flickering of the tungsten bulb at 100 Hz.

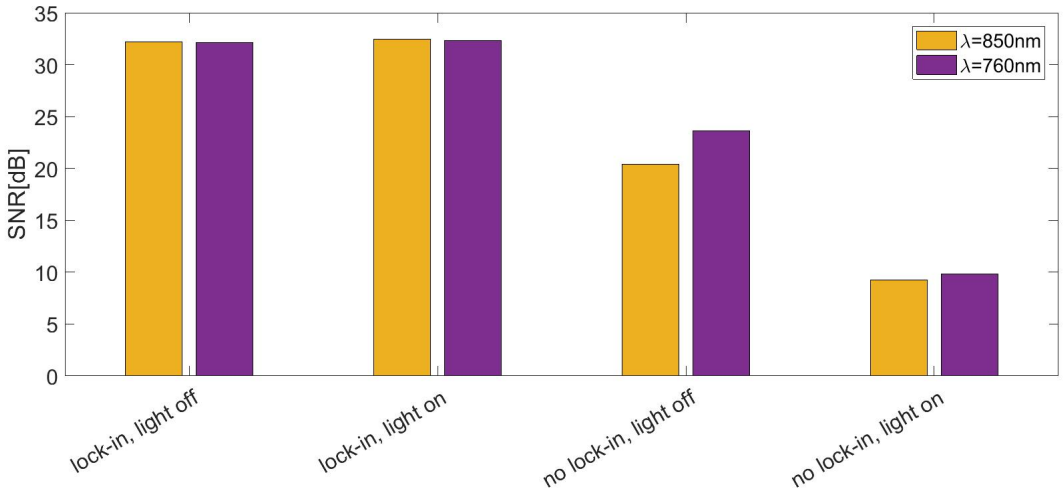

Figure 29: Signal-to-noise ratio case where lock-in was implemented and for the case where no lock-in was implemented at (C) $\lambda = 760$ and (D) λ =850 nm.

Fig. 29 shows the SNR calculated as $\frac{\text{mean(signal)}}{\text{std(signal)}}$. As can be seen from this figure, the SNR of the signal where lock-in technique is implemented remained the same (~ 32 dB) for both light-on and light-off conditions at both wavelengths. On the

other hand, in the unmodulated light measurements the SNR decreased significantly from $\sim$ 20 dB to $\sim$ 9 dB at $\lambda = 850$ nm and from $\sim$ 23 dB to $\sim$ 9.8 dB at $\lambda = 760$ nm. This shows that the lock-in technique can reduce the effect of background interference on the signal. However, it is important to note that in the measurements where no lock-in technique is used, no additional preprocessing steps such as subtracting the baseline, averaging or low pass filtering hasn't been performed which are common processing methods.

4.5 System verification using Dynamic Phantom

Finally, the designed system was tested using measurements on a dynamic optical phantom. This phantom consists of optical properties which are similar to human head and the optical properties can be adjusted dynamically by pushing a rod with an absorber in and out of the field of view (Fig. 30).

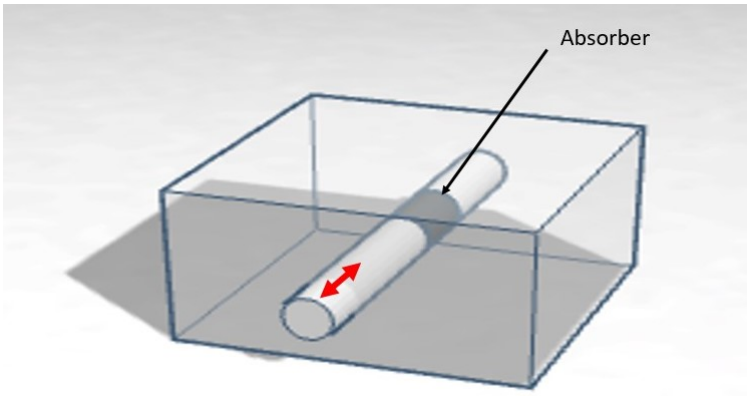

Figure 30: Dynamic optical phantom used for validating the designed DOT prototype.

Before the experiment was conducted the DOT sensor PCB was cast with Accu-Trans Black (by Coltene) in the side of the PCB that is placed on the scalp of the subjects. The casting prevents light leaks and provides softer contact surface.

During the experiment, the cast PCB was placed on top of the phantom and the absorber was pushed in and out of the field of view of MPPC2. The absorber was pushed in and out every 20 seconds and a total of sixteen signal repetitions were obtained. After that the signal was demodulated and averaged for yielding in the result shown in Fig. 31.

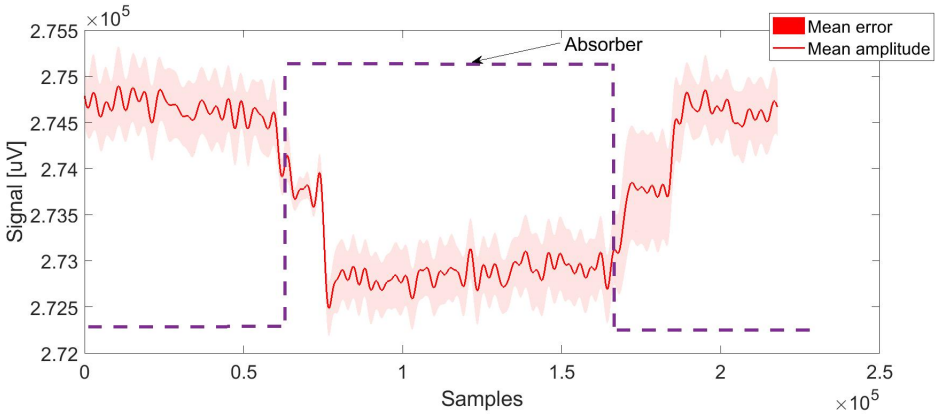

Figure 31: Signal obtained when an observer is pushed in and out of the FOV of an MPPC and a LED located 4.5 cm away.

A second experiment was conducted by placing the rod with the absorber in the field of view of a short distance PD placed 1 cm away from a LED as well as an MPPC detector located 4.5 cm away.The absorber was pushed in and out every 20 seconds and a total of fifteen signal repetitions were obtained. The signal was demodulated and averaged for yielding in the result shown in Fig. 32.

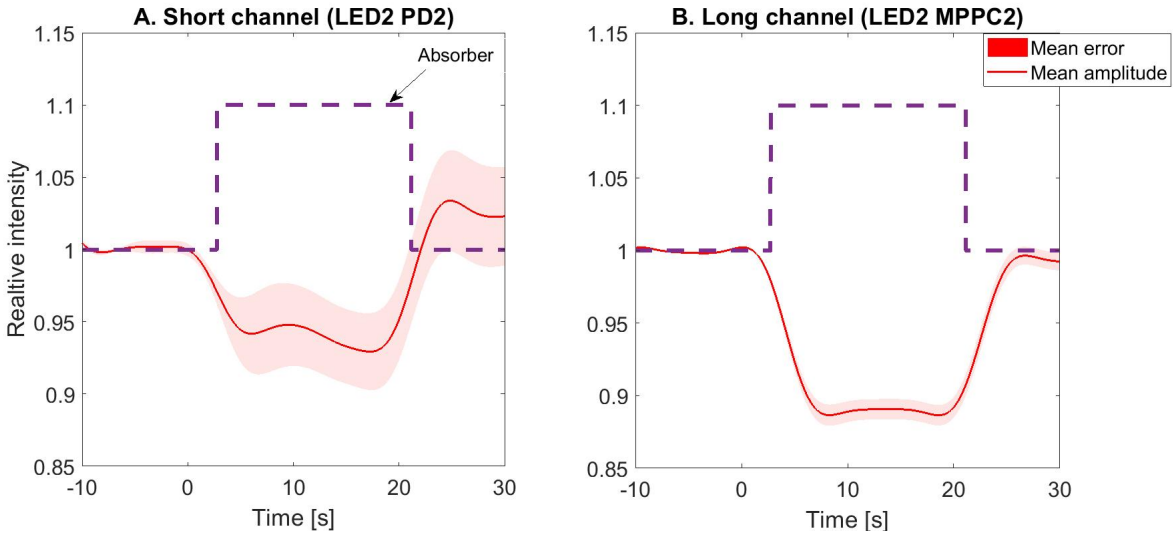

Figure 32: Signal obtained when an observer is pushed in and out of the FOV of (A) a PD located 1 cm away from the LED (B) an MPPC placed 4.5 cm away from a LED

5 Discussion and Conclusion

In this thesis, I have designed, developed and tested a fiberless multi-distance functional near-infrared spectroscopy instrument prototype. This prototype uses photodiodes at short source–detector separations and silicon photomultipliers at longer source–detector separations. The developed prototype consisted of two printed circuit boards (PCBs): a diffuse optical tomography (DOT) sensor PCB as well as a data acquisition and control (DAQ-C) PCB. Additionally, a graphical user interface was implemented for visualizing and storing data on a computer.

The microcontroller in the DAQ-C PCB was chosen by taking into consideration the ability to simultaneously control LED-driver and analog-to-digital converter(ADC) as well as to transfer the collected data at high speed to computer. The LED-driver chip was chosen because it can be used to time-multiplex and control the LED current accurately. While the ADC was chosen because it has low noise, high data rate and eight simultaneously sampling channels.

The current circuit can be improved by reducing the gain of the TIAs slightly both for the MPPCs and PDs to avoid saturation. Moreover, the drift in the MPPCs response can be reduced by using the temperature compensation nature of the SiPM high-voltage supply.

The DOT probe developed in this thesis is a rectangular 8 cm by 9.5 cm PCB which is very difficult to adapt to the curvature of the head. To improve this, future DOT probe designs can either be built using a flexible PCB or by building miniaturized modules. The flexible circuits can be applied by placing the source–detector optodes on a flexible PCB and connecting them to a control circuit with a cable. Alternatively, the system can also be built using a flexible-rigid PCBs and placing the control and data acquisition circuitry on the rigid part. On the other hand, miniaturized-modular design can be implemented by building for example, two types of modules consisting one short channel detector (PD) and one bi-color LED on source modules and MPPCs on detector modules. These modules then can then be inserted into pre-defined locations in a probe designed so that it can be worn like helmet.

Another issue to take into consideration during probe design is interference caused by hair. Hence, it is important that the source and detector optodes can easily be removed and plugged back after removing hair from under the sources and detectors.

Future designs could also use wireless and be battery operated, allowing for increased freedom of movement to subjects. For instance, wireless communication can be implemented using a bluetooth module. Additionally, if a high-density probe is designed a more powerful controller such as an field programmable graphic array (FPGA) should be used.

The designed system has done the preliminary work for a hybrid fiberless fNIRS and DOT system. This system could provide increased comfort for children neuroimaging studies with lower motion artefacts. This prototype can also be used for long-term bedside monitoring of infants with increased freedom of movement. Further more, photodiodes, unlike SiPMs, can be used to measure very short distances(2mm) without saturation in infant studies when superficial tissue regression is desired.

References

[1] Mohammadreza Abtahi, Gozde Cay, Manob Jyoti Saikia, and Kunal Mankodiya. Designing and testing a wearable, wireless fNIRS patch. In *2016 38th Annual International Conference of the IEEE Engineering in Medicine and Biology Society (EMBC)*, volume 2016, pages 6298–6301. IEEE, 2016.

[2] Diego Agro, Riccardo Canicatti, Maurizio Pinto, Giuseppe Morsellino, Alessandro Tomasino, Gabriele Adamo, Luciano Curcio, Antonino Parisi, Salvatore Stivala, Natale Galioto, Alessandro Busacca, and Costantino Giaconia. Design and implementation of a portable fNIRS embedded system. In Alessandro De Gloria, editor, *Lecture Notes in Electrical Engineering*, volume 351 of *Lecture Notes in Electrical Engineering*, pages 43–50. Springer International Publishing, Cham, 2014.

[3] Sangtae Ahn, Thien Nguyen, Hyojung Jang, Jae G. Kim, and Sung C. Jun. Exploring neuro-physiological correlates of crivers' mental fatigue caused by cleep ceprivation Using Simultaneous EEG, ECG, and fNIRS Data. *Frontiers in Human Neuroscience*, 10:1–14, 2016.

[4] Dincer Aktuerk, Pankaj Kumar Mishra, Heyman Luckraz, Andrew Garnham, and FayazMohammed Khazi. Cerebral oxygenation monitoring in patients with bilateral carotid stenosis undergoing urgent cardiac surgery: Observational case series. *Annals of Cardiac Anaesthesia*, 19(1):59–62, 2016.

[5] Fares Al-Shargie, Masashi Kiguchi, Nasreen Badruddin, Sarat C. Dass, Ahmad Fadzil Mohammad Hani, and Tong Boon Tang. Mental stress assessment using simultaneous measurement of EEG and fNIRS. *Biomedical Optics Express*, 7(10):3882, 2016.

[6] Elena A Allen. Transcranial magnetic stimulation elicits coupled neural and hemodynamic consequences. *Science*, 317(2007):1918–1922, 2014.

[7] A. R. Anwar, M. Muthalib, S. Perrey, A. Galka, O. Granert, S. Wolff, U. Heute, G. Deuschl, J. Raethjen, and Muthuraman Muthuraman. Effective connectivity of cortical sensorimotor networks during finger movement tasks: A simultaneous fNIRS, fMRI, EEG study. *Brain Topography*, 29(5):645–660, 2016.

[8] Dizem Arifler, Tingting Zhu, Sara Madaan, and Ilias Tachtsidis. Optimal wavelength combinations for near-infrared spectroscopic monitoring of changes in brain tissue hemoglobin and cytochrome c oxidase concentrations. *Biomedical Optics Express*, 6(3):933, 2015.

[9] Simon R. Arridge and John C. Schotland. Optical tomography: Forward and inverse problems. *Inverse problems*, 25(12), 2009.

[10] Joana B. Balardin, Guilherme A. Zimeo Morais, Rogério A. Furucho, Lucas Trambaiolli, Patricia Vanzella, Claudinei Biazoli, and João R. Sato. Imaging

brain function with functional near-Infrared spectroscopy in unconstrained environments. *Frontiers in Human Neuroscience*, 11, 2017.

[11] Michela Balconi, Elisabetta Grippa, and Maria Elide Vanutelli. What hemodynamic (fNIRS), electrophysiological (EEG) and autonomic integrated measures can tell us about emotional processing. *Brain and Cognition*, 95:67–76, 2015.

[12] Michela Balconi and Maria E. Vanutelli. Competition in the brain. The contribution of EEG and fNIRS modulation and personality effects in social ranking. *Frontiers in Psychology*, 7:1–14, 2016.

[13] Gemma Bale, Clare E. Elwell, and Ilias Tachtsidis. From Jöbsis to the present day: a review of clinical near-infrared spectroscopy measurements of cerebral cytochrome-c-oxidase. *Journal of biomedical optics*, 21(9):091307, 2016.

[14] David A. Benaron, John P. Van Houten, Wai-Fung Cheong, Eben L. Kermit, and Richard A. King. Early clinical results of time-of-flight optical tomography in a neonatal intensive care unit. In Britton Chance and Robert R. Alfano, editors, *proceedings of SPIE,Optical Tomography, Photon Migration, and Spectroscopy of Tissue and Model Media: Theory, Human Studies, and Instrumentation*, volume 2389, pages 582–596, 1995.

[15] M. Raheel Bhutta, Keum Shik Hong, Beop Min Kim, Melissa Jiyoun Hong, Yun Hee Kim, and Se Ho Lee. Three wavelengths near-infrared spectroscopy system for compensating the light absorbance by water. *Review of Scientific Instruments*, 85(2):2012–2015, 2014.

[16] Yvonne Blokland, Loukianos Spyrou, Dick Thijssen, Thijs Eijsvogels, Willy Colier, Marianne Floor-Westerdijk, Rutger Vlek, Jorgen Bruhn, and Jason Farquhar. Combined EEG-fNIRS decoding of motor attempt and imagery for brain switch control: An offline study in patients with tetraplegia. *IEEE Transactions on Neural Systems and Rehabilitation Engineering*, 22(2):222–229, 2014.

[17] D. A. Boas, K. Chen, D. Grebert, and M. A. Franceschini. Improving the diffuse optical imaging spatial resolution of the cerebral hemodynamic response to brain activation in humans. *Optics Letters*, 2004.

[18] Sabrina Brigadoi and Robert J. Cooper. How short is short? Optimum source–detector distance for short-separation channels in functional near-infrared spectroscopy. *Neurophotonics*, 2(2):025005, 2015.

[19] Britton Chance, Qingming Luo, Shoko Nioka, David C. Alsop, and John A. Detre. Optical investigations of physiology: a study of intrinsic and extrinsic biomedical contrast. *Philosophical transactions of the Royal Society of London. Series B, Biological sciences*, 352(1354):707–16, 1997.

[20] Antonio M. Chiarelli, Sebania Libertino, Filippo Zappasodi, Massimo Mazzillo, Francesco Di Pompeo, Arcangelo Merla, Salvatore Lombardo, and Giorgio Fallica. Characterization of a fiber-less, multichannel optical probe for continuous wave functional near-infrared spectroscopy based on silicon photomultipliers detectors: in-vivo assessment of primary sensorimotor response. *Neurophotonics*, 4(03):1, 2017.

[21] Danial Chitnis, Dimitrios Airantzis, David Highton, Rhys Williams, Phong Phan, Vasiliki Giagka, Samuel Powell, Robert J Cooper, Ilias Tachtsidis, Martin Smith, Clare E Elwell, Jeremy C Hebden, and Nicholas Everdell. Towards a wearable near infrared spectroscopic probe for monitoring concentrations of multiple chromophores in biological tissue in vivo. *Review of Scientific Instruments*, 87(6):065112, 2016.

[22] Jong Kwan Choi, Jae Myoung Kim, Gunpil Hwang, Jaehyeok Yang, Min Gyu Choi, and Hyeon Min Bae. Time-Divided Spread-Spectrum Code-Based 400 fW-Detectable Multichannel fNIRS IC for Portable Functional Brain Imaging. *IEEE Journal of Solid-State Circuits*, 51(2):484–495, 2016.

[23] Mark Cope and David T Delpy. System for long-term measurement of cerebral blood and tissue oxygenation on newborn infants by near infra-red transillumination. *Medical & Biological Engineering & Computing*, 26(3):289–294, 1988.

[24] Shirley Coyle, Tomás Ward, Charles Markham, and Gary McDarby. On the suitability of near-infrared (NIR) systems for next-generation brain-computer interfaces. *Physiological Measurement*, 25(4):815–822, 2004.

[25] Murphy D., De Kerillis P., Frabizzio J., and Nash B. Measurement of acute brain hemorrhage in the pre-hospital setting. *Stroke*, 2015.

[26] D T Delpy, M Cope, P van der Zee, S Arridge, S Wray, and J Wyatt. Estimation of optical pathlength through tissue from direct time of flight measurement. *Physics in Medicine and Biology*, 33(12):1433–1442, 1988.

[27] Adam T Eggebrecht, Silvina L Ferradal, Amy Robichaux-Viehoever, Mahlega S. Hassanpour, Hamid Dehghani, Abraham Z Snyder, Tamara Hershey, and Joseph P. Culver. Mapping distributed brain function and networks with diffuse optical tomography. *Nature Photonics*, 8(6):448–454, 2014.

[28] Gerhard Wilhelm Eschweiler, Christine Wegerer, Wilfried Schlotter, Christoph Spandl, Andreas Stevens, Mathias Bartels, and Gerhard Buchkremer. Left prefrontal activation predicts therapeutic effects of repetitive transcranial magnetic stimulation (rTMS) in major depression. *Psychiatry Research - Neuroimaging*, 99(3):161–172, 2000.

[29] N. L. Everdell, A. P. Gibson, I. D. C. Tullis, T. Vaithianathan, J. C. Hebden, and D. T. Delpy. A frequency multiplexed near-infrared topography system for

imaging functional activation in the brain. *Review of Scientific Instruments*, 76(9):093705, 2005.

[30] Parisa Farzam, E.M. Erin M. Buckley, Pei-Yi P.-Y. Lin, Katherine Hagan, P.E. Ellen Grant, T.E. Terrie Eleanor Inder, Stefan A. S.A. Carp, and M.A. Maria Angela Franceschini. Shedding light on the neonatal brain: Probing cerebral hemodynamics by diffuse optical spectroscopic methods. *Scientific Reports*, 2017.

[31] Siamac Fazli, Jan Mehnert, Jens Steinbrink, Gabriel Curio, Arno Villringer, Klaus Robert Müller, and Benjamin Blankertz. Enhanced performance by a hybrid NIRS-EEG brain computer interface. *NeuroImage*, 59(1):519–529, 2012.

[32] P T Fox, M E Raichle, and W T Thach. Functional mapping of the human cerebellum with positron emission tomography. *Proceedings of the National Academy of Sciences of the United States of America*, 82(21):7462–6, 1985.

[33] Tsukasa Funane, Takashi Numata, Hiroki Sato, Shinsuke Hiraizumi, Yuichi Hasegawa, Hidenobu Kuwabara, Kiyoshi Hasegawa, and Masashi Kiguchi. Rearrangeable and exchangeable optical module with system-on-chip for wearable functional near-infrared spectroscopy system. *Neurophotonics*, 5(01):1, 2017.

[34] Louis Gagnon, Robert J. Cooper, Meryem A. Yücel, Katherine L. Perdue, Douglas N. Greve, and David A. Boas. Short separation channel location impacts the performance of short channel regression in NIRS. *NeuroImage*, 59(3):2518–2528, 2012.

[35] Anne Gallagher, Maryse Lassonde, Danielle Bastien, Phetsamone Vannasing, Frédéric Lesage, Christophe Grova, Alain Bouthillier, Lionel Carmant, Franco Lepore, Renée Béland, and Dang Khoa Nguyen. Non-invasive pre-surgical investigation of a 10 year-old epileptic boy using simultaneous EEG-NIRS. *Seizure*, 17(6):576–582, 2008.

[36] Feng Gao, Huijuan Zhao, and Yukio Yamada. Improvement of Image Quality in Diffuse Optical Tomography by use of Full Time-Resolved Data. *Appl. Opt.*, 41(4):778–791, 2002.

[37] A Ghassemi, K Sato, and K Kobayashi. Technical note, MPPC.[Online] Hamatsu.com. Available at: https://www.hamamatsu.com/resources/pdf/ssd/mppc_kapd9005e.pdf[Accessed 20.Nov. 2018].

[38] Nicholas M. Gregg, Brian R. White, Benjamin W. Zeff, Andrew J. Berger, and P. Culver Joseph. Brain specificity of diffuse optical imaging: improvements from superficial signal regression and tomography. *Frontiers in Neuroenergetics*, 2(4):1–8, 2010.

[39] Stefan Jun Groiss, Hitoshi Mochizuki, Toshiaki Furubayashi, Shunsuke Kobayashi, Setsu Nakatani-Enomoto, Koichiro Nakamura, and Yoshikazu Ugawa. Quadri-pulse stimulation induces stimulation frequency dependent cortical hemoglobin concentration changes within the ipsilateral motor cortical network. *Brain Stimulation*, 6(1):40–48, 2013.

[40] Bertan Hallacoglu, Jason W Trobaugh, Kate L Bechtel, and Chandran V Seshagiri. Blood phantom verification of a new compact DOT system. *Biomedical Optics*, 2016.

[41] Hamamatsu Photonics. MPPCs for precision measurement, S13360 series datasheet, Aug. 2016.

[42] Jeremy C Hebden, Marta Varela, Salavat Magazov, Nick Everdell, Adam Gibson, and Topun Austin. Diffiuse optical imaging of the newborn infant brain. *Proc. of 9th IEEE In- ternational Symposium, Biomedical Imaging: from Nano to Macro*, pages 503–505, 2012.

[43] J. Heiskala, P. Hiltunen, and I. Nissilä. Significance of background optical properties, time-resolved information and optode arrangement in diffuse optical imaging of term neonates. *Physics in Medicine and Biology*, 54(3):535–554, 2009.

[44] Fabian Herold, Patrick Wiegel, Felix Scholkmann, and Notger Müller. Applications of Functional Near-Infrared Spectroscopy (fNIRS) Neuroimaging in Exercise-Cognition Science: A Systematic, Methodology-Focused Review. *Journal of Clinical Medicine*, 7(12):466, 2018.

[45] Keum-shik Hong and Amad Zafar. Existence of Initial Dip for BCI: An Illusion or Reality. *Frontiers in Neurorobotics*, 12(October):1–21, 2018.

[46] Yoko Hoshi and Mamoru Tamura. Detection of dynamic changes in cerebral oxygenation coupled to neuronal function during mental work in man. *Neuroscience Letters*, 150(1):5–8, 1993.

[47] Yoko Hoshi and Yukio Yamada. Overview of diffuse optical tomography and its clinical applications. *Journal of Biomedical Optics*, 21(9):091312, 2016.

[48] A. Janani and M. Sasikala. Investigation of different approaches for noise reduction in functional near-infrared spectroscopy signals for brain–computer interface applications. *Neural Computing and Applications*, 28(10):2889–2903, 2017.

[49] F F Jobsis. Noninvasive, infrared monitoring of cerebral and myocardial oxygen sufficiency and circulatory parameters. *Science (New York, N.Y.)*, 198(4323):1264–1267, 1977.

[50] Frans F. Jobsis-vanderVliet. Discovery of the near-infrared window into the body and the early development of near-infrared spectroscopy . *Journal of Biomedical Optics*, 4(4):392–396, 1999.

[51] Emma H. Jönsson, Kalle Kotilahti, Juha Heiskala, Helena Backlund Wasling, Håkan Olausson, Ilona Croy, Hanna Mustaniemi, Petri Hiltunen, Jetro J. Tuulari, Noora M. Scheinin, Linnea Karlsson, Hasse Karlsson, and Ilkka Nissilä. Affective and non-affective touch evoke differential brain responses in 2-month-old infants. *NeuroImage*, 169(November 2016):162–171, 2018.

[52] Danny K. Joseph, Theodore J. Huppert, Maria Angela Franceschini, and David A. Boas. Diffuse optical tomography system to image brain activation with improved spatial resolution and validation with functional magnetic resonance imaging. *Applied Optics*, 45(31):8142, 2006.

[53] Ehsan Kamrani, Frederic Lesage, and Mohamad Sawan. Low-noise, high-gain transimpedance amplifier integrated with SiAPD for low-intensity near-infrared light detection. *IEEE Sensors Journal*, 14(1):258–269, 2014.

[54] Ali Kassab, Jérôme Le Lan, Julie Tremblay, Phetsamone Vannasing, Mahya Dehbozorgi, Philippe Pouliot, Anne Gallagher, Frédéric Lesage, Mohamad Sawan, and Dang Khoa Nguyen. Multichannel wearable fNIRS-EEG system for long-term clinical monitoring. *Human Brain Mapping*, 39(1):7–23, 2018.

[55] Mariia Keitaanniemi. *Study of neurovascular coupling via simultaneous magnetoencephalography and high-density diffuse optical tomography.* Bachelor thesis, Aalto University, 2016.

[56] M. Kiguchi, H. Atsumori, I. Fukasaku, Y. Kumagai, T. Funane, A. Maki, Y. Kasai, and A. Ninomiya. Note: Wearable near-infrared spectroscopy imager for haired region. *Review of Scientific Instruments*, 83(5):3–6, 2012.

[57] Choong Ki Kim, Seungduk Lee, Dalkwon Koh, and Beop Min Kim. Development of wireless NIRS system with dynamic removal of motion artifacts. *Biomedical Engineering Letters*, 1(4):254–259, 2011.

[58] Laszlo Kocsis, Peter Herman, and Andras Eke. The modified Beer-Lambert law revisited. *Physics in medicine and biology*, 51(5):N91–8, 2006.

[59] Hideaki Koizumi, Yuichi Yamashita, Atsushi Maki, Tsuyoshi Yamamoto, Yoshitoshi Ito, H Itagaki, and R Kennan. Higher-Order Brain Function Analysis by Trans-Cranial Dynamic Near-Infrared Spectroscopy Imaging. *Journal of Biomedical Optics*, 4(4):403, 1999.

[60] Christina Kolyva, Arnab Ghosh, Ilias Tachtsidis, David Highton, Chris E. Cooper, Martin Smith, and Clare E. Elwell. Cytochrome c oxidase response to changes in cerebral oxygen delivery in the adult brain shows higher brain-specificity than haemoglobin. *NeuroImage*, 85 Pt 1:234–244, 2014.

[61] Kalle Kotilahti, Ilkka Nissilä, Tiina Näsi, Lauri Lipiäinen, Tommi Noponen, Pekka Meriläinen, Minna Huotilainen, and Vineta Fellman. Hemodynamic responses to speech and music in newborn infants. *Human Brain Mapping*, 31(4):595–603, 2010.

[62] F. Andrew Kozel, Fenghua Tian, Sameer Dhamne, Paul E. Croarkin, Shawn M. McClintock, Alan Elliott, Kimberly S. Mapes, Mustafa M. Husain, and Hanli Liu. Using simultaneous repetitive Transcranial Magnetic Stimulation/functional Near Infrared Spectroscopy (rTMS/fNIRS) to measure brain activation and connectivity. *NeuroImage*, 47(4):1177–1184, 2009.

[63] Takashi Kusaka, Kenichi Isobe, Saneyuki Yasuda, Kosuke Koyano, Shinji Nakamura, Makoto Nakamura, Masaki Ueno, Takanori Miki, and Susumu Itoh. Evaluation of cerebral circulation and oxygen metabolism in infants using near-infrared light. *Brain and Development*, 36(4):277–283, 2014.

[64] Chuen Wa Lee, Robert J. Cooper, and Topun Austin. Diffuse optical tomography to investigate the newborn brain. *Pediatric Research*, 82(3):376–386, 2017.

[65] Jose Leon-Carrion, Jose Maria Dominguez-Roldan, Umberto Leon-Dominguez, and Francisco Murillo-Cabezas. The Infrascanner, a handheld device for screening in situ for the presence of brain haematomas. *Brain Injury*, 2010.

[66] Sarah Lloyd-Fox, M. Papademetriou, M. K. Darboe, N. L. Everdell, R. Wegmuller, A. M. Prentice, S. E. Moore, and C. E. Elwell. Functional near infrared spectroscopy (fNIRS) to assess cognitive function in infants in rural Africa. *Scientific reports*, 4(4740):4740, 2014.

[67] Sarah Lloyd-Fox, Borbála Széplaki-Köllod, Jun Yin, and Gergely Csibra. Are you talking to me? Neural activations in 6-month-old infants in response to being addressed during natural interactions. *Cortex*, 70:35–48, 2015.

[68] Hiraoka M., Firbank M., Essenpreis M., Cope M., Arridge S R., van der Zee P., and Delpy D T. A Monte Carlo investigation of optical pathlength in inhomogeneous tissue and its application to near-infrared spectroscopy. *Physics in Medicine and Biology*, 38:1859–1876, 1993.

[69] A. Machado, J. M. Lina, J. Tremblay, M. Lassonde, D. K. Nguyen, F. Lesage, and C. Grova. Detection of hemodynamic responses to epileptic activity using simultaneous Electro-EncephaloGraphy (EEG)/Near Infra Red Spectroscopy (NIRS) acquisitions. *NeuroImage*, 56(1):114–125, 2011.

[70] Chemseddine Mansouri, Jean Pierre L'Huillier, Nasser H. Kashou, and Anne Humeau. Depth sensitivity analysis of functional near-infrared spectroscopy measurement using three-dimensional Monte Carlo modelling-based magnetic resonance imaging. *Lasers in Medical Science*, 2010.

[71] E. Martinenghi, L. Di Sieno, D. Contini, M. Sanzaro, A. Pifferi, and A. Dalla Mora. Time-resolved single-photon detection module based on silicon photomultiplier: A novel building block for time-correlated measurement systems. *Review of Scientific Instruments*, 87(7), 2016.

[72] G. A. Millikan. Experiments on Muscle Haemoglobin in vivo; The Instantaneous Measurement of Muscle Metabolism. *Proceedings of the Royal Society B: Biological Sciences*, 123(831):218–241, 1937.

[73] G. A. Millikan. The Oximeter, an Instrument for Measuring Continuously the Oxygen Saturation of Arterial Blood in Man. *Review of Scientific Instruments*, 13(10):434–444, 1942.

[74] Hitoshi Mochizuki, Toshiaki Furubayashi, Ritsuko Hanajima, Yasuo Terao, Yoko Mizuno, Shingo Okabe, and Yoshikazu Ugawa. Hemoglobin concentration changes in the contralateral hemisphere during and after theta burst stimulation of the human sensorimotor cortices. *Experimental Brain Research*, 180(4):667–675, 2007.

[75] Thomas Muehlemann, Daniel Haensse, and Martin Wolf. Wireless miniaturized in-vivo near infrared imaging. *Optics Express*, 16(14):10323, 2008.

[76] F Murillo-Cabezas, U Leon-Dominguez, J M Dominguez-Roldan, and J Leon-Carrion. Acute early detection of brain hematomas in patients with TBI using the Infrascanner. *Brain Injury*, 2010.

[77] Dang Khoa Nguyen, Julie Tremblay, Philippe Pouliot, Phetsamone Vannasing, Olivia Florea, Lionel Carmant, Franco Lepore, Mohamad Sawan, Frédéric Lesage, and Maryse Lassonde. Non-invasive continuous EEG-fNIRS recording of temporal lobe seizures. *Epilepsy Research*, 99(1-2):112–126, 2012.

[78] Ilkka Nissilä, Tommi Noponen, Kalle Kotilahti, Toivo Katila, Lauri Lipiäinen, Tanja Tarvainen, Martin Schweiger, and Simon Arridge. Instrumentation and calibration methods for the multichannel measurement of phase and amplitude in optical tomography. *Review of Scientific Instruments*, 76(4), 2005.

[79] Eiji Okada and David T. Delpy. Near-infrared light propagation in an adult head model I Modeling of low-level scattering in the cerebrospinal fluid layer. *Applied Optics*, 42(16):2906, 2003.

[80] Luis Orozco. Use Synchronous Detection to Make Precision, Low Level Measurments (MS-2698). *Analog Devices Technical Articles*, pages 1–8, 2014.

[81] OSRAM Opto Semiconductors . Silicon PIN Photodiode with very short switching time, datasheet, Feb. 2001 [Revised Dec. 2015].

[82] Roberto Pagano, Sebania Libertino, Delfo Sanfilippo, Giorgio Fallica, and Salvatore Lombardo. Improvement of sensitivity in continuous wave near

infrared spectroscopy systems by using silicon photomultipliers. *Biomedical Optics Express*, 7(4):1183, 2016.

[83] Ke Peng, Dang Khoa Nguyen, Tania Tayah, Phetsamone Vannasing, Julie Tremblay, Mohamad Sawan, Maryse Lassonde, Frédéric Lesage, and Philippe Pouliot. FNIRS-EEG study of focal interictal epileptiform discharges. *Epilepsy Research*, 108(3):491–505, 2014.

[84] Joost Peters, Bas Van Wageningen, Nico Hoogerwerf, and Edward Tan. Near-Infrared Spectroscopy: A Promising Prehospital Tool for Management of Traumatic Brain Injury. *Prehospital and Disaster Medicine*, 2017.

[85] Paola Pinti, Clarisse Aichelburg, Frida Lind, Sarah Power, Elizabeth Swingler, Arcangelo Merla, Antonia Hamilton, Sam Gilbert, Paul Burgess, and Ilias Tachtsidis. Using Fiberless, Wearable fNIRS to Monitor Brain Activity in Real-world Cognitive Tasks. *Journal of visualized experiments : JoVE*, 106, 2015.

[86] Sophie K Piper, Arne Krueger, Stefan P Koch, Jan Mehnert, Christina Habermehl, Jens Steinbrink, Hellmuth Obrig, and Christoph H Schmitz. A wearable multi-channel fNIRS system for brain imaging in freely moving subjects. *NeuroImage*, 85(0 1):64–71, 2014.

[87] Philippe Pouliot, Julie Tremblay, Manon Robert, Phetsamone Vannasing, Franco Lepore, Maryse Lassonde, Mohamad Sawan, Dang Khoa Nguyen, and Frédéric Lesage. Nonlinear hemodynamic responses in human epilepsy: A multimodal analysis with fNIRS-EEG and fMRI-EEG. *Journal of Neuroscience Methods*, 204(2):326–340, 2012.

[88] Md. Asadur Rahman and Mohiuddin Ahmad. Identifying appropriate feature to distinguish between resting and active condition from FNIRS. In *2016 3rd International Conference on Signal Processing and Integrated Networks (SPIN)*, pages 671–675. IEEE, 2016.

[89] Nadège Roche-labarbe, S.A. Stefan a Carp, Andrea Surova, Megha Patel, D.A. Boas, P.E. Ellen Grant, Maria Angela M.A. Franceschini, A David, P.E. Ellen Grant, and Maria Angela M.A. Franceschini. Noninvasive optical measures of CBV, StO_2, CBF index, and $rCMRO_2$ in human premature neonates' brains in the first six weeks of life. *Human Brain Mapping*, 31(3):341–352, 2010.

[90] Mohammed Rupawala, Hamid Dehghani, Samuel J. E. Lucas, Peter Tino, and Damian Cruse. Shining a Light on Awareness: A Review of Functional Near-Infrared Spectroscopy for Prolonged Disorders of Consciousness. *Frontiers in Neurology*, 9:1–17, 2018.

[91] Rolf B Saager and Andrew J Berger. Measurement of layer-like hemodynamic trends in scalp and cortex: implications for physiological baseline suppression in functional near-infrared spectroscopy. *Journal of Biomedical Optics*, 13(3):034017, 2008.

[92] J. Safaie, R. Grebe, H Abrishami Moghaddam, and F. Wallois. Toward a fully integrated wireless wearable EEG-NIRS bimodal acquisition system. *Journal of neural engineering*, 10(5):056001, 2013.

[93] Manob Jyoti Saikia, Walt Besio, and Kunal Mankodiya. WearLight: Towards a Wearable, Configurable Functional NIR Spectroscopy System for Noninvasive Neuroimaging. *IEEE Transactions on Biomedical Circuits and Systems*, 13(1):91–102, 2018.

[94] T. H. Sander, A. Liebert, B. M. Mackert, H. Wabnitz, S. Leistner, G. Curio, M. Burghoff, R. Macdonald, and L. Trahms. DC-magnetoencephalography and time-resolved near-infrared spectroscopy combined to study neuronal and vascular brain responses. *Physiological Measurement*, 28(6):651–664, 2007.

[95] Hiroki Sato, Masashi Kiguchi, and Atsushi Maki. Wavelength dependence of effective pathlength factor in noninvasive optical measurements of human brain functions. *Japanese Journal of Applied Physics, Part 2: Letters*, 45(12-16), 2006.

[96] Mohamad Sawan, Muhammad T. Salam, Jerome Le Lan, Amal Kassab, Sebastien Gelinas, Phetsamone Vannasing, Frederic Lesage, Maryse Lassonde, and Dang K. Nguyen. Wireless recording systems: From noninvasive EEG-NIRS to invasive EEG devices. *IEEE Transactions on Biomedical Circuits and Systems*, 7(2):186–195, 2013.

[97] Florian E.W. Schmidt, Martin E. Fry, Elizabeth M.C. Hillman, Jeremy C. Hebden, and David T. Delpy. A 32-channel time-resolved instrument for medical optical tomography. *Review of Scientific Instruments*, 71(1):256–265, 2000.

[98] Christoph H. Schmitz, Mario Löcker, Joseph M. Lasker, Andreas H. Hielscher, and Randall L. Barbour. Instrumentation for fast functional optical tomography. *Review of Scientific Instruments*, 73(2):429–439, 2002.

[99] Felix Scholkmann, Stefan Kleiser, Andreas Jaakko Metz, Raphael Zimmermann, Juan Mata Pavia, Ursula Wolf, and Martin Wolf. A review on continuous wave functional near-infrared spectroscopy and imaging instrumentation and methodology. *NeuroImage*, 85(Part 1):6–27, 2014.

[100] Yusuke Seki, Tsuyoshi Miyashita, Akihiko Kandori, Atsushi Maki, and Hideaki Koizumi. Simultaneous measurement of neuronal activity and cortical hemodynamics by unshielded magnetoencephalography and near-infrared spectroscopy. *Journal of Biomedical Optics*, 17(10):1070011, 2012.

[101] Zh B. Semenova, A. V. Marshintsev, A. V. Melnikov, S. V. Meshcheryakov, A. R. Adayev, and V. I. Lukyanov. Infrascanner^{TM} in the diagnosis of intracranial lesions in children with traumatic brain injuries. *Brain Injury*, 2016.

[102] A. Siegel, J. J. Marota, and David Boas. Design and evaluation of a continuous-wave diffuse optical tomography system. *Optics Express*, 4(8):287, 1999.

[103] Gary Strangman, Maria Angela Franceschini, and David A Boas. Factors affecting the accuracy of near-infrared spectroscopy concentration calculations for focal changes in oxygenation parameters. *NeuroImage*, 18(4):865–879, 2003.

[104] Gary E Strangman, Zhi Li, and Quan Zhang. Depth Sensitivity and Source-Detector Separations for Near Infrared Spectroscopy Based on the Colin27 Brain Template. *PLOS ONE*, 8(8):e66319, 2013.

[105] Gentaro Taga, Fumitaka Homae, and Hama Watanabe. Effects of source-detector distance of near infrared spectroscopy on the measurement of the cortical hemodynamic response in infants. *NeuroImage*, 38(3):452–460, 2007.

[106] Texas Instruments. ADS131E0x4-, 6-, and 8-channel,24-Bit,simultaneously-sampling,delta-sigma ADC, datasheet, Jun.2012 [Revised Jan.2017].

[107] Texas Instruments. LAUNCHXL-F28379D overview, user's guide, Aug. 2016 [Revised Mar. 2019].

[108] Texas Instruments and Device Information. TLC591x 8-channel constant-current LED sink drivers, datasheet, Jun. 2007 [Revised Jan. 2015].

[109] Richard H. Thomson, Zafiris J. Daskalakis, and Paul B. Fitzgerald. A near infra-red spectroscopy study of the effects of pre-frontal single and paired pulse transcranial magnetic stimulation. *Clinical Neurophysiology*, 122(2):378–382, 2011.

[110] Kâmil Uludağ, Jens Steinbrink, Arno Villringer, and Hellmuth Obrig. Separability and cross talk: optimizing dual wavelength combinations for near-infrared spectroscopy of the adult head. *NeuroImage*, 22(2):583–589, 2004.

[111] Susumu Urakawa, Kouichi Takamoto, Akihiro Ishikawa, Taketoshi Ono, and Hisao Nishijo. Selective Medial Prefrontal Cortex Responses During Live Mutual Gaze Interactions in Human Infants: An fNIRS Study. *Brain Topography*, 28(5):691–701, 2015.

[112] Kyle Verdecchia, Mamadou Diop, Ting-Yim Lee, and Keith St. Lawrence. Quantifying the cerebral metabolic rate of oxygen by combining diffuse correlation spectroscopy and time-resolved near-infrared spectroscopy. *Journal of Biomedical Optics*, 18(2):027007, 2013.

[113] A Villringer and B Chance. Non-invasive optical spectroscopy and imaging of human brain function. *Trends in Neurosciences*, 20(10):435–442, 1997.

[114] A Villringer and U Dirnagl. Coupling of brain activity and cerebral blood flow: basis of functional neuroimaging. *Cerebrovasc Brain Metab Rev*, 1995.

[115] H. A. Vohra, A. Modi, and S. K. Ohri. Does use of intra-operative cerebral regional oxygen saturation monitoring during cardiac surgery lead to improved clinical outcomes? *Interactive CardioVascular and Thoracic Surgery*, 9(2):318–322, 2009.

[116] Alexander von Lühmann. *Design and Evaluation of a System for Mobile Brain Activity Measurements using Functional Near-Infrared Spectroscopy.* M.sc., Karlsruhe Institute of Technology, 2014.

[117] Alexander Von Luhmann, Heidrun Wabnitz, Tilmann Sander, and Klaus Robert Muller. M3BA: A Mobile, Modular, Multimodal Biosignal Acquisition Architecture for Miniaturized EEG-NIRS-Based Hybrid BCI and Monitoring. *IEEE Transactions on Biomedical Engineering*, 64(6):1199–1210, 2017.

[118] J. A. Wahr, K. K. Tremper, S. Samra, and D. T. Delpy. Near-infrared spectroscopy: Theory and applications. *Journal of Cardiothoracic and Vascular Anesthesia*, 10(3):406–418, 1996.

[119] F. Wallois, A. Patil, C. Héberlé, and R. Grebe. EEG-SPIR chez les patients épileptiques. *Neurophysiologie Clinique*, 40(5-6):281–292, 2010.

[120] Brian White. *Developing High-Density Diffuse Optical Tomography for Neuroimaging.* PhD thesis, Washington University in St. Louis, 2012.

[121] Dominik Wyser, Olivier Lambercy, Felix Scholkmann, Martin Wolf, and Roger Gassert. Wearable and modular functional near-infrared spectroscopy instrument with multidistance measurements at four wavelengths. *Neurophotonics*, 4(04):1, 2017.

[122] Mingdi Xu, Eiichi Hoshino, Kiyomi Yatabe, Soichiro Matsuda, Hiroki Sato, Atsushi Maki, Mina Yoshimura, and Yasuyo Minagawa. Prefrontal Function Engaging in External-Focused Attention in 5- to 6-Month-Old Infants: A Suggestion for Default Mode Network. *Frontiers in Human Neuroscience*, 10(January):1–9, 2017.

[123] M Atif Yaqub, Amad Zafar, Usman Ghafoor, and Keum-shik Hong. Development of a High Density Neuroimaging System Using Functional Near-Infrared Spectroscopy. In *2018 18th International Conference on Control, Automation and Systems (ICCAS)*, number Iccas, pages 1158–1163. Institute of Control, Robotics and Systems - ICROS, 2018.

[124] G Yurtsever, A Bozkurt, F Kepics, K Pourrezaei, A Devaraj, and A Bozkurt. Pocket PC based Wireless Continuous Wave Near Infrared Spectroscopy System for Functional Imaging of Human Brain. In *Annual International Conference of the IEEE Engineering in Medicine and Biology - Proceedings*, pages 53–54, 2003.

[125] Gunay Yurtsever, Hasan Ayaz, Frank Kepics, and Banu Onaral. Wireless, Continuous Wave Near Infrared Spectroscopy System for Monitoring Brain Activity, 2006.

[126] Benjamin W Zeff, Brian R White, Hamid Dehghani, Bradley L Schlaggar, and Joseph P Culver. Retinotopic mapping of adult human visual cortex with high-density diffuse optical tomography. *Proceedings of the National Academy of Sciences of the United States of America*, 104(29):12169–12174, 2007.

[127] Mahlet Zewde. Evaluation of silicon photomultipliers to build a high- density diffuse optical tomography instrument ., 2018.

[128] Yu Zhang, Xiong Zhang, Han Sun, Xuefei Zhong, and Zhaowen Fan. A Wearable Wireless fNIRS System. In *Proceedings of the 2018 8th International Conference on Bioscience, Biochemistry and Bioinformatics - ICBBB 2018*, number 2, pages 124–128, New York, New York, USA, 2018. ACM Press.

[129] Hubin Zhao and Robert J. Cooper. Review of recent progress toward a fiberless, whole-scalp diffuse optical tomography system. *Neurophotonics*, 5(01):1, 2017.

[130] R. Zimmermann, F. Braun, T. Achtnich, Olivier Lambercy, Roger Gassert, and M. Wolf. Silicon photomultipliers for improved detection of low light levels in miniature near-infrared spectroscopy instruments. *Biomedical optics express*, 4(5):659, 2013.

A Appendices

A.1 LED Driver behaviour

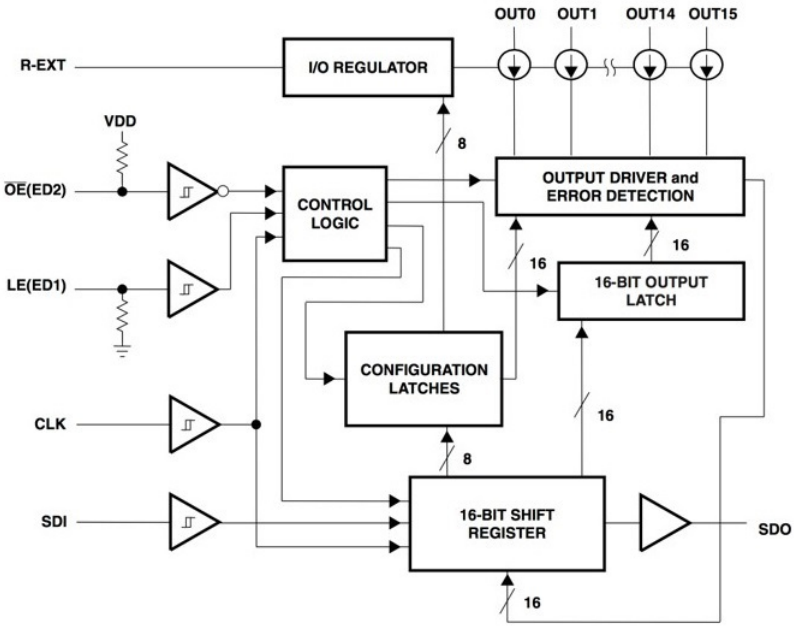

Figure A1: TLC5916- LED driver block diagram adapted from [108]

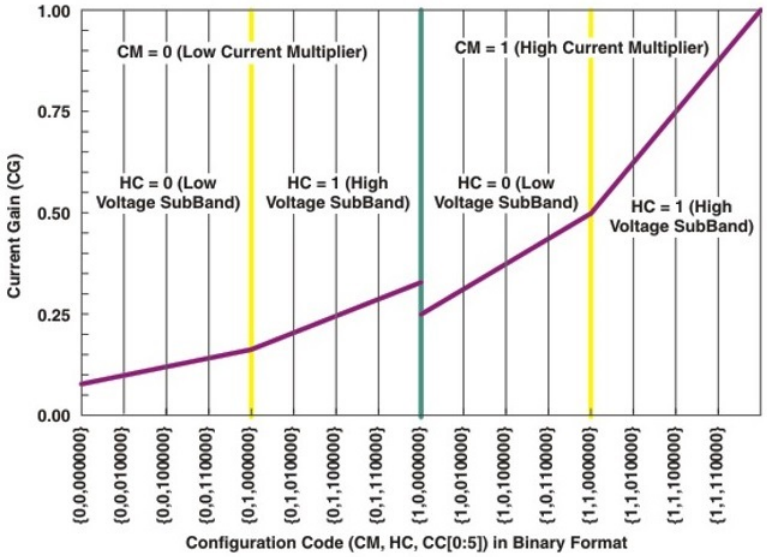

Figure A2: TLC5916- LED driver code vs output current [108]

A.2 SFH 229 Behaviour

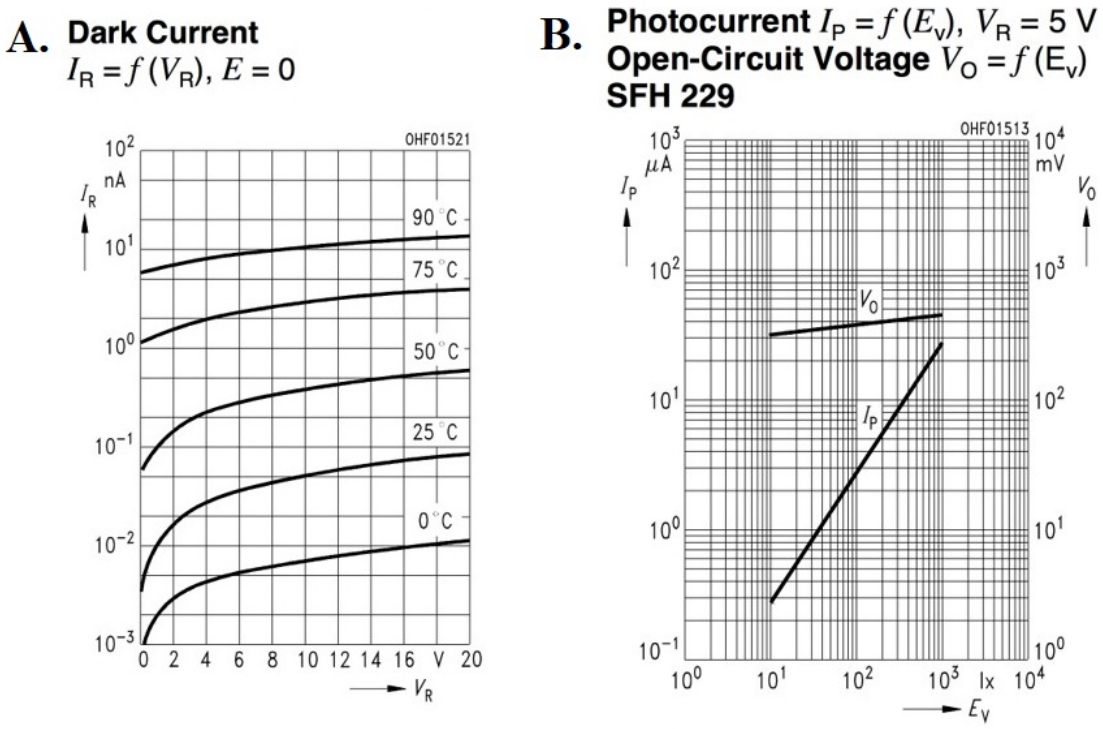

Figure A3: SFH229 photodiode dark current vs temperature adapted from [81]

A.3 MPPC Behaviour

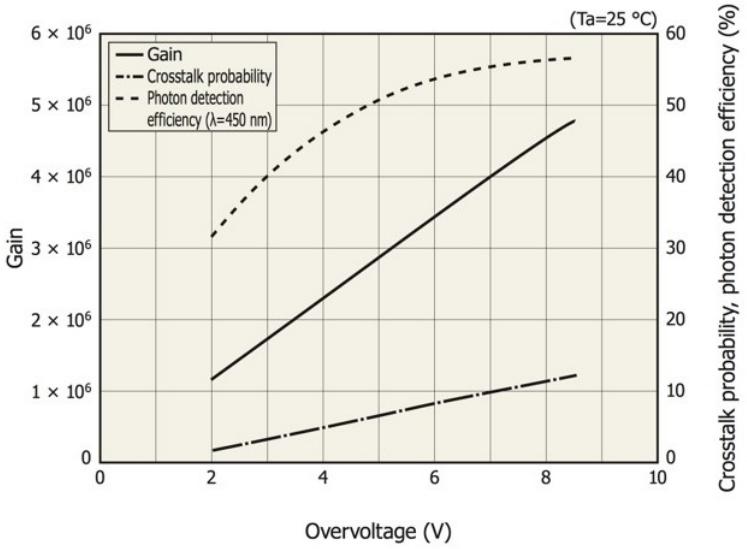

Figure A4: S13360-6050Cs- over voltage vs gain Adapted from [37]

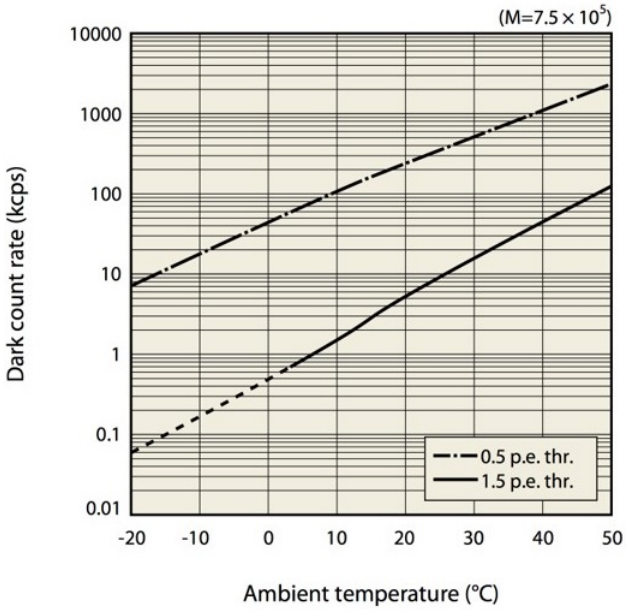

Figure A5: MPPC darkcrrent vs temp Adapted from [37]

A.4 ADS131E08 Behaviour

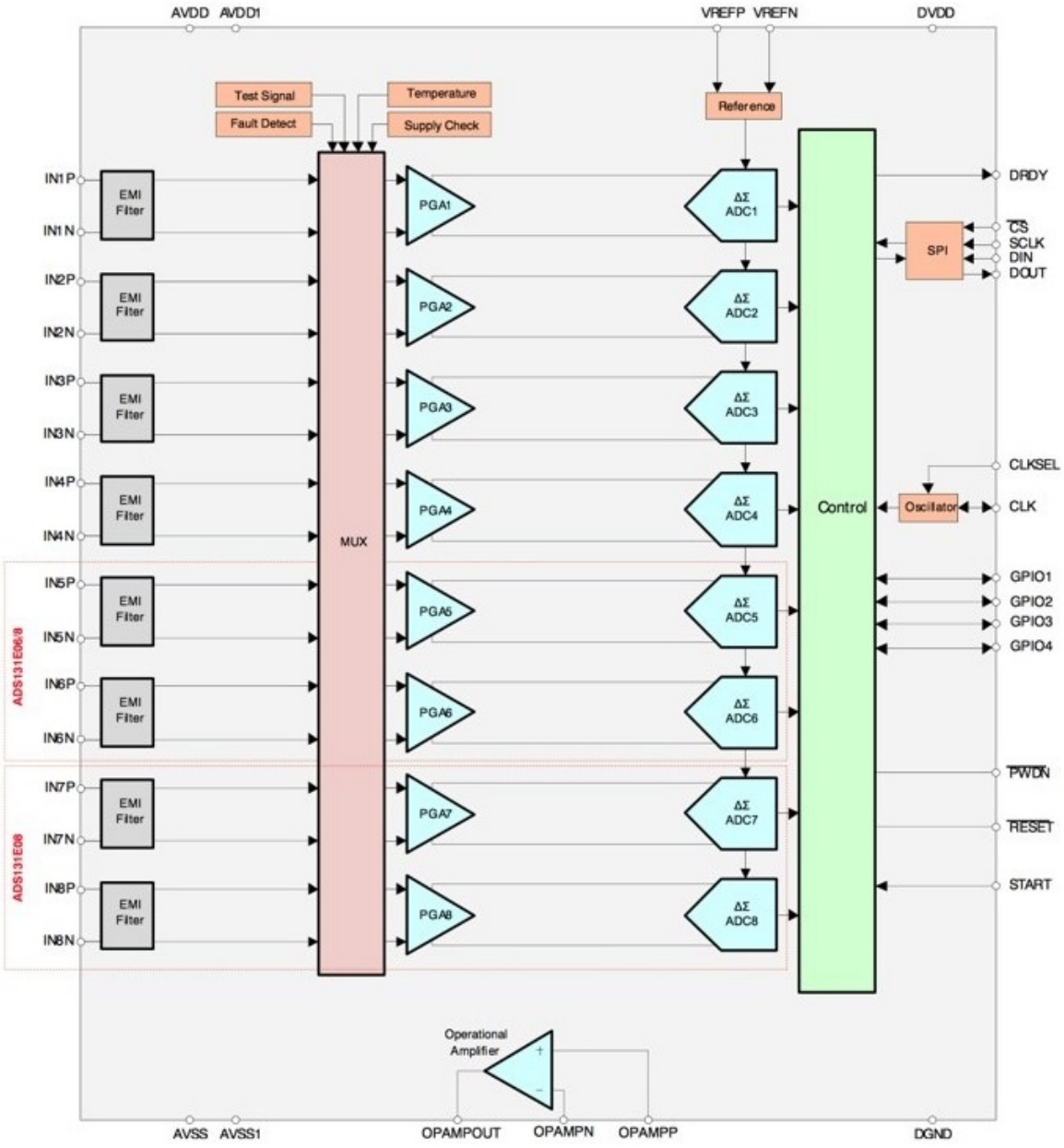

Figure A6: ADS131E08 block diagram adapted from [106]

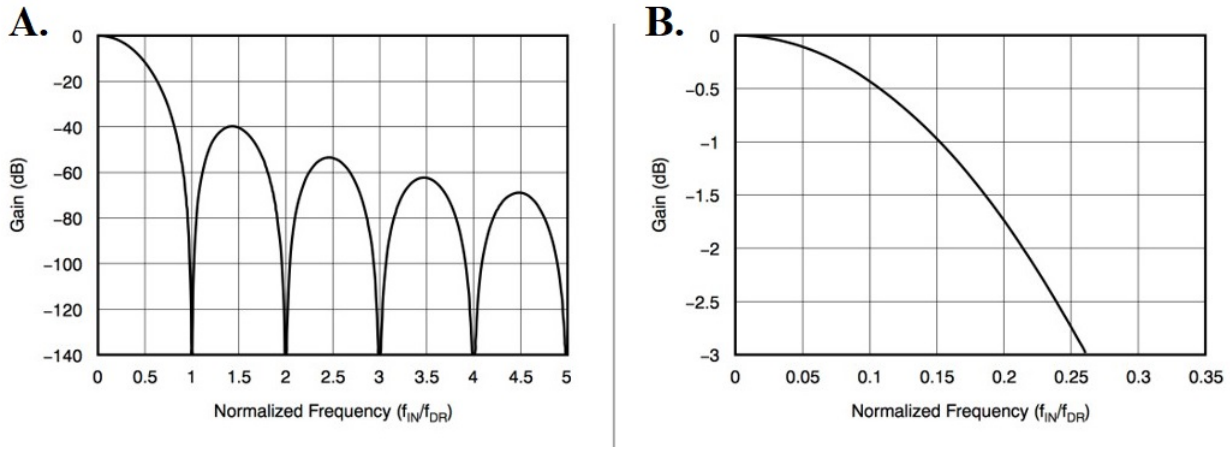

Figure A7: ADS131E08 Sinc filter frequency responce adapted from [106]

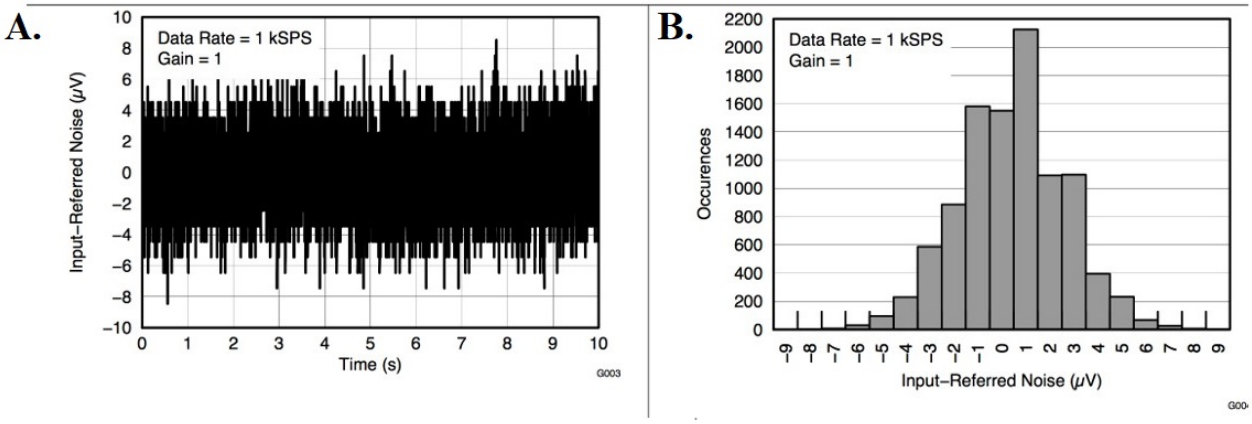

Figure A8: ADS131E08 PGA Noise and noise hystogram [106]

DR BITS (CONFIG1 Register)	OUTPUT DATA RATE (kSPS)	−3-dB BANDWIDTH (Hz)	PGA GAIN									
			x1		x2		x4		x8		x12	
			DYNAMIC RANGE (dB)	ENOB	DYNAMIC RANGE (dB)	ENOB	DYNAMIC RANGE (dB)	ENOB	DYNAMIC RANGE (dB)	ENOB	DYNAMIC RANGE (dB)	ENOB
000	64	16768	74.1	12.31	74.1	12.30	74.0	12.29	74.0	12.29	73.9	12.27
001	32	8384	89.6	14.89	89.6	14.88	89.4	14.85	88.6	14.71	87.6	14.55
010	16	4192	102.8	17.07	102.3	16.99	100.6	16.72	97.1	16.12	94.2	15.65
011	8	2096	108.2	18.0	107.4	17.9	105.2	17.5	101.6	16.9	98.9	16.5
100	4	1048	111.4	18.6	109.4	18.4	107.4	18.1	103.5	17.4	100.5	17.0
101	2	524	114.6	19.1	113.7	19.0	111.4	18.6	107.7	18.0	104.9	17.5
110	1	262	117.7	19.6	116.8	19.5	114.5	19.1	110.7	18.5	108.0	18.0

Figure A9: ADS131E08 PGA Noise vs gain Adapted from [106]

A.5 Hardware Design

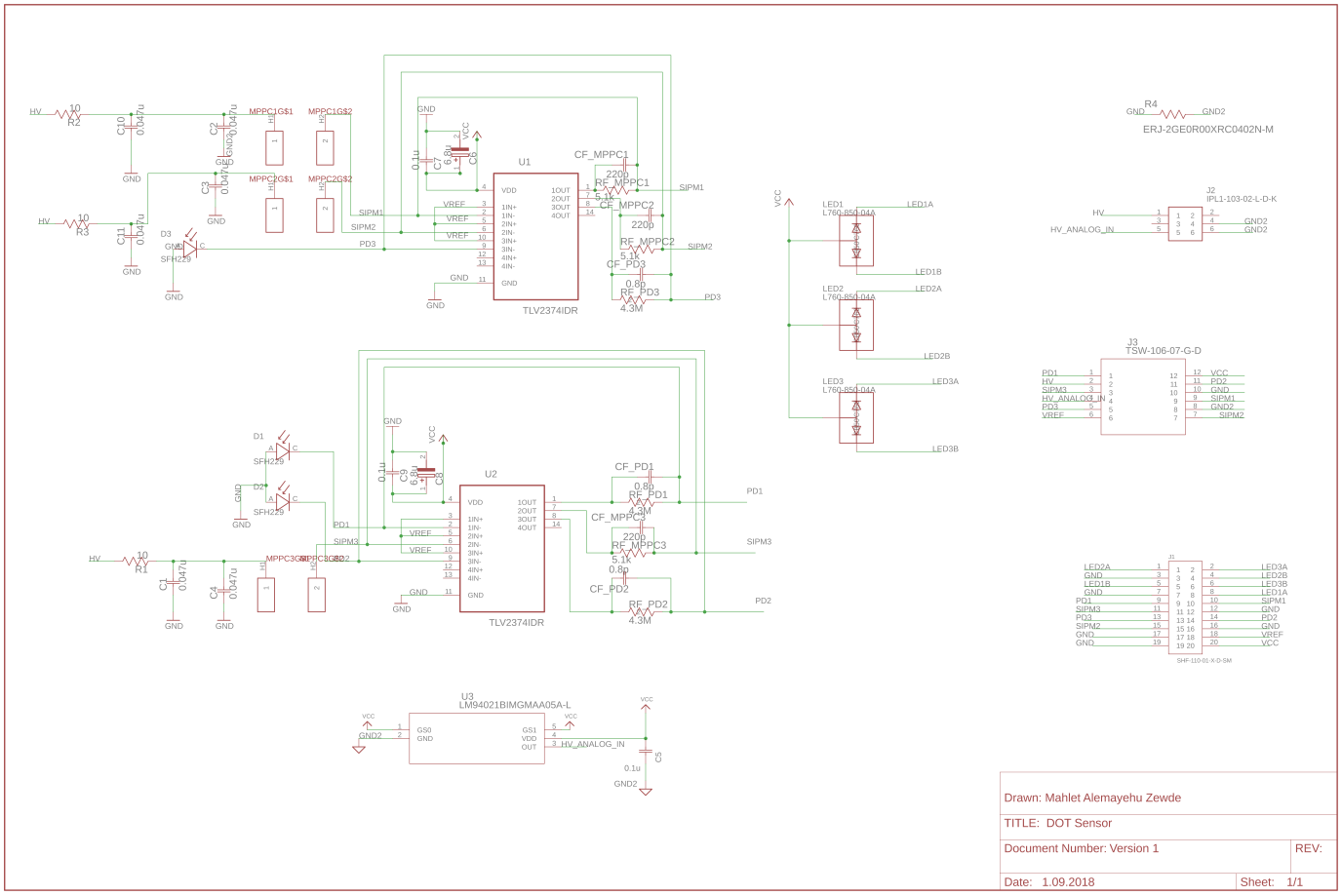

Figure A10: DOT Sensor PCB Schematic

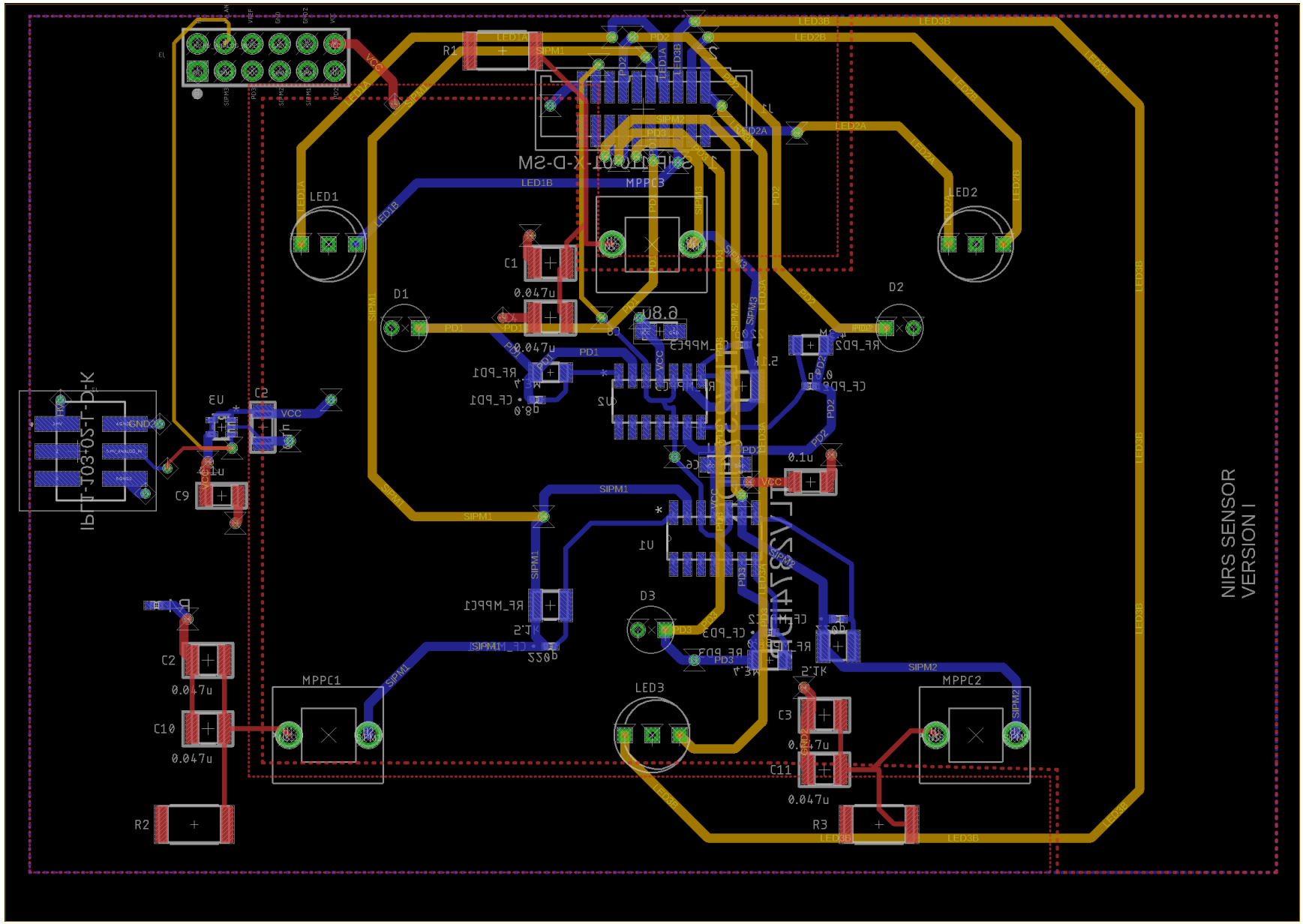

Figure A11: DOT Sensor PCB Layout

Table A1: DOT Sensor PCB Bill of Materials

Reference designators	Qty	Part number	Manufacturer	Description
RF_PD1, RF_PD2, RF_PD3	3	ERJ-8GEYJ435V	Panasonic	4.3 MOhms ±5% 0.25W, 1/4W Chip Resistor 1206 (3216 Metric) Automotive AEC-Q200 Thick Film
RF_MPPC1, RF_MPPC2, RF_MPPC3	3	CRCW12105K10FKEAHP	Vishay	5.1 kOhms ±1% 0.75W, 3/4W Chip Resistor 1210 (3225 Metric) Pulse Withstanding Thick Film
CF_PD1, CF_PD2, CF_PD3	3	GJM1555C1HR80BB01D	Murata	0.8pF ±0.1pF 50V Ceramic Capacitor C0G, NP0 0402 (1005 Metric)
CF_MPPC1, CF_MPPC2, CF_MPPC3	3	GCM1555C1H221JA16D	Murata	220pF ±5% 50V Ceramic Capacitor C0G, NP0 0402 (1005 Metric)
C1, C2, C3, C4, C10, C11	6	C1210C473JAGAC7800	Kemet	0.047µF ±5% 250V Ceramic Capacitor C0G, NP0 1210 (3225 Metric)
C5, C7, C9	3	CL31C104JAHNNWE	Samsung	0.1µF ±5% 25V Ceramic Capacitor C0G, NP0 1206 (3216 Metric)
C6, C8	2	T495A685K006ATE1K8	Kemet	6.8µF Molded Tantalum Capacitors 6.3V 1206 (3216 Metric) 1.8 Ohm
R1, R2, R3	3	RC2512JK-0710RL	Yageo	10 Ohm ±5% 1W Chip Resistor 2512 (6432 Metric) Moisture Resistant Thick Film
MPPC1, MPPC2, MPPC3, MPPC1_1, MPPC2_1, MPPC3_1	6	4015-0-43-80-30-27-10-0	Mill-max	Circuit Board Hardware - PCB 30P PIN RECEPTACLE W/OFP SOLDER BARRIER
LED1, LED2, LED3	3	L760/850-04A	Marubeni	Bi-color LED 760nm, 850nm
U3	1	LM94021BIMG/NOPB	Texas Instruments	Temperature Sensor Analog, Local -50°C ~ 150°C 5.5 ~ 13.6mV/°C SC-70-5
D1, D2, D3	3	SFH 229	OSRAM	PHOTODIODE 860NM 3MM CLEAR
J1	1	SHF-110-01-L-D-SM	Samtec Inc.	Connector Header Surface Mount 20 position 0.050" (1.27mm)

Table A2: DOT Sensor PCB Bill of Materials (continued)

Reference designators	Qty	Part number	Manufacturer	Description
J2	1	IPL1-103-02-L-D-K	Samtec	Connector Header Surface Mount 6 position 0.100" (2.54mm)
U1, U2	2	TLV2374IDR	Texas Instruments	General Purpose Amplifier 4 Circuit Rail-to-Rail 14-SOIC
R4	1	GPR04020R	Generic part	0 Ohms Jumper 0.1W, 1/10W Chip Resistor 0402 (1005 Metric) Automotive AEC-Q200 Thick Film
J3	1	TSW-106-07-G-D	Samtec	Connector Header Through Hole 12 position 0.100" (2.54mm)
SIPM1, SIPM2, SIPM3	3	S13360-6050CS	Hamamatsu	MPPC for precision measurement, Photo sensitive area: 6.0 x6.0 mm, pixel pitch 50 µm

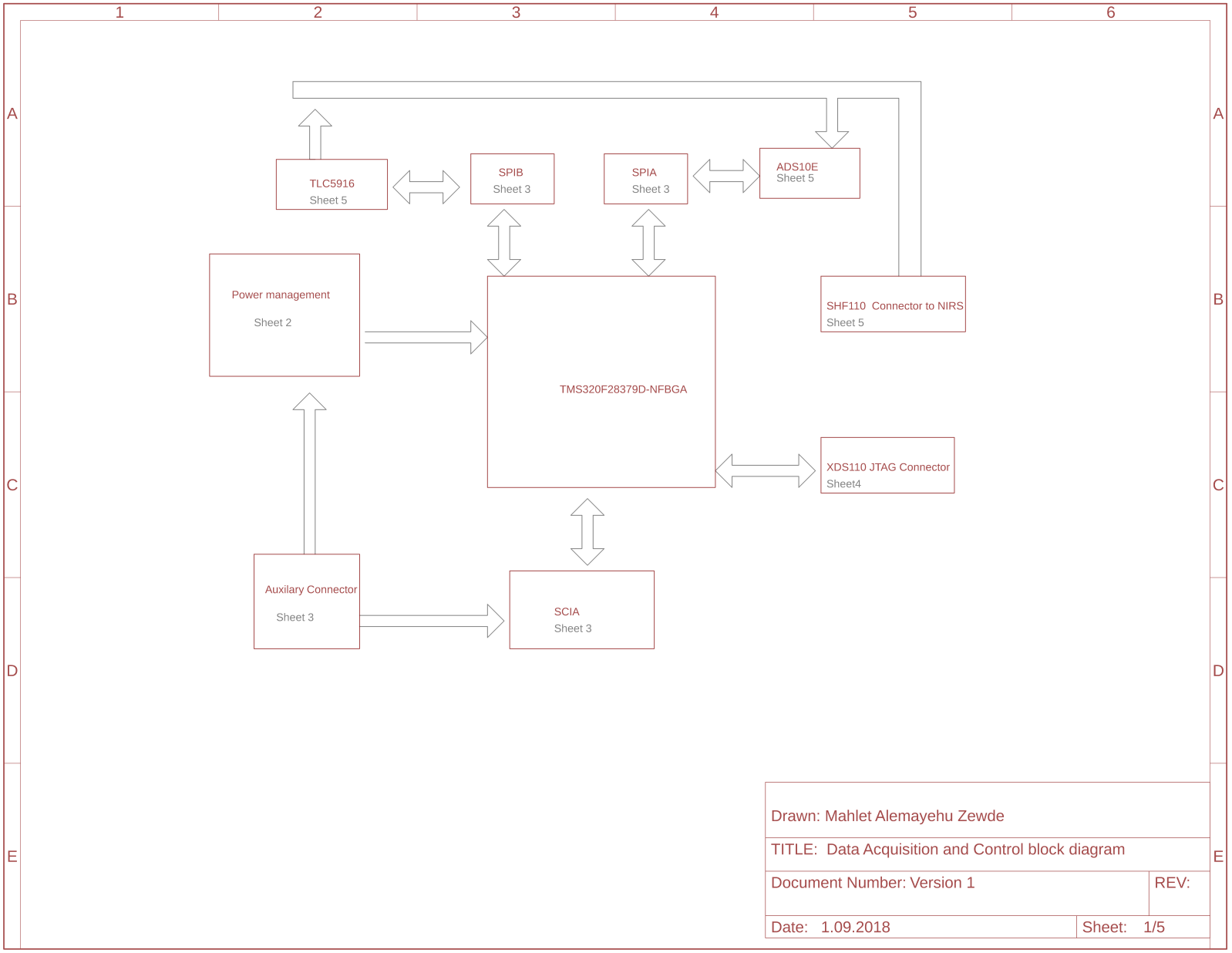

Figure A12: DAQ-C PCB Block Diagram Schematic

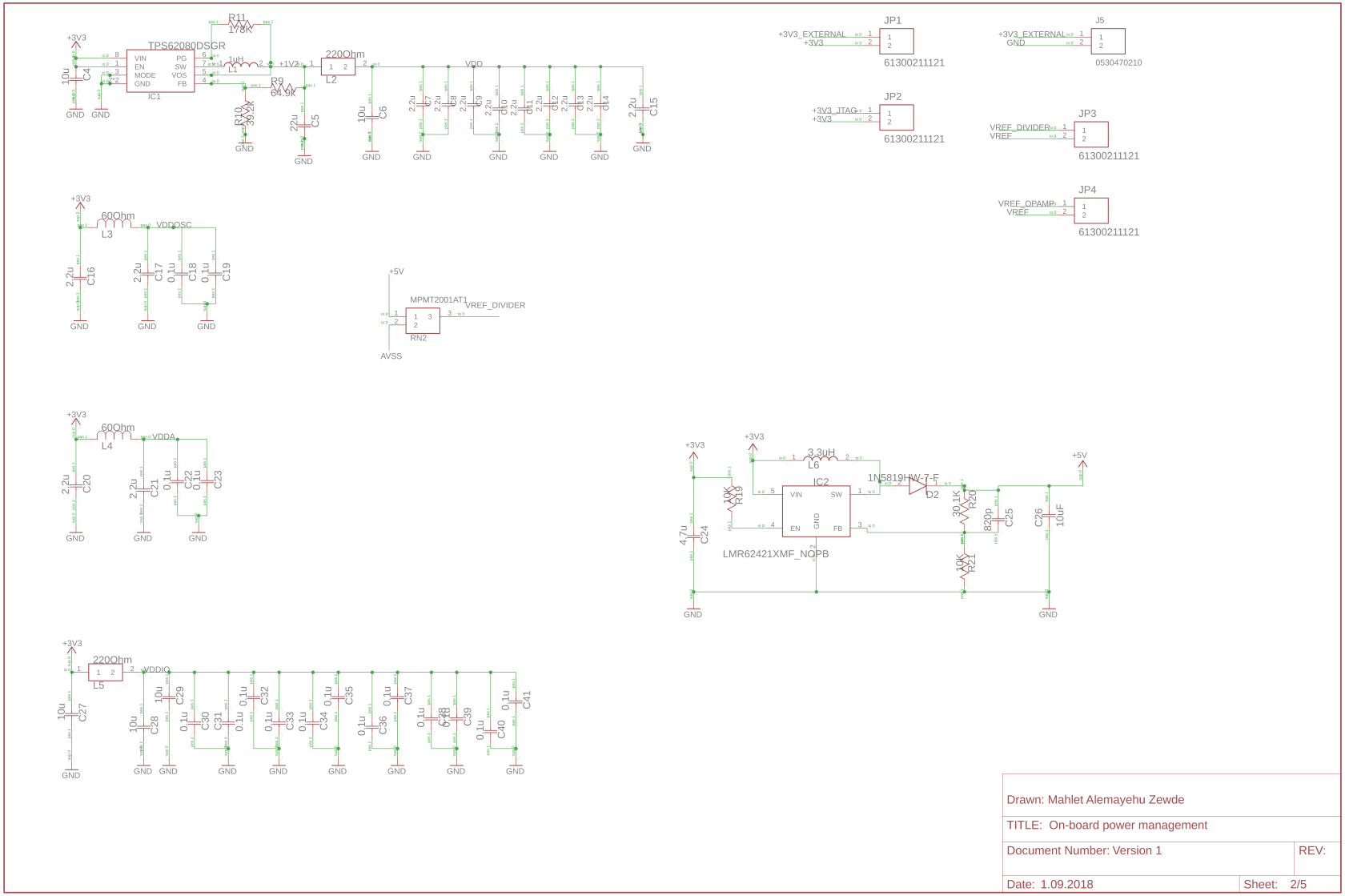

Figure A13: DAQ-C PCB On-board regulators Schematic

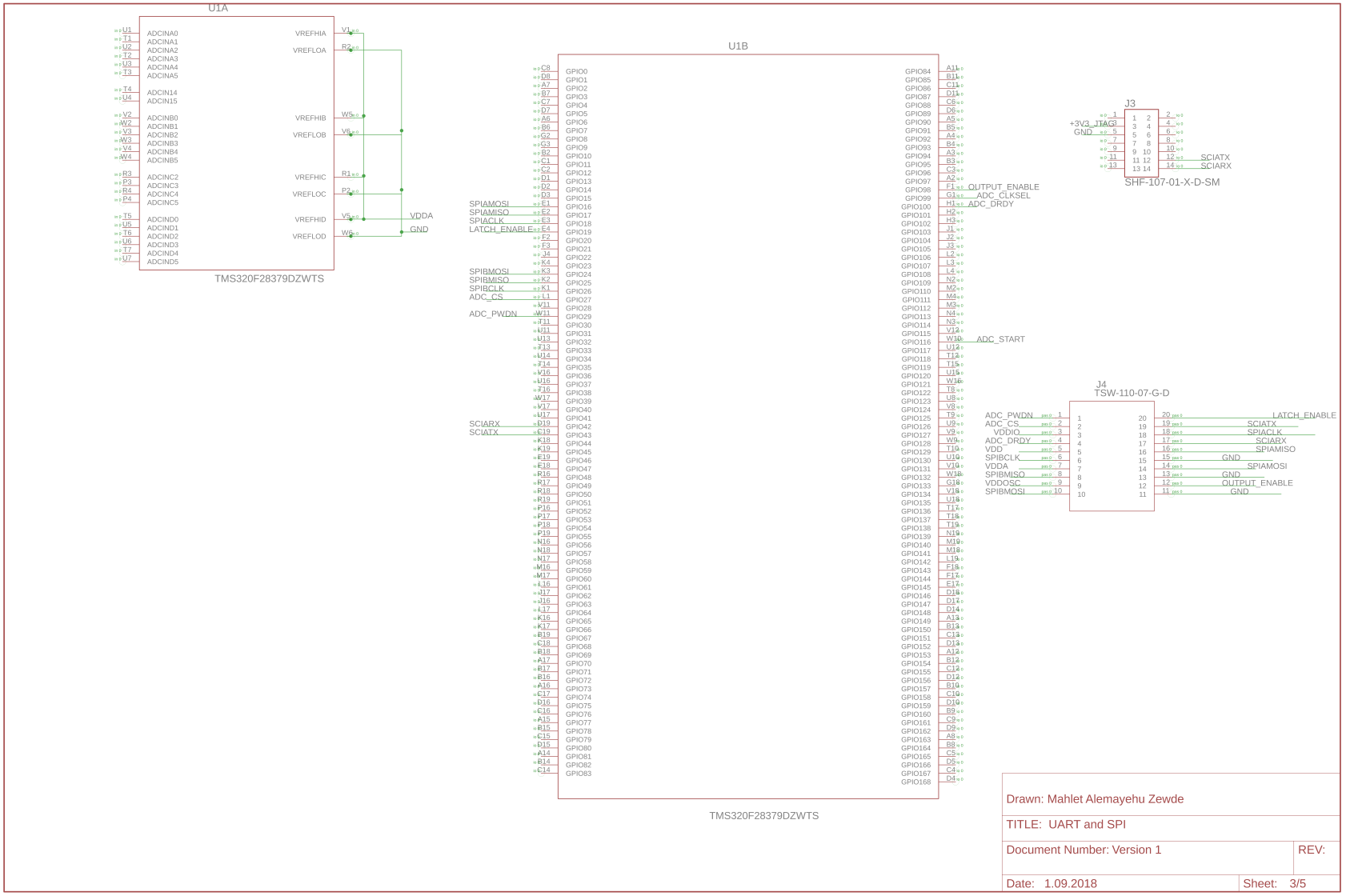

Figure A14: DAQ-C PCB UART and SPI Schematic

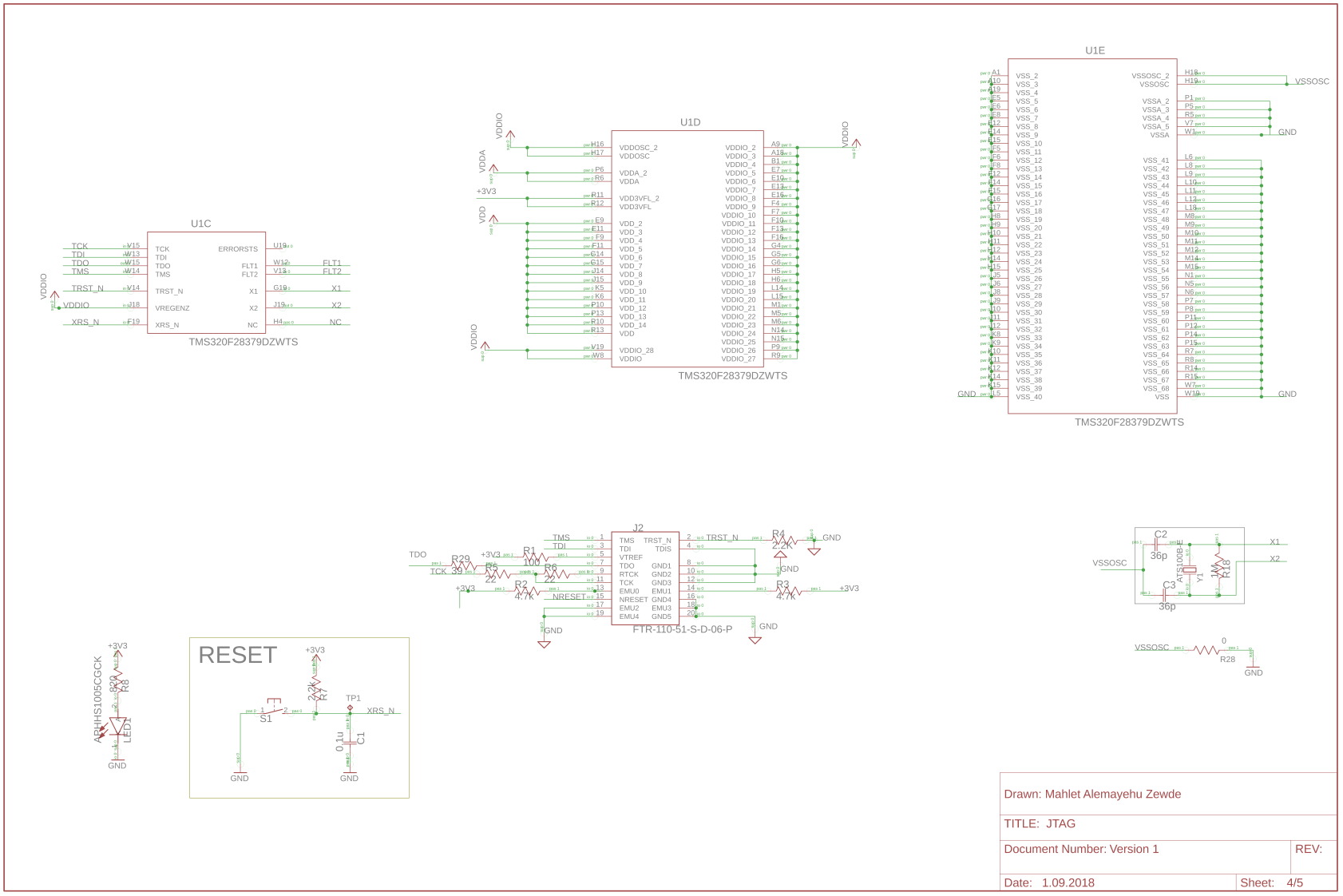

Figure A15: DAQ-C PCB JTAG connector and Oscilator clock Schematic

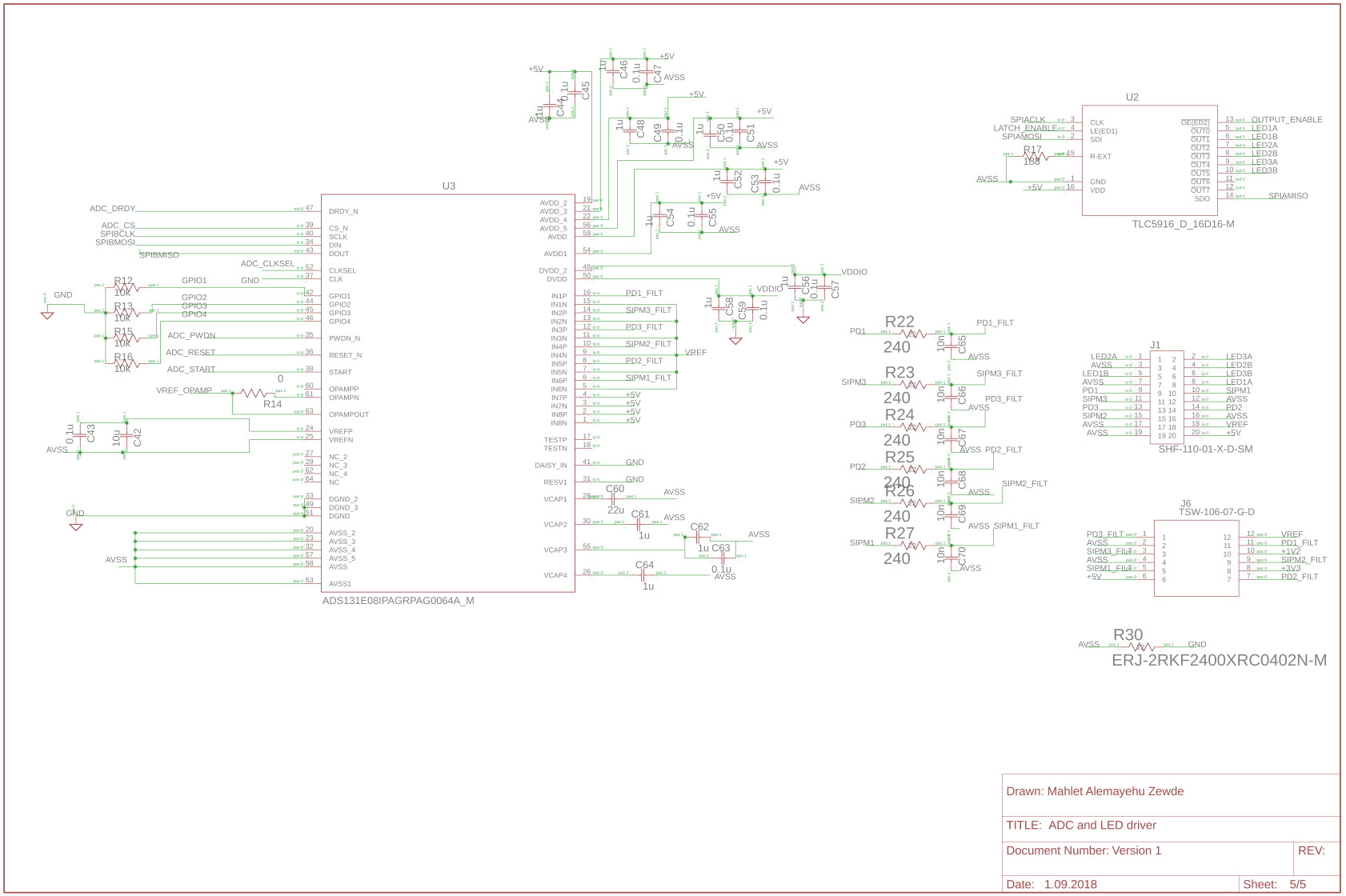

Figure A16: DAQ-C PCB ADC and LED Driver Schematic

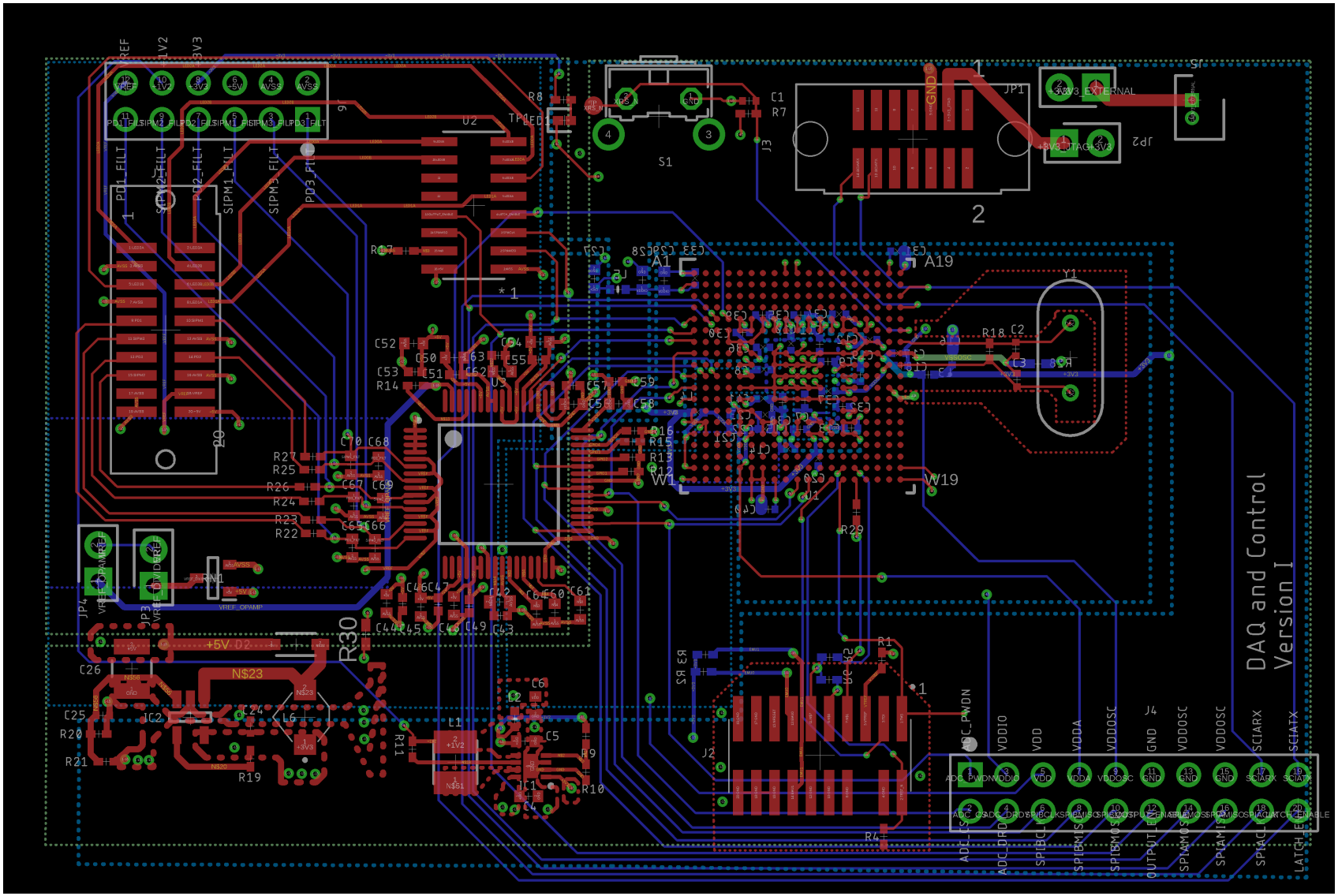

Figure A17: DAQ-C PCB Layout

Table A3: DAQ-C PCB Bill of Materials

Reference designators	Qty	Part number	Manufacturer	Description
S1	1	B3F-3152	Omron	Tactile Switch SPST-NO Side Actuated Through Hole, Right Angle
C1, C18, C19, C22, C23, C30, C31, C32, C33, C34, C35, C36, C37, C38, C39, C40, C41	17	GPC0402104-B	Generic part	0.1µF ±10% 16V Ceramic Capacitor X7R 0402 (1005 Metric)
R19, R21	2	ERJ-2RKF1002X	Panasonic	10 kOhms ±1% 0.1W, Chip Resistor 0402 (1005 Metric) AEC-Q200 Thick Film
Y1	1	ATS100B-E	CTS	10MHz ±30ppm Crystal 18pF 60 Ohms HC-49/US
C4, C6, C27, C28, C29	5	GRM188C80G106ME47D	Murata	10µF ±20% 4V Ceramic Capacitor X6S 0603 (1608 Metric)
C26	1	GPC1210106	Generic part	10µF ±10% 50V Ceramic Capacitor X5R 1210 (3225 Metric)
R11	1	ERJ-2RKF1783X	Panasonic	178 kOhms ±1% 0.1W, Chip Resistor 0402 (1005 Metric) AEC-Q200 Thick Film
R18	1	ERJ-2RKF1004X	Panasonic	1M Ohm ±1% 0.1W, Chip Resistor 0402 (1005 Metric) AEC-Q200 Thick Film
D2	1	1N5819HW-7-F	Diodes	Diode, Schottky, 40V, 1A, SMD
L1	1	LQH44PN1R0NP0L	Murata	1µH Shielded Wirewound Inductor 2.45A 36 mOhm Max Nonstandard
R7	1	ERJ-2RKF2201X	Panasonic	2.2k Ohm ±1% 0.1W, Chip Resistor 0402 (1005 Metric) AEC-Q200 Thick Film
C7, C8, C9, C10, C11, C12, C13, C14, C15, C16, C17, C20, C21	13	CL05A225MR5NNNC	Samsung	2.2µF ±20% 4V Ceramic Capacitor X5R 0402 (1005 Metric)
L5, L2	2	BKP1005EM221-T	Taiyo Yuden	FERRITE BEAD 220 OHM 0402 1LN

Table A4: DAQ-C PCB Bill of Materials (Continued)

Reference designators	Qty	Part number	Manufacturer	Description
C5	1	GRM188C80G226MEA0D	Murata	22µF ±20% 4V Ceramic Capacitor X6S 0603 (1608 Metric)
L6	1	CDRH3D16/HPNP-3R3NC	Sumida	3.3µH Shielded Inductor 1.8A 85 mOhm Max Nonstandard
R20	1	ERJ-2RKF3012X	Panasonic	30.1 kOhms ±1% 0.1W, Chip Resistor 0402 (1005 Metric) AEC-Q200 Thick Film
C2, C3	2	C0402C360J5GACTU	Kemet	Capacitor, Ceramic, 36pF 50V 5% NP0
R10	1	ERJ-2RKF3922X	Panasonic	39.2 kOhms ±1% 0.1W, Chip Resistor 0402 (1005 Metric) AEC-Q200 Thick Film
C24	1	GRM155R60J475ME47D	Murata	SMD Multilayer Ceramic Capacitor, 0402 [1005 Metric], 4.7 µF, 6.3 V, ± 20%, X5R
L3, L4	2	BLM15PD600SN1D	Murata	FERRITE BEAD 60 OHM 0402 1LN
R9	1	ERJ-2RKF6492X	Panasonic	64.9k Ohm ±1% 0.1W, Chip Resistor 0402 (1005 Metric) AEC-Q200 Thick Film
R8	1	ERJ-2RKF8200X	Panasonic	820 Ohms ±1% 0.1W, Chip Resistor 0402 (1005 Metric) AEC-Q200 Thick Film
C25	1	C0402C821K5RACTU	Kemet	820pF ±10% 50V Ceramic Capacitor X7R 0402 (1005 Metric)
LED1	1	APHHS1005CGCK	Kingbright	Green 570nm LED Indication - Discrete 2.1V 0402 (1005 Metric)
IC2	1	LMR62421XMF/NOPB	Texas Instruments	Boost, SEPIC Switching Regulator IC Adjustable 2.7V 1 Output 2.1A, SOT-753
U1	1	TMS320F28379DZWTT	Texas Instrument	C28x C2000™ Delfino™ Microcontroller 32-Bit Dual-Core 200MHz 1MB NFBGA

Table A5: DAQ-C PCB Bill of Materials (Continued)

Reference designators	Qty	Part number	Manufacturer	Description
IC1	1	TPS62080ADSGT	Texas Instrument	Buck Switching Regulator IC, Adjustable 0.5V 1 Output 1.2A 8-WFDFN Exposed Pad
U3	1	ADS131E08IPAGR	Texas Instruments	IC, Analog Front-End for Power Monioring Control And Protection
U2	1	TLC5916IDR	Texas Instruments	IC LED DRIVER LIN 120MA 16SOIC
J3	1	SHF-107-01-L-D-SM	Samtec	.050 X .050 SHROUDED TERMINAL ST
J1	1	SHF-110-01-L-D-SM	Samtec	Connector Header Surface Mount 20 position 0.050" (1.27mm)
J2	1	FTR-110-51-S-D-06-P-TR	Samtec	Connector,Single or double row design Up to 80 pins
C44, C46, C48, C50, C52, C54, C56, C58, C61, C62, C64	11	GRM188R61A105KA61D	Murata	1µF ±10% 10V Ceramic Capacitor X5R 0603 (1608 Metric)
R1	1	ERJ-2GEJ101X	Panasonic	Res Thick Film 0402 100 Ohm 5% 0.1W Molded SMD Punched T/R
R2, R3	2	ERJ-2GEJ472X	Panasonic	4.7 kOhms ±5% 0.1W, Chip Resistor 0402 (1005 Metric) AEC-Q200 Thick Film
R4	1	ERJ-2GEJ222X	Panasonic	2.2k Ohm ±5% 0.1W, Chip Resistor 0402 (1005 Metric) AEC-Q200 Thick Film
R5, R6	2	ERJ-2RKF22R0X	Panasonic	22 Ohms ±1% 0.1W, Chip Resistor 0402 (1005 Metric) AEC-Q200 Thick Film
R12, R13, R15, R16	4	ERJ-2RKF1002X	Panasonic	10 kOhms ±1% 0.1W, Chip Resistor 0402 (1005 Metric) AEC-Q200 Thick Film
R17	1	ERJ-2RKF1870X	Panasonic	187 Ohms ±1% 0.1W, Chip Resistor 0402 (1005 Metric) AEC-Q200 Thick Film

Table A6: DAQ-C PCB Bill of Materials (Continued)

Reference designators	Qty	Part number	Manufacturer	Description
C42	1	GPC0603106	Generic part	Multilayer Ceramic Capacitors, SMD/SMT 0603 X5R 10 uF +/- 10% 10 V T&R GP
C43, C45, C47, C49, C51, C53, C55, C57, C59, C63	10	GPC0402104-B	Generic part	0.1µF ±10% 16V Ceramic Capacitor X7R 0402 (1005 Metric)
C60	1	GRM188R61A226ME15D	Murata	22µF ±20% 10V Ceramic Capacitor X5R 0603 (1608 Metric)
RN1	1	MPMT2001AT1	Vishay	1 kOhm 100mW Per Element Voltage-Divider 2 Resistor Network, SOT-23-3
R14, R28, R30	3	ERJ-2GE0R00X	Panasonic	0 Ohms Jumper 0.1W, Chip Resistor 0402 (1005 Metric) AEC-Q200 Thick Film
JP1, JP2, JP3, JP4	4	61300211121	Wurth Electronics	2 Positions Header Connector 0.100" (2.54mm) Through Hole Gold
J5	1	53047-0210	Molex	2 Positions Header Connector 0.049" (1.25mm) Through Hole Tin
R22, R23, R24, R25, R26, R27	6	ERJ-2RKF2400X	Panasonic	Res Thick Film 0402 240 Ohm 1% 0.1W Molded SMD Punched T/R
C65, C66, C67, C68, C69, C70	6	CGJ3E2C0G1H103J080AA	Murata	10000pF ±5% 50V Ceramic Capacitor C0G, NP0 0603 (1608 Metric)
R29	1	ERJ-2RKF39R0X	Panasonic	39 Ohms ±1% 0.1W, Chip Resistor 0402 (1005 Metric) AEC-Q200 Thick Film
J6	1	TSW-106-07-G-D	Samtec	Connector Header Through Hole 12 position 0.100" (2.54mm)
J4	1	TSW-110-07-G-D	Samtec	Connector Header Through Hole 20 position 0.100" (2.54mm)

A.6 Graphical user Interface Design

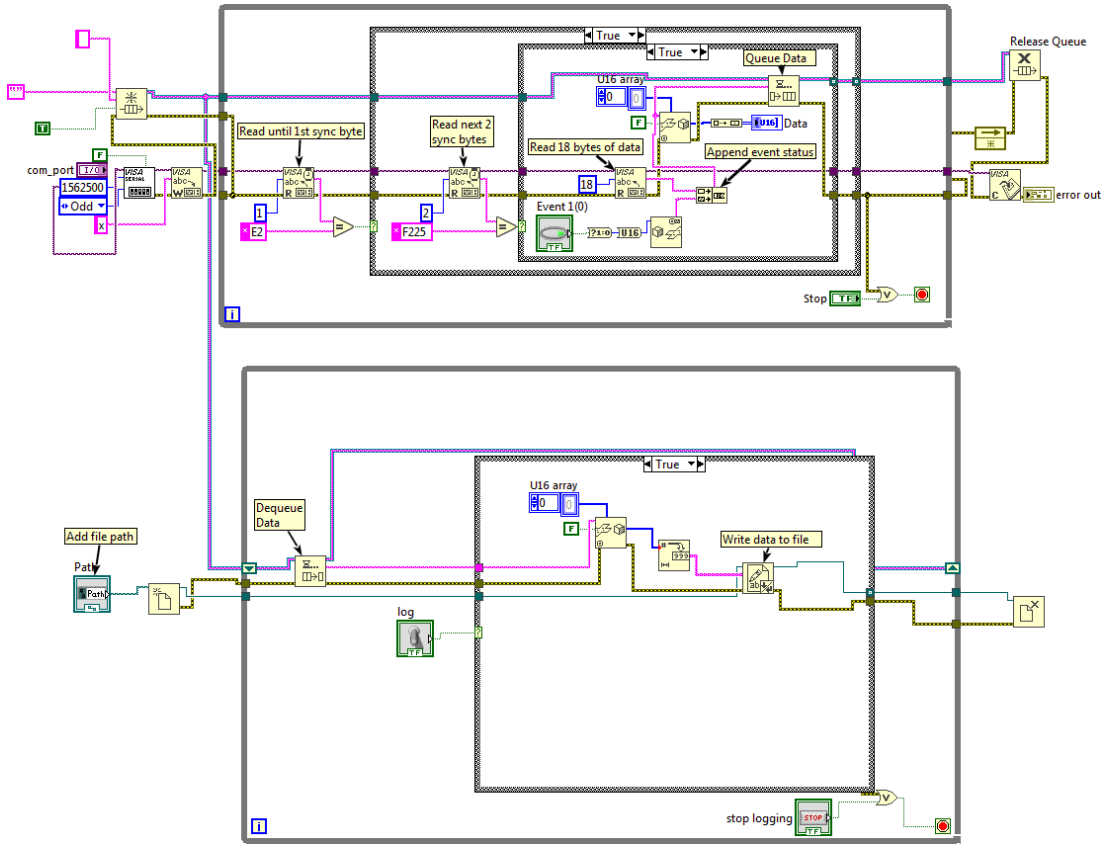

Figure A18: Graphical User Interface Block Diagram